Assessment and impact of aeroelastic effects in highly supersonic organic Rankine cycle turbines

Ricardo Oliveira

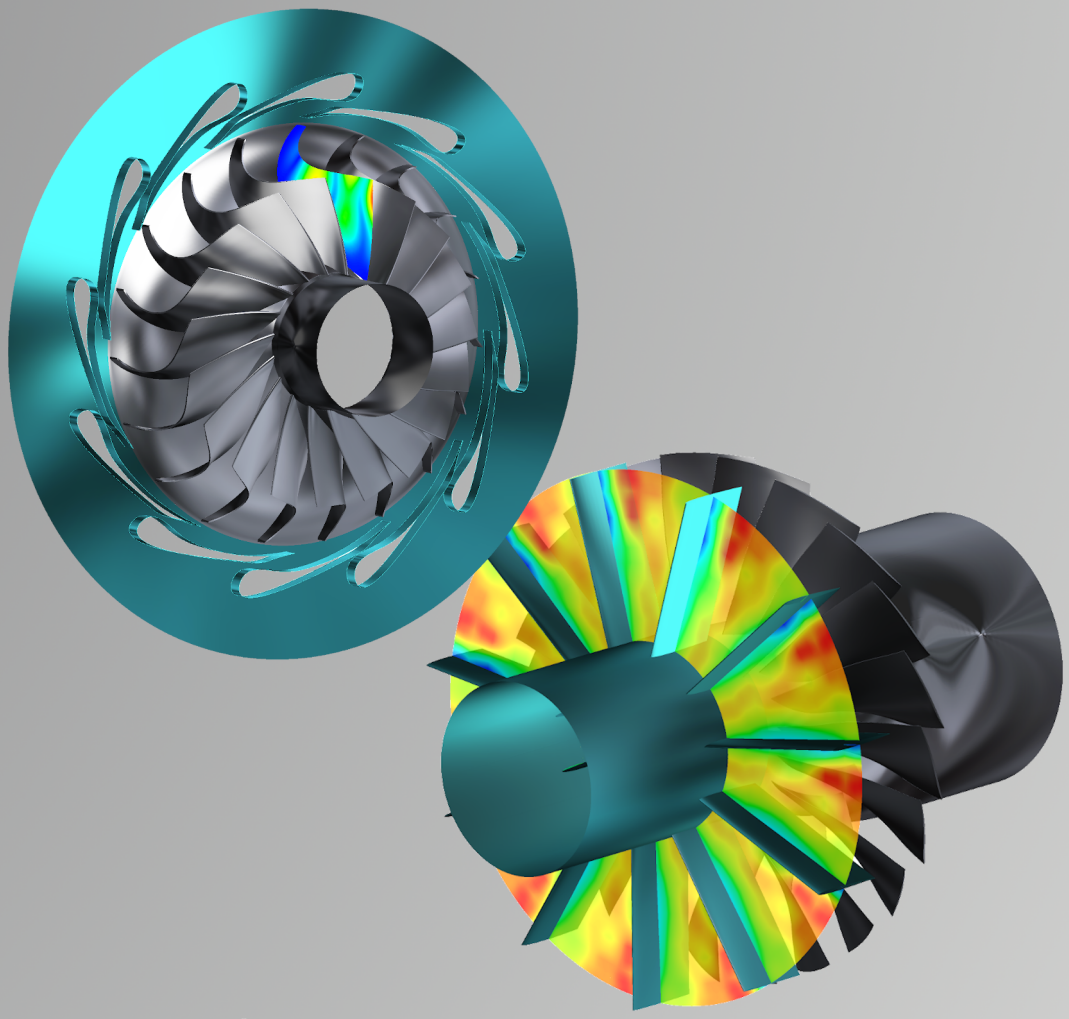

TU Delft

March 2020

Assessment and impact of aeroelastic effects in highly supersonic organic Rankine cycle turbines

by

Ricardo Oliveira

to obtain the degree of Master of Science
at the Delft University of Technology,
to be defended publicly on Monday March 2, 2020 at 2:00 PM.

Student number:	4736559	
Project duration:	February 2019 - March 2020	
Supervised by:	Dr. Ir. M. Pini,	TU Delft
	Ir. N. Anand,	TU Delft
Thesis committee:	Dr. Ir. M. Pini,	TU Delft, supervisor
	Ir. N. Anand,	TU Delft, supervisor
	Prof. Dr. Ir. P. Colonna,	TU Delft
	Dr. Ir. R.C Alderliesten,	TU Delft

TU Delft

Abstract

The current high demands for the energy and transportation industries make it imperative to design efficient and reliable turbomachinery. Aeroelastic phenomena such as forced response and flutter are one of the main concerns when designing these machines, and the incorrect prediction of these effects generates vibrations that can lead to structural failure due to high cycle fatigue. Furthermore, the search for unconventional energy sources is also of great relevance to meet these demands. Power generation using the Rankine cycle with organic fluids is one example of these technologies. The different thermodynamic properties, when comparing to water, of these fluids, make it possible to use low temperature energy sources, having many practical applications such as waste heat recovery and combined power cycles.

Organic fluids, due to their high molecular weight, are also characterized by a low speed of sound which results in a supersonic flow, leading to shock waves. This unsteadiness propagates onto rotating blade rows downstream and acts as a harmonic forcing. Investigating the impact of these effects on the structural integrity of small scale radial machines operating with organic fluids has not been done in the past and is the goal of this thesis.

The assembly of a forced response analysis chain is made and is based in three main points. First, finding and characterizing resonant conditions. Second, determining aerodynamic harmonic forcing and aerodynamic damping, and finally, place alternating and mean stresses against structural limits. This method was applied to two test cases, the NASA rotor 67 and the ORCHID turbine. The NASA rotor 67 is used as a benchmark case to assemble and validate the analysis chain due to the large amount of openly available experimental data. ORCHID is a small scale ORC turbine designed at TU Delft and is used to explore the influence of the aeroelastic effects on this category of machines.

For the ORCHID turbine, high unsteady pressures in the turbine rotor blades were observed by the simulations made. This is due to the shock waves in the upstream supersonic stator, from tip leakage and from potential interactions. In terms of flutter, a stable system was found for the resonant conditions studied. The regions of higher unsteadiness were confined to the upstream most part of the rotor blade being excited, which correspond to areas of small modal displacements. Furthermore, even with high rotational speeds, the small scale of the machine resulted in small centrifugal effects, and so in high allowable margins for alternating stresses. In sum, even with a high unsteady pressure content, the mismatch between these and the mode shapes, and the positive aerodamping values, result in a safe system in terms of high cycle fatigue for the resonant conditions studied.

The current work should be continued for the manufacture of the ORC turbine by investigating precise material properties, hub geometry and upstream inlet geometries that can lead to lower frequency resonant crossings. Furthermore, the investigation of the influence of the aeroelastic issues identified on the efficiency and the incorporation of the work developed on multi-disciplinary optimization procedures is also of great relevance and a main recommendation for further studies.

Contents

Nomenclature

Acronyms

AIC	Aerodynamic influence coefficient
CFD	Computational fluid dynamics
EO	Engine order
FEA	Finite element analysis
HCF	High cycle fatigue
IBPA	Interblade phase angle
IGV	Inlet guide vane
ITSM	Institute of Thermal Turbomachinery and Machinery Laboratory
LCF	Low cycle fatigue
LPT	Low pressure turbine
NACA	National Advisory Committee for Aeronautics
NASA	National Aeronautics and Space Administration
ND	Nodal diameter
NSV	Non-synchronous vibrations
ORC	Organic Rankine cycle
RANS	Reynolds-averaged Navier-Stokes
RC	Resonant crossing
R67	Rotor 67
SDOF	Single degree of freedom
TWM	Travelling wave mode
URANS	Unsteady Reynolds-averaged Navier-Stokes

Latin Symbols

A	Amplitude
d	Damping
$[D]$	Damping matrix for multiple degree of freedom
e	Exponential
E	Young modulus
F	Force

i	Imaginary number
k	Stiffness
$[K]$	Stiffness matrix for multiple degree of freedom
m	Mass
$[M]$	Mass matrix for multiple degree of freedom
M_w	Molecular weight
N	Number of *subscript*
p	Pressure
P	Power
q	Displacements for single degree of freedom
R	Gas constant
t	Time
T	Temperature
$\mathcal{T}$	Period
v	Velocity
W	Work
X	Displacements for multiple degree of freedom

Greek Symbols

γ	Generalized coordinate or Modal participation factor
$[\Gamma]$	Modal participation factor matrix
η	Efficiency
ν	Poisson coefficient
ξ	Aerodynamic damping ratio
ρ	Density
σ	Stress
ϕ	Mode shape
$[\Phi]$	Mode shape matrix
Ω	Rotational speed

Subscripts

aero	Aerodynamic
alt	Alternating
b	Blade numbering
backward	Backward
dist	Disturbance
end	Endurance

exc	Excitation
forward	Forward
gen	Generalized
k	Mode number k
max	Maximum
mean	Mean
mode	Mode
motion	Motion
n	Harmonic numbering
nat	Natural
RPM	Rotations per minute
static	Static
struct	Structural
tt	Total to total
ts	Total to static
ult	Ultimate
yield	Yield

Accents

$\check{()}$	Complex number
$\bar{()}$	Mean
$\hat{()}$	Module of a complex number
$\ddot{()}$	Second time derivative
$\dot{()}$	Time derivative
$()^T$	Transpose
$\tilde{()}$	Unsteady
$\vec{()}$	Vector

List of Figures

List of Tables

1 Introduction

1.1. Background

In recent years the world has seen a constant growth in population and has undergone groundbreaking technological developments in many different industries. Since the 1960s, the world population has more than doubled, going from 3 to 7.5 billion people, and the current increasing trend continues. A more populated and developed world results in evident demand increases for the energy and transportation sectors. These industries rely heavily on turbomachinery components, and so the constant need for efficiency improvements and the search for unconventional energy sources has become imperative in order to reduce costs and emissions.

Turbomachinery optimization procedures are usually based on aerodynamic improvements having only general structural constraints. As a consequence, designs usually result in thinner blades subject to high aerodynamic loadings [1]. This raises concerns regarding structural issues due to vibrations and stationary loadings, and so being able to analyse turbomachinery components in terms of high cycle fatigue becomes of major relevance to avoid failure occurrences. Furthermore, being able to incorporate static and dynamic structural analysis into effective multidisciplinary optimization procedures can result in substantial time and money savings during the design phase.

To correctly analyse the structural behaviour of a turbomachinery component it is necessary to account for the aerodynamic loadings applied. As known, in this class of machines, an inherent unsteadiness is present, coming from the interaction of stationary and rotating components. Thus, the vibration phenomena will be associated with an unsteady aerodynamic flow that can possibly lead to vibrations which will, in turn, generate further unsteady loadings. The described coupling, between fluid and structural behaviour, leads this analysis to fall into the field of aeroelasticity. Indeed, taking

into account the interaction between the aerodynamic flow and an elastic structure is essential to ensure the safe operation of not only turbomachines, but also of aircraft, race cars, and even buildings and bridges. In 1946, Collar [2] defined the well known triangle of forces for aeroelasticity, presented in Figure 1.1, that illustrates a system handling inertial, elastic and aerodynamic forces in a dynamic way. The field of static aeroelasticity concerns only elastic and aerodynamic forces and is also of much relevance in the manufacturing process of turbomachines and in the design of aircrafts.

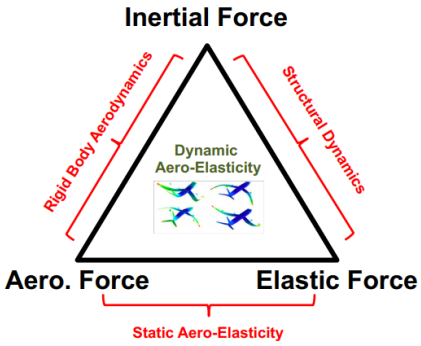

Figure 1.1: Illustration of the Collar's triangle of forces which represents the different contributions of inertial, aerodynamic and stiffness forces in the aeroelasticity domain.

The present work focus on the study of the dynamic aeroelastic effects, in small scale, highly supersonic organic Rankine cycle (ORC) turbines. These machines, that have a power output in the order of tens of kW, have been subject to various research and development activities at the Technical University of Delft (TUDelft), a challenging process due to the lack of available design methods for turbines operating with non-ideal fluids [3].

As previously mentioned, the recent world energy consumption rise, and the emissions associated with power generation, make it imperative to investigate alternative heat conversion technologies. The ORC technology is an example that can play a part in achieving objectives related to the reduction of emissions [4]. The advantage of using the Rankine cycle with organic fluids comes from the fact that the choice of the working fluid represents an important degree of freedom in the thermodynamic cycle and system design. Due to this, organic Rankine cycle systems exhibit relatively high efficiency for low-to-medium power capacity applications and temperature levels of the heat source up to 400°C [5]. Hence, the conversion of thermal energy at low and medium temperatures, into electrical and/or mechanical energy can be made, which allows the use of renewable heat sources (such as geothermal, biomass and solar) and of waste heat recovery from different sources (such as industrial processes, power plants, and exhaust gases of automotive engines) [4]. Specifically, the recovery of waste heat from long-haul truck engines and aboard aircraft is the application currently driving the development of the ORCHID turbine at TUDelft, which is used as a test case in this work [3].

1.2. Motivation

One important characteristic of organic fluids is their high molecular weight which will result in a low speed of sound. Because of this, supersonic flows occur even at low operating speeds, resulting in shock waves in the stator that will interact with the turbine rotor [6]. The unsteadiness created in the stator is, even if stationary, seen as a harmonic force on the rotating blades operating downstream. More particularly, slender blades in an ORC turbine will be subject to a high unsteady loading. This may lead to aeroelastic issues such as forced response that can possibly result in premature failure of blades. Hence, a forced response analysis of these machines is necessary.

A study regarding the forced response analysis of small scale, supersonic turbines operating with organic fluids has not been performed yet. Assessing the influence of organic fluids on the structural integrity of the ORCHID turbine motivates this MSc thesis work.

1.3. Research objectives and questions

This MSc thesis work will be based on the construction of a forced response methodology using one-way fluid-structure interaction simulations by using the commercial software package ANSYS and its application to two test cases. The first test case is the NASA rotor 67, a transonic axial fan developed in the 1980's and for which experimental and numerical data is available in open literature. In this way, this test case is used to validate and verify results obtained throughout the development of the forced response analysis. The second test case is the ORCHID turbine, which is a small scale, radial inflow turbine operating with an organic fluid. As mentioned, a study of aeroelastic effects in the type of machines described has never been made, and so this test case represents the main innovation of this thesis.

This work counted of the support of the Institute of Thermal Turbomachinery and Machinery Laboratory (ITSM) at the University of Stuttgart, where the candidate went for an exchange of 4 months. A study regarding different transient methods for the simulation of unsteady flows in turbomachinery was also performed during the exchange and is also briefly presented in this work.

Building knowledge at TU Delft regarding aeroelastic analysis in turbomachinery, that can possibly allow for future work in this field to be conducted, was an important goal of this thesis. More specifically, relating to the necessary analysis, the objectives of this work can be summarized in 3 main points:

- Conduct one-way fluid-structure interaction simulations that can allow for the forced response analysis of turbomachinery components subject to unsteady aerodynamic loadings, based in three main steps:
  - Identify resonant conditions: Determine engine order, rotational speed and structural vibration mode (Blade mode shape, vibration frequency and interblade phase angle);

  - Compute aerodynamic forcing and aerodynamic damping:
    - Aerodynamic forcing: Conduct transient stator-rotor CFD simulations to export unsteady blade surface pressures - Compute the generalized force;
    - Aerodynamic damping: Conduct transient vibrating mesh CFD simulations to export unsteady blade surface forces and mesh velocities - Compute aerodynamic damping ratio;
  - Compute static stresses, due to centrifugal loading, and alternating stresses at the identified resonant conditions, due to blade vibration. Assemble the Haigh diagram to compare the mentioned structural stresses against material limits regarding high cycle fatigue (HCF);

- Apply the described process to a benchmark test case - NASA rotor 67 - to validate and verify results obtained throughout. Perform a study regarding different transient methods for the simulation of unsteady flows in turbomachinery using this case - Compare values of the generalized force using different methods;
- Apply the described process the ORCHID turbine developed at TU Delft. Conclude regarding the influence of operating with organic fluids on the structural integrity of these machines by answering the research questions.

Building from the objectives presented, the research questions of this thesis are:

1. Which are the dominant aeroelastic issues in small-scale, highly supersonic machines operating with organic fluids?

   a) What can be concluded regarding the stability of the system in terms of aerodynamic damping?

   b) Which are the recognizable flow features that can lead to excitation?

   c) What is the magnitude and location of unsteady pressures coming from upstream disturbances and from blade vibration?

2. What can be concluded regarding the influence of the aeroelastic issues identified on the life of the machine being analysed?

   a) How do the identified flow features relate with the structural response?

   b) Do static and/or alternating stresses surpass structural limits defined?

   c) What is the estimate life of the machine and what are the limitations of this prediction?

   d) Which advices can be given to the turbine manufacturer to reduce vibrations and increase safety margins regarding high cycle fatigue?

1.4. Outline

The report presented will begin with a theoretical background, in Chapter 2, regarding aeroelastic phenomena in turbomachinery. Important concepts such as flutter and forced response will be introduced in a physical manner. With them, some aspects regarding aerodynamic excitations and structural vibrations will also be elaborated. In the end, a contextualization regarding analysis methods for forced response and their relation with the fluid-structure coupling will be made, which will be crucial when choosing the type of analysis to be made and to be aware of the assumptions that come with it.

The concepts mentioned will be elaborated in the Chapter 3. First, the necessary steps for the analysis are introduced and a theoretical background on vibration theory is provided. After this, the inherent assumptions of the methodology are presented. Finally, the methodology steps are further detailed with theoretical and physical explanations of the underlying methods used.

Following this, in Chapters 4 and 5, the results of the test cases are presented following four main points. First, the structural and fluid computational models used for simulations are presented. Following this, the identification of resonant conditions is made. The results regarding aerodynamic transient simulations are then given and, finally, the structural integrity of the machine is analysed and conclusions are taken.

In the end, Chapter 6 presents the conclusions of the thesis work and the answers to the elaborated research questions. Also in this chapter recommendations for future work are given.

2

Theoretical background

2.1. Aeroelastic phenomena in turbomachinery

The field of aeroelasticity as introduced by Collar in [2] concerns the phenomena that show an inherent coupling between structural dynamics and aerodynamics. The triangle of forces, introduced previously in Figure 1.1, illustrates the forces in play in this domain, consisting of the mutual interaction between inertial, elastic and aerodynamic forces. This concept helps to understand how the mentioned forces contribute to the different disciplines of the aeroelasticity field.

A relevant contribution of all the forces results in the field of dynamic aeroelasticity, which concerns phenomena such as flutter, limit-cycle oscillations, forced response and non-synchronous vibrations (NSV) [7]. Flutter is a phenomenon that is driven by the unsteady aerodynamic forces generated by blade vibrations, and so is considered to be a case of self-excited oscillations. On the other hand, forced response will be driven by flow defects that will act as periodic forces on a rotating blade row [1]. Moreover, the phenomenon of limit-cycle oscillations is seen as a particular case of flutter where non linearities constrain the amplification of vibrations until a steady, periodic state is achieved [8]. Finally, non-synchronous vibrations are induced by flow unsteadiness such as tip leakage [9] rather than by blade motion itself.

In static aeroelasticity only aerodynamic and elastic forces come into play. The relevance of this field in turbomachinery is related to the manufacturing process, where static aerodynamic loads can change the blade geometries significantly.

The consideration of only aerodynamic and inertial forces results in the topic of rigid-body aerodynamics which is the core consideration for the usual aerodynamic optimization procedures used in turbomachinery.

The exclusion of aerodynamic forces ends up in the structural dynamics topic which will also be of relevance in this work to understand how and when blades and bladed disk assemblies, also referred to as blisks, vibrate.

Referring to the Collar's triangle of forces, in Figure 1.1, the inertial, elastic and aerodynamic forces, together with a damping term, can be arranged in a mathematical form to assemble the aeroelastic system,

$$[M_{\text{struct}}]\ddot{\vec{X}} + [D_{\text{struct}}]\dot{\vec{X}} + [K_{\text{struct}}]\vec{X} = \vec{F}_{\text{aero}}(t), \tag{2.1}$$

where $[M_{\text{struct}}]$, $[D_{\text{struct}}]$, $[K_{\text{struct}}]$ represent the structural mass, damping and stiffness matrices and $\vec{X}$ the vector of structural displacements. $\vec{F}_{\text{aero}}(t)$ is related to the unsteady aerodynamic forces, which can be decomposed into the aerodynamic forces coming from flow defects, $\vec{F}_{\text{dist}}(t)$, and from the blade vibration motion, $\vec{F}_{\text{motion}}(t)$,

$$\vec{F}_{\text{aero}}(t) = \vec{F}_{\text{dist}}(t) + \vec{F}_{\text{motion}}(t). \tag{2.2}$$

By combining Equations 2.1 and 2.2, the final aeroelastic equation of motion that drives this topic can be defined:

$$[M_{\text{struct}}]\ddot{\vec{X}} + [D_{\text{struct}}]\dot{\vec{X}} + [K_{\text{struct}}]\vec{X} = \vec{F}_{\text{dist}}(t) + \vec{F}_{\text{motion}}(t). \tag{2.3}$$

In Equation 2.3, the $\vec{F}_{\text{dist}}(t)$ term is of great relevance when studying aeroelastic effects in turbomachinery, since, being related to flow defects, will be directly associated with the turbomachine configuration and will act as an excitation force. On the other hand, the $\vec{F}_{\text{motion}}(t)$ term, being related to the blade motion, can have influences on the left hand side of Equation 2.3 acting has aerodynamic mass, damping or stiffness terms and, as will be explained, can possibly give origin to a negative damping term characteristic of unstable systems. Understanding the physical origin of described force terms of Equation 2.3, what is their influence on the structural vibrations, and how they can be correctly simulated is a major step of this work.

2.1.1. Static aeroelasticity

The relevance of static aeroelasticity relates to the process of unrunning which is related to the fact that the centrifugal and gas loads will change the blade shape at the operating point. Unrunning consists in finding the correct blade shape to be manufactured (cold geometry) so that the optimum shape obtained from an aerodynamic optimization (hot geometry) is obtained at the operating point under the static loads mentioned. It is known that blades tend to untwist and show high bending displacements and that section profiles tend to uncamber under the centrifugal and gas loads [10].

2.1.2. Flutter

Flutter is an aeroelastic instability that can happen even with uniform flow, and so is related with how aerodynamic forces influence blade vibration when a perturbation is encountered. In Figure 2.1, a simplified overview of the flutter physical mechanism is given. A 2D airfoil emerged in a uniform incoming flow is initially at an equilibrium state. An outside perturbation such as, for example, vortex shedding, can initiate a vibratory motion that generates unsteady aerodynamic forces [1]. Depending on the inherent flow features and on the vibration motion, these forces can transfer energy onto the structure, leading to an increase in the amplitude of the initial vibrations (represented in red in Figure 2.1). This effect is quantified as a measure of damping of aerodynamic origin. In this case, a negative aerodynamic damping value is assessed, representing a flutter situation [1].

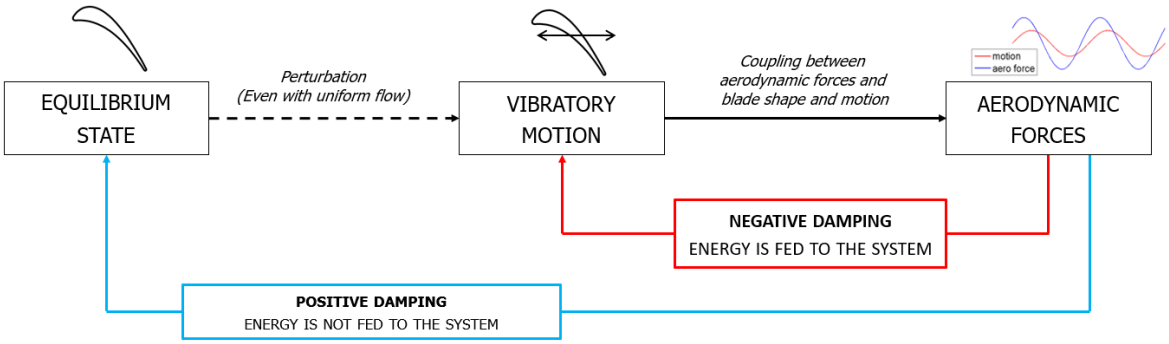

Figure 2.1: Illustration of the flutter physical mechanism as a stability problem due to unsteady aerodynamic forces induced by blade motion. Phasing between unsteady aerodynamic forces and blade motion results in an aerodynamic damping value that can be positive (in blue, leading back to equilibrium), or negative (in red, leading to the amplification of the vibratory motion).

On the other hand, a positive value of aerodynamic damping will lead the system back to an equilibrium state (represented in blue in Figure 2.1). In this case, energy is being transferred from the structure to the surrounding flow and the vibratory motion is damped until it stops. One of the main goals of designing against aeroelastic effects is ensuring that this situation is achieved [11].

The complexity of the prediction of flutter is easily seen by this simplified description considering a two dimensional single blade. When analysing a three dimensional cascade of blades it is straightforward to see that the complexity will rise, due to the aerodynamic coupling between blades and the complex three dimensional flow features. This concept will be elaborated in further sections but it is simple to understand that the vibratory motion of one blade will have aerodynamic repercussions in the flow on adjacent blades due to a passage effect. [11]

2.1.3. Forced response

In a simple way, forced response lays in the structure's response to a forced vibration. In the case of turbomachinery forced response analysis, complexity comes from the aerodynamic origins of excitation force and damping. The flow inside a turbine or compressor is never uniform since static and dynamic obstructions will generate wakes, potential pressure disturbances, flow distortions, shocks

and secondary flows. These unsteady effects may even be fixed in space, but are seen as periodic by the rotating passages. A match of frequency and shape between the unsteady forces rising from flow defects and the vibratory modes results in resonance, which represents the condition of highest vibration amplitudes [1].

The forced response analysis is then based on an aerodynamic analysis, where the transient effects described are simulated, and on a structural analysis, where the vibrating frequencies and shapes are computed, as illustrated in Figure 2.2. To find the conditions where the excitation and the natural frequencies match, the Campbell and interference diagrams are assembled and inspected. These will be described in detail in Chapter 3. As mentioned, resonant conditions are the ones that will result in the highest blade vibrations, and so these are the points at which the forced response analysis is conducted.

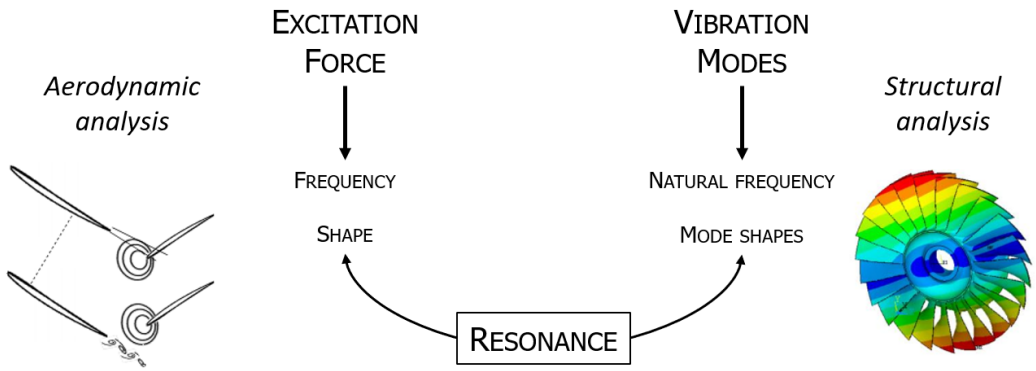

Figure 2.2: Illustration of resonant conditions by the match, in frequency and shape, of aerodynamic excitation forces and structural natural modes. In turbomachinery, the aerodynamic excitation will rise due to flow defects between adjacent blade rows. Vibration modes are characterized by structural properties and geometry of blades and bladed disk assemblies.

The possible excitation frequencies will be associated with engine orders, which will relate to the number of disturbances that can possibly be encountered when the machine is operating. Engine orders will then be integers that can be linked with, for example, the number of stationary components found upstream of a rotating passage and its multiples. This is an important concept in forced response analysis of turbomachinery which will be elaborated when introducing the Campbell diagram.

Vibration modes

In turbomachinery forced response analysis, the characterization of vibration modes of blades, disks, and bladed disk assemblies is necessary. For blades, the vibration modes are associated with bending (flap), torsion, and edgewise motion, and the amount of nodal lines encountered. For disks, the vibration modes are simply associated with the amount of nodal diameters that are found [12]. Blisk modes are a combination of blade and disk modes where the entire set of blades is vibrating with the same blade mode. At the same time, the motion of each blade is lagged between each other by an amount related to the amount of nodal diameters of the disk mode. The described modes are illustrated in Figure 2.3.

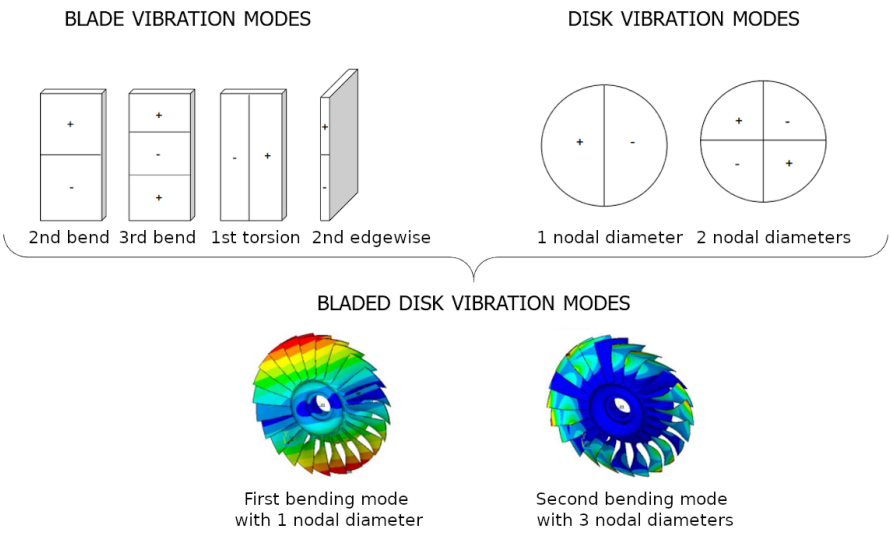

Figure 2.3: Illustration of relevant vibration modes: blade modes are characterized by bending, torsion, and edgewise motions and by the number of nodal lines; disk modes are characterized by the number of nodal diameters present; finally, bladed disk assemblies modes are a combination of blade and disk modes.

In specific, the bladed disk modes in Figure 2.3 are the combination of the 1^{st} bending blade mode and the 1 nodal diameter disk mode. Also the 2^{nd} bending mode with 3 nodal diameters is presented as an example.

Furthermore, for blisk modes, the travelling wave mode concept is introduced for cases where the nodal diameter rotates in the same or opposite direction as the rotational speed, corresponding, respectively, to a forward or backward travelling wave mode. The interblade phase angle, IBPA, will represent the phase lag between adjacent blades vibrating at a certain travelling wave mode,

$$\begin{cases} IBPA_{\text{forward}} = \frac{ND}{N_{\text{blades}}} 360 \\ IBPA_{\text{backward}} = \frac{360(N_{\text{blades}} - ND)}{N_{\text{blades}}} - 360, \end{cases} \tag{2.4}$$

where N_{blades} is the number of blades and ND the nodal diameter. The IBPA computed with Equation 2.4 will be positive for forward travelling wave modes and negative for backward travelling wave modes [1]. This quantity is of great relevance when computing the aerodynamic damping, as will be seen in Chapter 3, since it will have aerodynamic repercussions due to a passage effect [11]. Hence, the value of aerodynamic damping must be determined for the IBPA associated with the resonant conditions assessed. The whole stability curve, which relates the aerodynamic damping values for all the IBPA can also be determined to assess if a stable system is achieved for all modes.

2.2. Failure

The main failure mechanisms that occur due to vibrations in turbomachinery are overload, low cycle fatigue (LCF), and high cycle fatigue (HCF). Overload is referred to the cases where the load applied exceeds the ultimate tensile, compressive or shear strength of the material. For this to happen, the

deformation must be high enough that these limits are passed. This can possibly happen in cases of self-excited vibrations when the amplitude is not limited. Flutter is an example since, being an instability situation, the amplitude of vibrations can grow without being stopped, reaching a point where, by overload, the material will fracture [13].

Low cycle fatigue concerns the case where stresses above the yield strength of the material and under its ultimate strength are being applied. As a result, the deformations lead the material to a plastic behaviour region. A small amount of cycles will be sufficient for a failure occurrence. Thermal stresses due to the start and stop operation of a turbine or centrifugal effects dues to engine speed variations are examples of cases where low cycle fatigue can play an important role [13].

In terms of high cycle fatigue, failure can happen due to a high number of cycles happening at small elastic strains. The material will never undergo stresses above the yield strength, but the high number of cycles can still result in failure [13]. When assessing if a certain turbomachine will be prone to vibration problems it is seen that, in general, it will not be possible to avoid every resonance situation or to have a stable system for every vibration mode. In these cases it must be verified that the system will not exceed the high cycle fatigue limits. Haigh diagrams are usually used to assess these limits.

Some examples of failure occurrences can be found that truly represent the relevance of the topic in question. A first example lies in the blade failure of a 110 MW geothermal turbine in 2005, where 2 groups of blades in the last stage of the turbine were bent at around 140 degrees. An investigation led to find the origin of the failure, that was attributed to high cycle fatigue. It was concluded that resonance was not a cause for the vibrations that led to HCF. Instead, flutter was found to be the origin of the vibration motion, due to the operation of the turbines with a reduced mass flow, resulting in a negative incidence angle and inducing stall flutter. Furthermore, the vibratory motion led the blades to be free standing at some point, completely changing the structural damping characteristics and contributing to failure [14].

Resonance failures have also been reported. One example lays in an engine endurance testing program of a JAS-39 Gripen engine. An hour into the testing a low pressure turbine blade failure was seen. The cause of the problem was traced back to the blockage in three fuel nozzles. This blockage led to an incomplete combustion that resulted in resonance. Another example lays in the T55-L-11 engine where the shrouds of the blades of the second stage rotor turbine wore out through time due to excessive rubbing. Due to this, the blades became free-standing altering once more its damping characteristics and leading to vibratory resonance [1].

2.3. Methods for forced response analysis

An assessment of the current state of the art simulation methods used for aeroelastic predictions was carried out to gain knowledge regarding the available options. With this, an informed decision regarding which method was more adequate for the test cases studied could be made. The decision between the different numerical approach to take is connected to the physical assumptions of the fluid-

structure coupling [15].

The main division of the aeromechanical prediction methods can be made as decoupled and coupled methods. Decoupled methods, considered a one-way fluid-structure interaction method, attempt to solve the aeroelastic problem as a structural and an aerodynamics problem separately. Finite element analysis (FEA) and computational fluid dynamics (CFD) simulations are performed separately to determine modal shapes and frequencies, forcing functions and aerodynamic damping values (which will require modal information from the structural analysis) [10].

Coupled methods will solve the structural and fluid equations together and can still be split into partially-integrated and fully-integrated methods. In partially-integrated methods, which are considered two-way fluid-structure interaction methods, information regarding each simulation is exchanged at each timestep between structural and fluid environments. In this case, the force acting on a certain structure is determined by the CFD simulation and serves as boundary condition for the FEA simulation. This results in a certain displacement of the structure that changes the CFD mesh for the next timestep. Displacements and forces are sent back and forth at each time step between two different simulations. In the case of fully-integrated methods, the aeroelastic problem is defined in a single environment that involves both the structure and the fluid. The partially-integrated approach and the fully-integrated approach will converge to the same solution if the time step is reduced to close to zero [10]. An illustration of the methods described above is given in Figure 2.4.

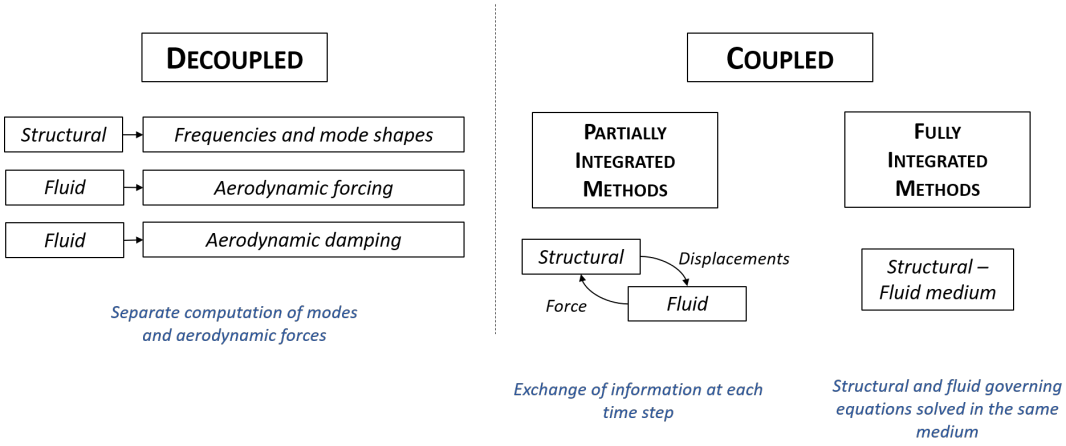

Figure 2.4: Illustration of coupled and decoupled methods for aeroelastic simulations. Decoupled methods are characterized by separate computations of structural vibration modes and fluid unsteady forces - the influence of the aerodynamic flow on structural modes is disregarded. In coupled methods, partially and fully integrated, information between different mediums is exchanged - the influence of the aerodynamic flow on structural modes is captured.

The main advantage of using decoupled methods is that there is the possibility of analysing separately the different vibration modes and frequencies, finding then resonant crossings associated with certain specific conditions. In coupled methods, the modal information is not separated, and so the influence of the unsteady aerodynamic forces on the vibration modes themselves is captured.

A decision regarding which method to use for the forced response analysis is made by assessing the type of fluid-structure coupling. The unsteady aerodynamic forces generated by the blade motion,

$\vec{F}_{\text{motion}}(t)$ from Equation 2.3, can have an impact on the structural behaviour, possibly generating aerodynamic mass, $[M_{\text{aero}}]$, damping, $[D_{\text{aero}}]$, and stiffness, $[K_{\text{aero}}]$, terms, that will be included on the left hand side of Equation 2.3. How the mentioned forces influence the structural behaviour (by influencing mass, damping and stiffness terms) is the criteria used to define the fluid-structure coupling. In [15] this topic is divided into weak, intermediate and multyphysics.

Weak coupling regards the case where only a constant aerodynamic damping term is of relevance. The damping forces from an aerodynamic origin are then linear in relation to the blade motion. The aerodynamic damping term originated from $\vec{F}_{\text{motion}}(t)$ is included on the left hand side of Equation 2.3,

$$[M_{\text{struct}}]\ddot{\vec{X}} + [D_{\text{struct}} + D_{\text{aero}}]\dot{\vec{X}} + [K_{\text{struct}}]\vec{X} = \vec{F}_{\text{dist}}(t). \tag{2.5}$$

Since mass and stiffness matrices are not affected, mode shapes and frequencies are not influenced by the aerodynamic behaviour, and so separate structural and aerodynamic simulations can be performed (decoupled methods are adequate). Furthermore, since the aerodynamic damping term is constant, it can be determined with only one transient fluid simulation.

Intermediate coupling is related to an aerodynamic damping term that is dependent on the blade motion,

$$[M_{\text{struct}}]\ddot{\vec{X}} + [D_{\text{struct}} + D_{\text{aero}}(X)]\dot{\vec{X}} + [K_{\text{struct}}]\vec{X} = \vec{F}_{\text{dist}}(t). \tag{2.6}$$

Decoupled methods can still be used, but determining the aerodynamic damping term becomes more challenging, as an iterative process must be conducted to obtain its correct value.

Finally, multyphysics coupling relates to the situation where the unsteady aerodynamic forces will influence both mass and stiffness components,

$$[M_{\text{struct}} + M_{\text{aero}}]\ddot{\vec{X}} + [D_{\text{struct}} + D_{\text{aero}}(X)]\dot{\vec{X}} + [K_{\text{struct}} + K_{\text{aero}}]\vec{X} = \vec{F}_{\text{dist}}(t), \tag{2.7}$$

which will influence the structural behaviour itself, modifying mode shapes and frequencies. In this case, a coupled analysis is required.

As it will be justified in following sections, a weak coupling, which allows for decoupled simulations to be performed will be assumed.

Relevant aeroelastic phenomena for this study are forced response and flutter which are considered dynamic aeroelastic effects, and so transient fluid simulations are necessary to determine aerodynamic forcing and damping. The forced response analysis is based in solving Equation 2.5, since a weak fluid-structure coupling is assumed. Furthermore, resonant conditions will be the ones of most concern since a frequency match between excitation and natural frequencies leads to the escalation of vibration amplitudes, and so of alternating stresses. Failure due to high cycle fatigue will be of concern due to the elastic strains and high number of cycles of the vibrations studied.

3

Forced response analysis method

3.1. Introduction

A theoretical and practical explanation of all the steps necessary in the forced response methodology is given here for the test cases considered in this study.

The goal of this analysis is to provide an estimation of the lifetime of the turbomachine. To achieve this, it is necessary to determine the static and alternating stresses at resonance conditions and to place them against structural limits regarding high cycle fatigue. The static stresses computed will come from the centrifugal loading due to the rotational speed. On the other hand, alternating stresses will rise due to the vibration of the blade, and so are dependent on the aerodynamic excitation force and on the aerodynamic damping values at resonant conditions

Taking this into account, the 3 main blocks of this methodology can be defined and are presented in Figure 3.1. These blocks are summarized in a simplified way and its substeps will be further detailed in this section.

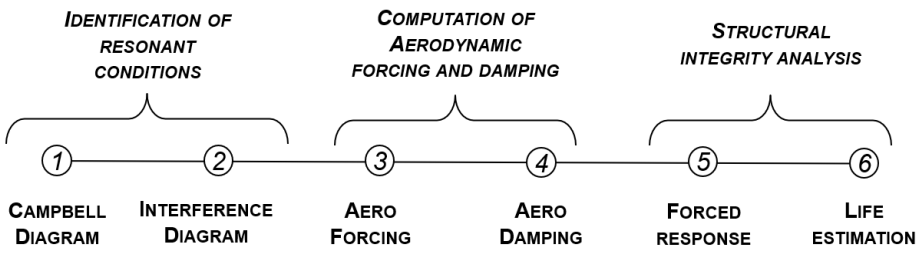

Figure 3.1: Forced response analysis chain based in: Resonance (Campbell and interference) diagrams to identify resonant crossings; Transient CFD simulations to determine forcing and damping and; Forced response analysis to assess structural integrity by means of the Haigh diagram.

The first step, the identification of resonant conditions, is made initially by using the Campbell diagram, which relates the possible excitation frequencies occurring at different operating speeds with the blade natural modes. The interference diagram is assembled at a specific rotational speed, and relates the possible excitation frequencies with the bladed disk natural modes. Resonant conditions will be characterized by a certain rotational speed, engine order, mode shape and frequency and interblade phase angle.

Once defined the resonant conditions, the aerodynamic forcing and damping values can be obtained through CFD transient analysis with different setups. These two components will be the determinant factors that can possible amplify or dampen the amplitudes and stresses. For the aerodynamic forcing, the unsteadiness will come from the disturbances caused by an upstream blade row whereas for the aerodynamic damping, these will be coming solely from the blade vibration with the mode shape and frequency of interest.

After this, static and alternating stresses are computed and verified against structural limits regarding high cycle fatigue (HCF). A constant life diagram, which represents the structural limits regarding fatigue [16], will be used to assess the structural integrity of the machine and to provide a life estimation.

These steps will be detailed in the following sections but before this, an important theoretical introduction to general vibration theory is made, that allows to gain understanding on the aerodynamic damping and forcing concepts and their importance on the vibration amplitudes and stresses. In the end, the assumptions associated with the forced response analysis chain are presented and justified.

3.1.1. Vibration theory

A forced response analysis consists of solving the equation of motion of a structure subject to an external excitation force, in order to find vibration amplitudes. In this section, the theory behind solving the equation of motion for a single degree of freedom (SDOF) oscillator is presented, being this a very relevant example that can explain most of the phenomena encountered in more complex systems with more degrees of freedom. Furthermore, it will be explained in the following section how, introducing generalized coordinates, a system with a higher number of degrees of freedom can be reduced to this simple example [17].

The single degree of freedom oscillator, shown in Figure 3.2, is ruled by the equation of motion, Equation 3.1:

$$m\ddot{q}(t) + d\dot{q}(t) + kq(t) = F_{\text{exc}}(t), \tag{3.1}$$

where m, d and k represent, respectively, the mass, damping and stiffness of the SDOF oscillator, $F_{\text{exc}}(t)$ the excitation force acting on it, and $q(t)$ the displacement regarding the axis of the degree of freedom.

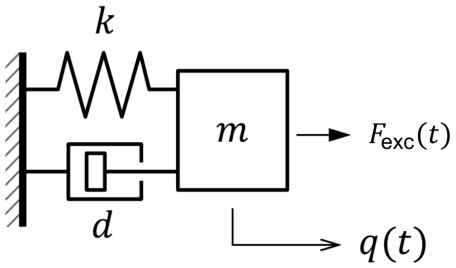

Figure 3.2: Single degree of freedom oscillator of mass m, stiffness k and damping d, subject to an external excitation force $F_{exc}(t)$.

Free oscillations

The case of free oscillations, where the excitation force is zero, $F_{exc}(t) = 0$, will be considered first. This example will help to gain understanding regarding aerodynamic damping and flutter.

In the case of free oscillations, the standard form of the equation of motion is written as,

$$\ddot{q} + 2\xi\omega_{nat}\dot{q} + \omega_{nat}^2 q = 0, \tag{3.2}$$

where ω_{nat} is defined as the natural frequency and ξ as the damping ratio and are defined as:

$$\omega_{nat} = \sqrt{\frac{k}{m}}, \tag{3.3}$$

$$\xi = \frac{d}{2\sqrt{km}}. \tag{3.4}$$

Considering a solution with an exponential form of : $q(t) = Ae^{\lambda t}$, and replacing in Equation 3.2, an algebraic equation is to be solved to determine the λ values that will ultimately determine the form of the solution itself,

$$(\lambda^2 + 2\xi\omega_{nat}\lambda + \omega_{nat}^2)Ae^{\lambda t} = 0. \tag{3.5}$$

Solving Equation 3.5 for λ while considering $q(t) = Ae^{\lambda} \neq 0$, so as to only find the non trivial solutions, the λ values will yield to:

$$\lambda_{1,2} = -\xi\omega_{nat} \pm i\omega_{nat}\sqrt{1-\xi^2}. \tag{3.6}$$

As we can see in Equation 3.6, depending on the value of the damping ratio, the value of λ can be: a purely real number, where the solution will be determined by an exponential; a purely imaginary number, where the solution will be a sinusoidal wave; or a complex number (with a real and an imaginary part), where the solution will be a combination of an exponential and a sinusoidal wave. The real part of the λ value will determine if we are in the presence of a stable system, where the vibration amplitude will decay, or in the presence of an unstable system, where the vibration amplitudes will be amplified.

In Figure 3.3, the locus of λ values is plotted in the Argand plane with varying values of damping ratio.

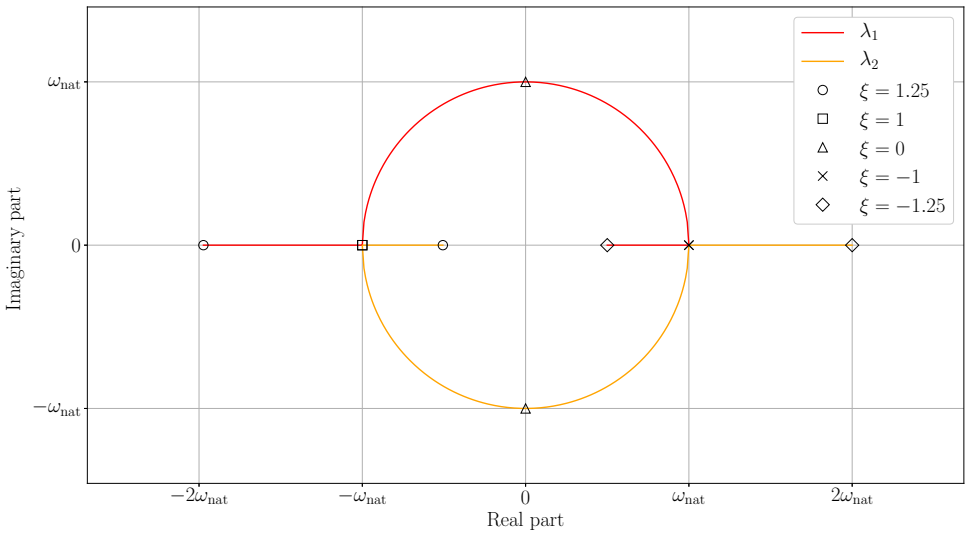

Figure 3.3: Argand plane locus of λ determined using Equation 3.6 to describe the dependence of free oscillation solutions with the damping ratio. Illustration of stable and unstable cases in relation to, respectively, negative or positive real part of λ.

Relating simultaneously to Figure 3.3 and 3.4, a value of ξ greater then one places the λ values in the real negative axis, representing a stable, over damped system characterized by a simple exponential decay. Moving towards values of damping close to zero, if $\xi \in]0, 1[$, the solution will still be damped, but with an imaginary component that introduces an oscillation component to the solution. The case of $\xi = 0$, represents a purely sinusoidal solution since a purely imaginary value of λ is encountered. Moving towards negative values of damping, an unstable system is found, first with an oscillatory component as $\xi \in]-1, 0[$ and after this, for values of $\xi \leq -1$, with only a growing exponential component.

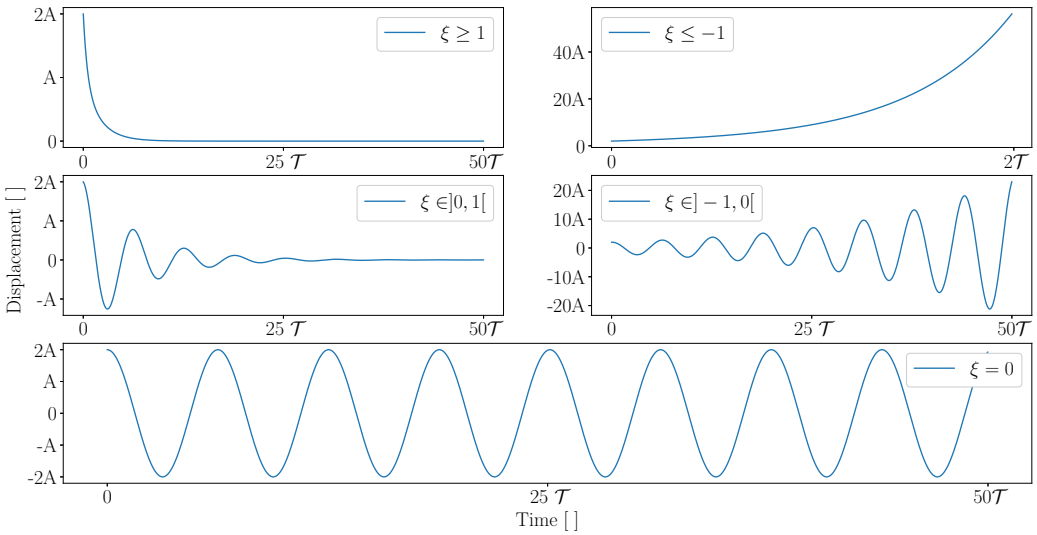

Figure 3.4: Solutions for the single degree of freedom free oscillations in the time domain. Illustration of stable and unstable cases, with and without oscillatory behaviour, in relation to damping ratio.

At this stage, some interesting considerations can be made, related to the single degree of freedom solutions. Namely, the important influence of the damping ratio on the solution, since negative values result in unstable systems, which result in the amplification of vibration amplitudes and alternating stresses, possibly leading to structural failure. Furthermore, the damping ratio due to a mechanical origin will be dependant on the physical dissipation, and so will always have a positive value. Usually, light mechanical damping values are encountered in turbomachinery applications (if no feature is added to the blade to increase damping) and is sometimes neglected from a forced response analysis [18]. Still, negative values of overall damping can originate if the aerodynamic damping is negative in such an amount that it overcomes the mechanical damping. In this situation, the flow is providing energy to the structure in such a way that the mechanical dissipation is not enough to counteract it, leading to flutter [1].

When the damping ratio is negative it is important to mention that in a real situation non-linearities will become relevant. These will cause a saturation in the vibration amplitudes and, if the steady state behaviour achieved is periodic, the case of limit cycle oscillations is achieved. This phenomena is related to the fact that damping will be dependant on the vibration amplitude and, at some vibration amplitude, will reach zero and maintain a periodic behaviour.

Harmonic forcing

The next case to be analysed is the one regarding the response to a harmonic forcing. Periodic excitations are typical in turbomachinery and can be decomposed into a sum of harmonic excitations, thus emphasizing the relevance of the case described. The equation of motion is once again Equation 3.1 with the external force as a harmonic force such as:

$$F_{\text{exc}}(t) = Re\{\hat{F}_{\text{exc}} e^{i\omega_{\text{exc}} t}\}, \tag{3.7}$$

where $\hat{F}_{\text{exc}}$ is the module of the excitation force, ω_{exc} the excitation frequency and i the imaginary number. The solution will be the superposition of the homogeneous solution, which is the case of free oscillations, and a particular solution associated with the excitation force. The analysis is limited to the case of positive subcritical damping since, in this case, the homogeneous solution will approach zero as we progress in time, being the particular solution the only relevant one.

This solution will be also a harmonic response at the same frequency as the excitation,

$$q(t) = Re\{\hat{q} e^{i\omega_{\text{exc}} t}\}, \tag{3.8}$$

where $\hat{q}$ is the module of the response. Replacing Equations 3.7 and 3.8 in Equation 3.1, we obtain:

$$\frac{\hat{q}}{\hat{F}_{\text{exc}}} = \frac{1}{-\omega_{\text{exc}}^2 m + i\omega_{\text{exc}} d + k}. \tag{3.9}$$

Solving Equation 3.9 for a range of different excitation frequencies and values of damping, the plot presented in Figure 3.5 is obtained.

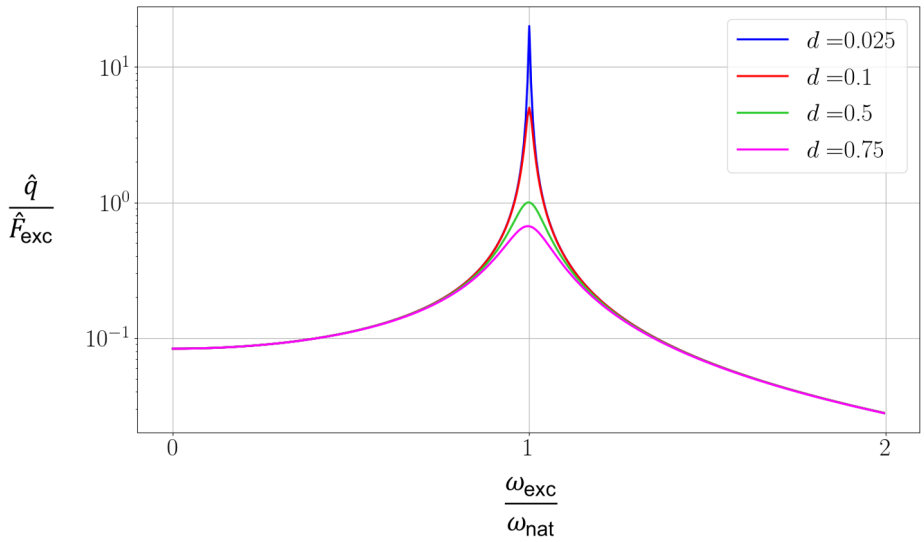

Figure 3.5: Single degree of freedom forced response to a harmonic excitation, computed from Equation 3.9, for a range of excitation frequencies and for varying damping values. Resonant conditions are identified by a response amplification for $\omega_{\text{exc}} = \omega_{\text{nat}}$. Higher vibrations amplitudes are identified for smaller damping values.

In Figure 3.5 it is clearly seen the increase of vibration amplitudes for frequencies close to the natural frequency and the reduction of these amplitudes for higher values of damping. The peak of vibration amplitudes at resonance conditions represents the values at which the higher alternating stresses are observed, and its value will be dependent on the excitation force and damping. This analysis serves also to illustrate how the response is amplified at resonant conditions.

3.1.2. Methodology overview

In conclusion, Figure 3.6 summarizes the forced response analysis chain. Each of the blocks will be explained in the following sections by focusing on the physical mechanisms being captured and on the simulation or computation needs. In a short way, the diagrams assembled in steps 1 and 2 will be based in structural simulations using finite element analysis, capturing natural modes of blades and bladed disk assemblies for different rotational speeds and thus characterizing resonant conditions. Step 3 concerns the transient CFD analysis necessary to compute the aerodynamic forcing. Different blade rows are included in the simulations in order to capture their unsteady interactions. In step 4, the aerodynamic damping is determined, also by means of transient CFD analysis, but where only the rotor blades are simulated with a prescribed vibratory motion. Finally, in step 5, the modal superposition method will be used to obtain the correct alternating stresses. This will allow to for the assemble of the Haigh diagram, in step 6, which is used to take conclusions regarding the structural integrity of the machine.

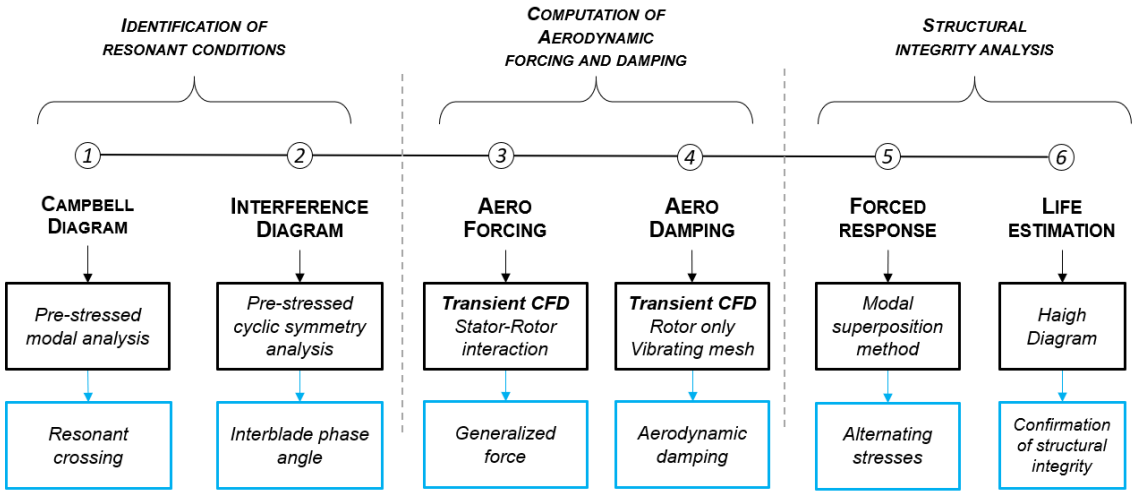

Figure 3.6: Forced response analysis chain. Description of simulation details and outputs for each substep. Identification of resonant conditions is based in structural simulations to assemble resonance diagrams. Aerodynamic forcing and damping require transient CFD simulations with different setups. The structural integrity analysis is based in implementing the modal superposition method and constructing the Haigh diagram using Python scripts developed.

3.1.3. Assumptions

The assumptions associated with the forced response methodology described in this chapter are:

1. The unsteadiness coming from the blade vibration and from the upstream disturbances can be decoupled. This will allow for the separated calculation of the aerodynamic forcing and damping terms. Some studies, such as [19] and [20], present a correlation between the upstream disturbances and the flutter behaviour. Nevertheless, the complexity of simulating this effect would rise, namely due to the phase between the blade vibration frequency and the stator passing frequency, and, not being a main interest of the thesis in question, this effect is not captured;

2. The CFD simulations to capture transient pressures were always performed at the design speed to avoid the process of assembling a performance map. The flow features are assumed to be sufficiently similar and of similar magnitudes in the operating range defined.

3. The fluid-structure interaction is of a linear nature, and so a weak fluid-structure coupling is verified. From this assumption, the influence of the unsteady aerodynamic forces due to blade vibration will only have an impact on the damping term of the equation of motion. One-way fluid-structure interaction simulations can be made since the unsteady aerodynamic forces will not influence the mass and stiffness matrices, and so the vibration modes remain unchanged. As described in [21], this assumption is valid for cases of small vibration amplitudes and high blade to air mass ratios. This is the case for turbomachinery components subject to forced excitations, and so this assumption can correctly be applied to the test cases studied in this work. Furthermore, the determination of the aerodynamic damping is possible to obtain with only one CFD simulation;

4. Small vibration amplitudes are assumed for the implementation of the aerodynamic influence coefficient [22].

5. Mechanical damping is neglected. This assumption comes from the fact that mechanical damping is usually very small in turbomachinery applications and always has positive values [18]. In this way, not taking this quantity into account simplifies the analysis and provides conservative results.

6. The structural response is dominated by the influence of only one mode near the resonant conditions of interest, which allows for only one mode to be considered during the determination of alternating stresses;

7. The bladed disks under analysis are perfectly tuned. As a consequence, all the blades in the assembly are assumed to have the exact same geometry. In a real case the manufacturing tolerances and the operational wear can cause random deviations in blade geometry [23] but, not being the main interest of this work, and to avoid the complexity of capturing this effect, the described assumption is made;

8. Differences between hot and cold geometries were not taken into account, and so hot geometries were used. With this it was possible to avoid the process of conducting further structural and aerodynamic analysis necessary to find the cold geometry to be manufactured. The unrunning process, which addresses this topic, is described in Section 2.1.1.

3.2. Campbell Diagram

As briefly mentioned previously, the Campbell diagram provides a match between the possible excitation frequencies and the natural frequencies associated with the blade. A brief explanation regarding the excitation frequencies, which are associated with engine orders, is here given.

Imagining a rotor operating downstream of a stationary blade row consisting of 3 stators, each producing a pressure drop in the wake, a certain point of this rotor will feel a pressure disturbance as depicted in the first graph in Figure 3.7. Linearly increasing the rotational speed, as an example, to its double, will result in these 3 disturbances to be felt in half the previous time, and so doubling the frequency of this pressure disturbance.

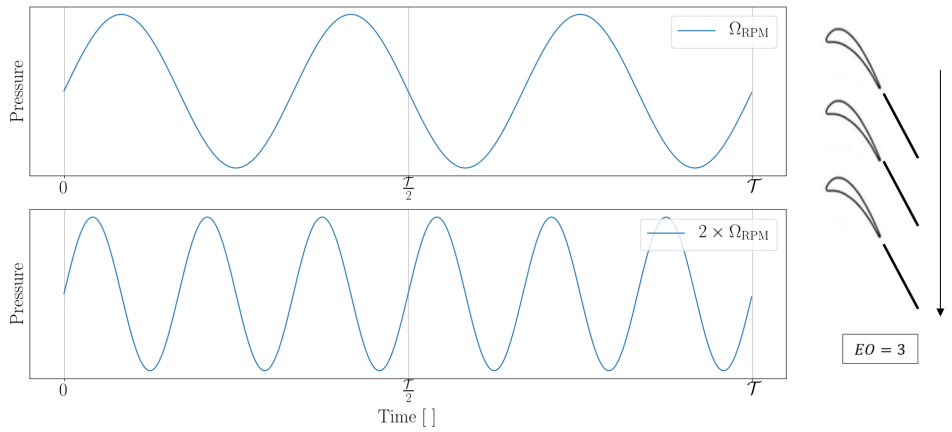

Figure 3.7: Illustration of a disturbance of 3 engine orders related to flow defects from 3 stationary upstream blades. Transient pressure variation along one full wheel rotation period $\mathcal{T}$, for two different rotational speeds Ω_{RPM} and $2 \times \Omega_{RPM}$. Variation in rotational speed results in a linear frequency increase of the transient signal by a factor of 2.

In this way, it is easily seen that the excitation frequency increases linearly with the rotational speed by a factor of the engine order, which will always be an integer quantity since it is nothing but the amount of pressure disturbances coming from flow defects of stationary blade rows. A real pressure disturbance signal will never have a perfect harmonic shape, as seen in Figure 3.8, which shows the pressure signal at a certain node of the blade of the ORCHID turbine through one stator passing period. Nevertheless, the decomposition of this pressure signal into its harmonics by means of a fast Fourier transform shows that this signal will have a harmonic content that will also increase in integers.

In the example shown in Figure 3.8 the pressure signal is taken from one stator passing period of an upstream blade row consisting of 12 stationary components. In this way, as the first harmonic is associated with the 12^{th} engine order, the second harmonic will be associated with the 24^{th} engine order and so forth.

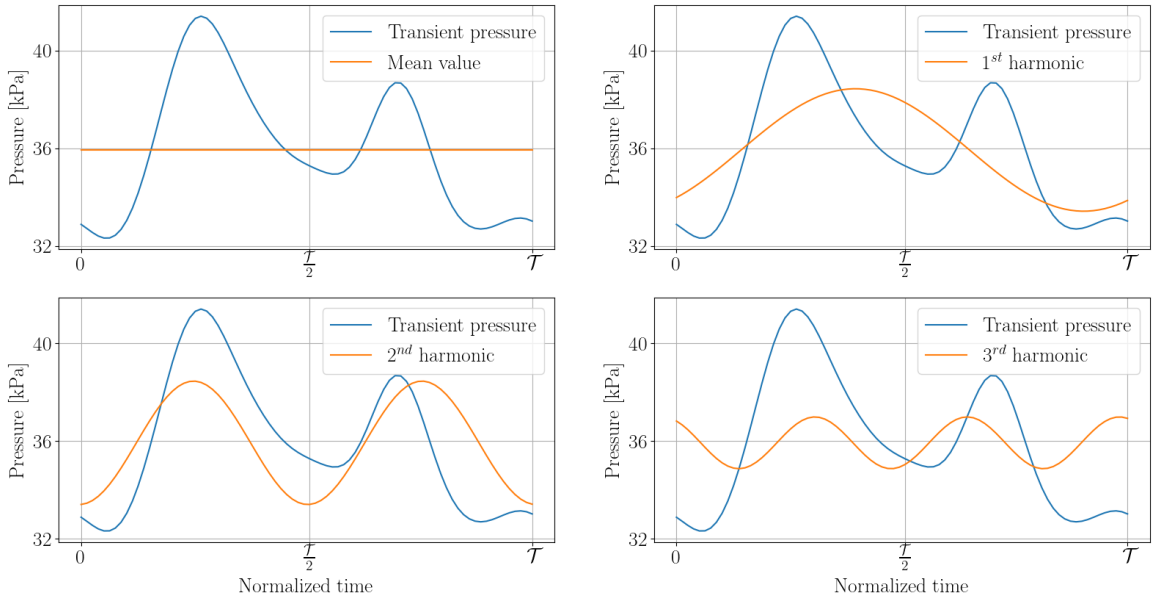

Figure 3.8: Transient pressure signal from one node on the blade surface of the ORCHID turbine rotor blade during one stator passing period $\mathcal{T}$. Representation of the mean value and the first 3 harmonics of the transient signal.

As an example the Campbell diagram for NASA rotor 67 is shown here in Figure 3.9, with the three first structural modes and 9 engine orders plotted.

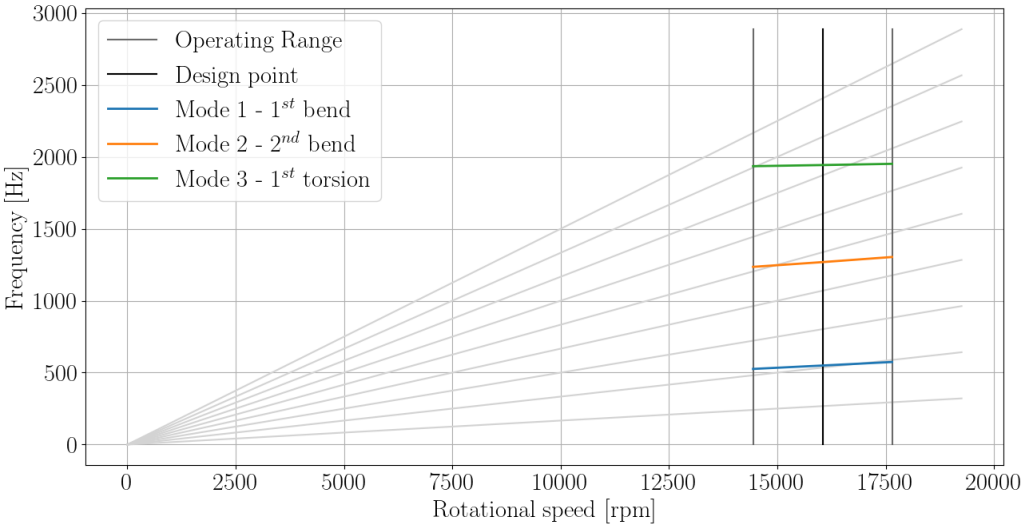

Figure 3.9: Campbell diagram of the NASA R67, shown as an example, with the 3 first structural modes and 9 engine order excitation frequencies plotted in grey. Operating range defined within a 10% range of the design speed.

In Figure 3.10 an overview regarding the process of obtaining the Campbell diagram is given. First, to obtain the modal frequencies, a pre-stressed modal analysis is made for a range of operating speeds around the design speed, in this case of 10% of the design speed. The centrifugal effects are captured, as seen by the varying natural frequencies in the diagram of Figure 3.9. Second, the excitation frequencies are computed by,

$$\omega_{\text{exc}} = EO\frac{\Omega_{\text{RPM}}}{60}, \tag{3.10}$$

where EO is the engine order and Ω_{RPM} is the rotational speed in rotations per minute. In sum, engine orders represent the amount of fixed pressure disturbances, originated by flow defects of adjacent blade rows, that result in a harmonic pressure signal to a rotating blade row. The frequency of this signal, that will be acting as an excitation force on the rotor blades, is obtained with Equation 3.10, that simply multiplies the engine order and the rotational speed.

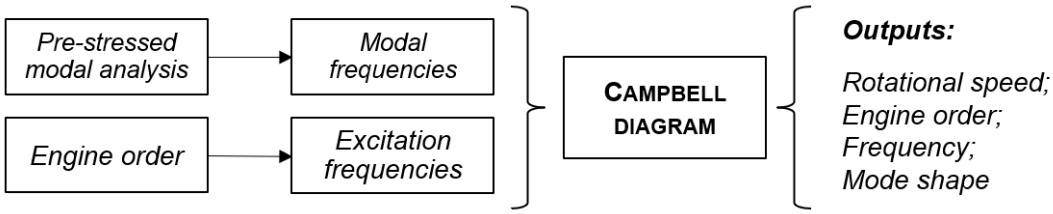

Figure 3.10: Inputs and outputs for the construction of the Campbell diagram. Inputs are obtained for each rotational speed by FEA pre-stressed modal analysis (to obtain modal frequencies) and by Equation 3.10 (to obtain excitation frequencies). Outputs are obtained by assessing resonant conditions (matching between excitation and modal frequencies).

From this diagram, the rotational speed of the resonant crossing is obtained, and so subsequent structural and fluid simulations should be performed at this speed (which may require performance maps). Also the engine order is obtained, which must be related to the number of disturbances of the machine in study (or its multiples) since these will be the ones that have a physical relevance. Besides this, also the blade vibration mode is identified, which is characterized by a certain frequency (which will be the same as the excitation frequency) and mode shape. Finally, it must be mentioned that it will be usual that a high amount of resonant crossings are identified in a Campbell diagram, and so the relevant resonant conditions must be chosen. This is made by looking not only at the relevant engine orders present in the machine, but also by identifying the lowest frequency crossings. These will be the ones that can cause higher vibration amplitudes and alternating stresses.

3.3. Interference Diagram

The interference diagram provides information regarding the circumferential distribution of the engine orders around the whole disk and how they can lead to the excitation of bladed disk modes, i.e. the modes of vibration of the blisk (blade+disk), rather than only blade modes. This information is lacking in the Campbell diagram, and so an interference diagram is necessary.

As mentioned before, bladed disk modes combine the blade modes and nodal diameters. Travelling wave modes result from this, and the vibration lag between each blade results in the rotation of the nodal diameter in the same or opposite direction as the rotational speed, corresponding, respectively, to a forward or backward travelling wave mode. If the nodal diameter stays stationary, this is the case of a standing wave mode. The maximum amount of nodal diameters of a bladed disk is limited by the

maximum number of possible axi-symmetric divisions, and so will be half the number of blades of the assembly (and is rounded down for cases of odd number of blades) [21].

As already introduced, engine orders will relate to upstream disturbances that can excite vibration modes. These are characterized by an excitation frequency which is obtained by multiplying the engine order with the rotational speed (as made for the Campbell diagram in Equation 3.10). Similarly, the excitation frequencies are computed for the interference diagram by first connecting engine orders with nodal diameters and then multiplying them by the rotational speed to obtain frequencies. Because of this, the interference diagram is assembled for one rotational speed at a time. Frequencies of natural modes are then plotted to find resonant crossings.

The main question now lays in finding the amount of engine orders that will possibly excite the bladed disk modes at certain nodal diameters. This will be related to an amount of disturbances that will be anti-symmetric to the nodal diameter of the mode. As an example, a case for a disk comprising of 4 blades is here given to provide a better understanding of this diagram, shown in Figure 3.11.

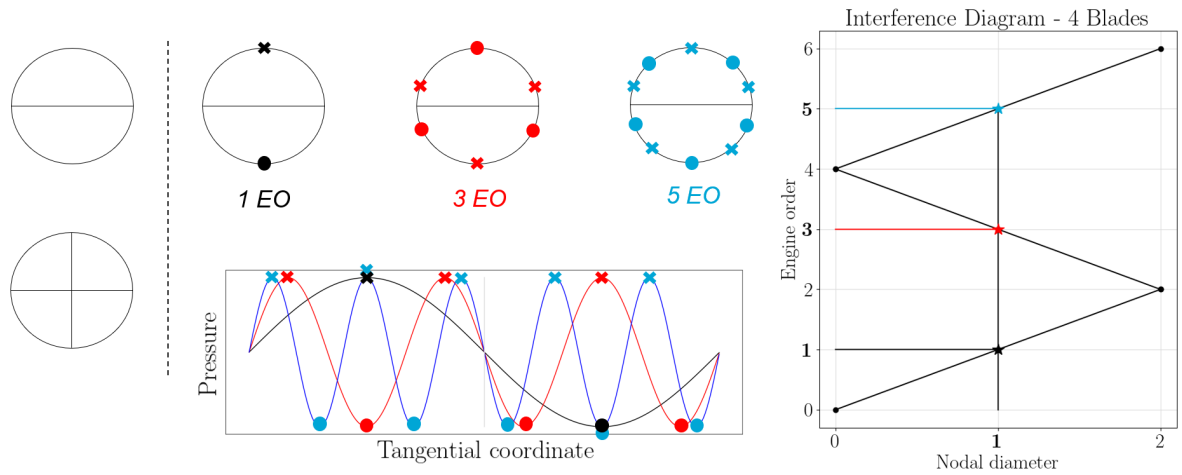

Figure 3.11: Interference diagram for a bladed disk with 4 blades - Illustration of the circumferential distribution of pressure disturbances related to engine orders 1, 3 and 5 and correlation against interference diagram. These will possibly excite the $1st$ nodal diameter disk mode.

Having 4 blades, bladed disk modes with 0,1 and 2 nodal diameters are possible to be excited. In Figure 3.11, a cross represents a high pressure area and a circle a low pressure area. The cases of 1, 3 and 5 engine order perturbations are represented around the disk circumference and plotted against the tangential coordinate. Looking at these cases, first, having a 1 engine order disturbance, it is clear to see that the 1 nodal diameter mode will be excited. Furthermore, the 3^{rd} and 5^{th} engine orders are also anti-symmetric to the 1^{st} nodal diameter, and so will also excite this mode. Referring to the interference diagram in Figure 3.11, the plot of the 1^{st}, 3^{rd} and 5^{th} engine orders against the 1 nodal diameter is highlighted.

As seen, this connection between the circumferential distribution of engine orders and the blisk vibration modes (characterized by nodal diameters), leads to the assemble of the interference diagram with the common zig-zag shape of the excitation lines. Furthermore, the lines with positive slope will

be associated with backward travelling waves, and negative slope lines with forward travelling wave modes.

To obtain the frequencies associated with the travelling wave nodes, a pre-stressed modal analysis must be conducted to capture the blisk vibration modes. In this case, a model comprising of the whole bladed disk must be used to capture the modes in question. To reduce the computational size, an analysis using a model comprising of only one section can be used if cyclic boundary conditions are applied. Exporting the frequencies and nodal diameters from the simulation performed is the last step to complete the elaboration of the interference diagram.

In sum, having obtained the rotational speed of the resonant conditions from the Campbell diagram, the interference diagram can be assembled for this operating condition. With this, the bladed disk modes are captured, and the nodal diameter determined. From here the interblade phase angle, which will be a relevant quantity when computing aerodynamic damping, can be computed for the resonant conditions to be studied.

3.4. Aerodynamic forcing

Determining the aerodynamic forcing lays in the procedure of capturing the unsteadiness that can possibly excite the blade being analysed. In terms of frequency, the unsteadiness can happen at a blade passing frequency or at low engine orders [24]. Excitations in the blade passing engine order will be related to the flow defects from stationary blade rows which will include wakes, shock waves, vortex shedding and potential interactions due to upstream influence [21]. In terms of low engine order excitations, these can arise due to asymmetries of the approaching flow to the rotating blade row. Turbochargers are a great example of turbomachines where low engine order excitations can lead to vibration issues [25].

Considering this, for the test cases considered in this thesis, the excitations will come at the blade passing frequency, and so unsteady CFD simulations including the upstream stationary blade rows must be performed in order to correctly capture these effects.

As mentioned in previous sections, the unsteady forces captured will only be able to excite certain modes if a matching condition in terms of mode shape and frequency between structural modes and excitation force exists. In Figure 3.12, an illustration of the post-processing necessary to obtain this match is given.

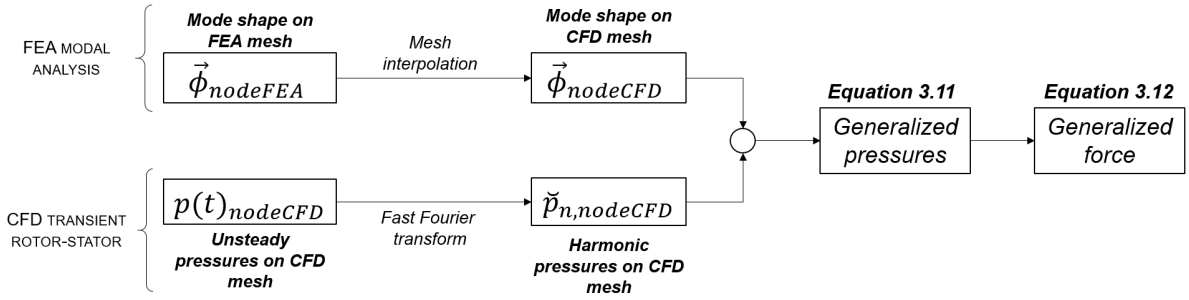

Figure 3.12: Illustration of necessary simulations and post processing to obtain aerodynamic forcing. Interpolation of mode shapes from FEA to CFD mesh (obtained from a pre-stressed modal analysis) and the fast Fourier transform of unsteady pressures (obtained from a transient stator-rotor CFD simulation). Computation of generalized pressures, using Equation 3.11, and of the generalized force using Equation 3.12.

In Figure 3.12, $p(t)_{nodeCFD}$ represents the transient pressure at each node in the CFD mesh on the blade surface, $nodeCFD$. The fast Fourier transform is used to obtain the harmonic pressures $\breve{p}_{n,nodeCFD}$, which will be a complex number at each $nodeCFD$ and for each harmonic n, characterized by a module and phase. The choice of which harmonic should be used for the aerodynamic forcing determination is associated with the engine order of the resonant crossing. Furthermore, $\vec{\phi}_{nodeFEM}$ is the mass normalized mode shape on the FEA blade surface mesh. From this, $\vec{\phi}_{nodeCFD}$, the mode shape on the CFD blade surface mesh, is obtained by interpolating between both meshes.

The interpolation from the FEM mesh to the CFD mesh and the fast Fourier transform of the unsteady pressures are made using built in functions in Python. The generalized pressures can then be computed at each node on the CFD mesh, $nodeCFD$, by taking the harmonic pressure, $\breve{p}_{n,nodeCFD}$, and projecting it onto the mode shape, $\vec{\phi}_{nodeCFD}$,

$$\breve{p}_{\text{gen},nodeCFD} = \breve{p}_{n,nodeCFD}(\vec{n}_{nodeCFD} \cdot \vec{\phi}_{nodeCFD}), \tag{3.11}$$

where $\breve{p}_{\text{gen},nodeCFD}$ is the generalized pressure and $\vec{n}_{nodeCFD}$ is the surface normal vector at node $nodeCFD$. After this, the value for the generalized force, $\breve{F}_{\text{gen}}$, can be computed by summing, for all the nodes on blade surface CFD mesh, $N_{\text{nodesBlade}}$, the forces associated with the generalized pressures computed using Equation 3.11,

$$\breve{F}_{\text{gen}} = \sum_{nodeCFD=0}^{N_{\text{nodesBlade}}} \breve{p}_{\text{gen},nodeCFD} \times Area_{nodeCFD}, \tag{3.12}$$

where $Area_{nodeCFD}$ is, clearly, the surface area associated with $nodeCFD$. The generalized force, computed using Equation 3.12, is of relevance when computing the forced response solution, and so to determine vibration amplitudes. Besides this, being easy to understand that this quantity will be directly related to the amplitudes mentioned, the use of it as an objective function in optimization procedures is a viable option to design turbomachinery towards lower vibration amplitudes and stresses [26].

3.4.1. Transient CFD methods for turbomachinery applications

Studies regarding different transient methods that handle multiple blade rows in turbomachinery have been made previously, such as in [27]. Using the test case of the NASA R67, a similar study is here presented, which was made with the goal of gaining more understanding regarding the capabilities and limitations of each method. The methods will be used to compute transient pressures, the $p(t)_{nodeCFD}$ term in Figure 3.12.

Three blade row methods were studied. The first is based in the direct application of the periodic boundary conditions, which can only be used with a model that maintains a pitch ratio of one or if the flow profile is correctly scaled in the circumferential direction (the flow profile must either be streched or compressed to account for the different domain sizes). Following this, a method that handles different pitches by the application of phase lagged boundary conditions was studied. Finally, a time inclination method was also investigated. Furthermore, regarding the transient scheme, also a comparison between the unsteady Reynolds-averaged Navier-Stokes method (URANS) and the harmonic balance method was made.

The method regarding the direct application of periodic boundary conditions is named in ANSYS CFX as the Profile transformation method. This method scales the flow profile in the circumferential direction regarding the pitch ratio and applies it in a periodic way. This method is adequate for cases where the pitch ratio is maintained as 1, but is no longer advisable for different cases, since it will not capture flow variations at the blade passing frequency [28].

Regarding the phase-lagged boundary conditions method, the ANSYS nomenclature used is the Fourier transformation method. Firstly proposed by [29], and further developed by [30], the method relies on a sampling interface that collects the necessary variables to be imposed with a time lag on the correspondent boundaries. This signal is decomposed in a Fourier series to avoid storing the entire time signal and to reduce the computational effort of its application.

The time inclination method, referred in ANSYS as Time transformation method, was elaborated by [31] and deals with the non-periodic boundaries by applying a time transformation in the circumferential direction. In this way, in the transformed set of coordinates, the boundaries can be applied as periodic. When the solution is finished, the solution must be transformed back to physical time, and the elapsed simulation time is considered as the stator simulation time. The limitation of this method lies in the pitch ratio range that is allowed, being restrained to a range between 0.6 and 1.5.

The harmonic balance methods presents itself as an alternative to the usual time integration method. It is based on the fact that turbomachinery flows have an inherently large frequency content. In this way, the unsteady flow variables can be represented by a Fourier series in time. The formulation of the flow variables in such a way results in a reduction in computational effort, since the assessment of a new flow solution for each successive timestep stops being necessary. With the harmonic balance method implemented in ANSYS, which is based in the work presented in [32] and [33], the number of harmonics to be solved for is specified, and the frequencies associated with different harmonics

are automatically associated with the blade passing frequency. For flows of higher complexities, and if the necessity of computing higher order harmonics arises, the specification of a higher number of harmonics to be solved can decrease the computational advantage of this method. Furthermore, any kind of flow features that can be happening at different frequencies than the blade passing frequency will not be captured by this method. The harmonic balance method can be used in combination with the Profile and Fourier transformation methods.

A summary of the described methods is provided in Table 3.1.

Boundary condition	ANSYS nomenclature	Number of passages
Periodic	Profile transformation	1 stator / 1 rotor or Pitch ratio of 1
Phase-lagged	Fourier transformation	2 stator / 2 rotor
Time inclination method	Time transformation	Pitch ratio between 0.6 and 1.5

Table 3.1: Summary of transient blade row methods in ANSYS CFX specifying the boundary condition imposed and the necessary number of passages for the method setup.

Without the implementation of the described methods, whole annulus simulations would have to be conducted to obtain viable results. In this way, by using any of these methods, a considerable reduction in computational size is obtained, which is fundamental for the assessment of the aerodynamic forcing in an efficient way.

3.5. Aerodynamic damping

As presented previously, the value of aerodynamic damping will determine the level of vibration amplitudes and can possibly lead to flutter. This value will be associated with the work done per vibration cycle of the fluid flow onto the structure. A positive value of work will be correspondent to energy being transferred from the fluid to the structure. The opposite situation will correspond to energy being taken away from the structure by the fluid flow, in this way dampening the initial vibratory motion.

To illustrate in a simple way the energy transfer described, the case of a two dimensional airfoil undergoing a plunging vibration mode is analysed. This motion is illustrated in Figure 3.13 (a), which shows the airfoil motion, and in Figure 3.13 (b), that plots the normalized displacement and velocity of the airfoil during one vibration period $\mathcal{T}$.

Being that during the vibration process the flow around this airfoil will change, unsteady aerodynamic forces are generated. Comparing against the velocity of the airfoil, these unsteady aerodynamic forces, if in phase, as illustrated in Figure 3.13 (c), will be acting always in the same direction as the mode, and will help the vibration process to be amplified, corresponding to positive work being supplied from fluid to structure and resulting in flutter. An out of phase force, illustrated in Figure 3.13 (d), will always be acting against the vibration, and so will help the vibration amplitudes to be reduced, corresponding to negative work from fluid to structure, representing a stable system that is able to dissipate the mechanical energy contained in the vibrations.

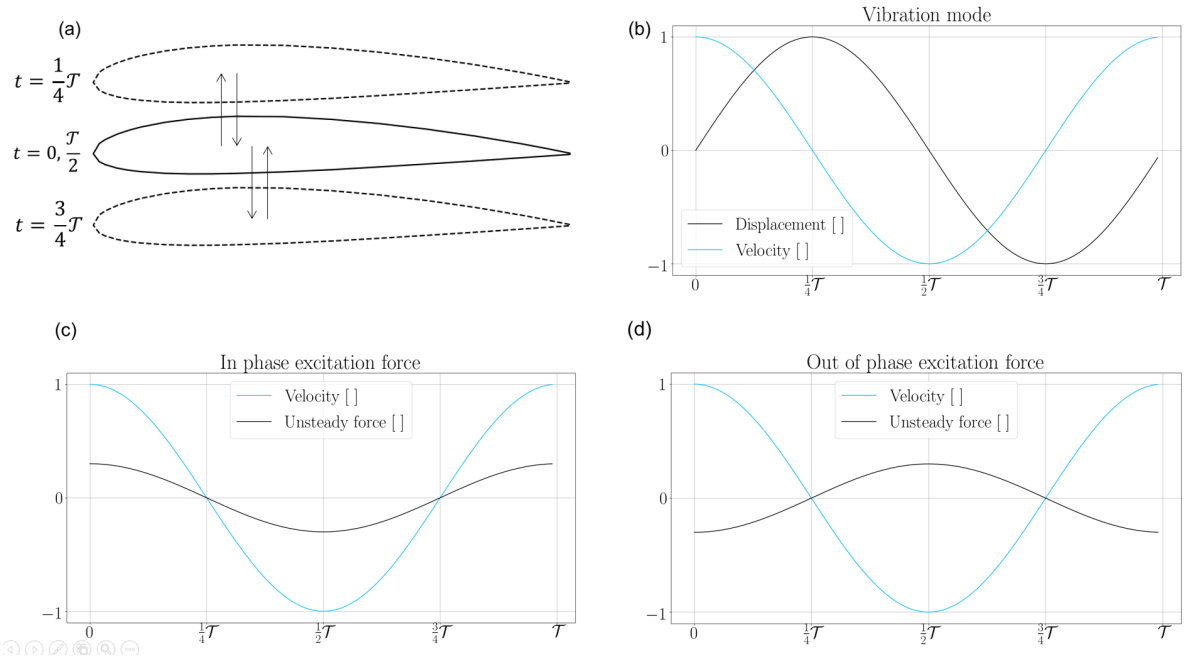

Figure 3.13: Plunging two dimensional airfoil: a) Illustration of plunging motion b) Normalized displacements and velocities; c) In phase unsteady forces in relation to velocities during one vibration period; d) Out of phase unsteady forces in relation to velocities during one vibration period.

The cases illustrated in Figure 3.13 (c) and Figure 3.13 (d) are a conceptualization of the physical process that can lead to flutter or to the dampening of vibrations by means of an aerodynamic force. It must be mentioned that the phase lag between the blade motion and the unsteady aerodynamic forces, since originated by the blade motion itself, will be dependant on a number of factors, such as the vibration mode shape, frequency and the flow features characteristic of the aerodynamic flow, which will also be associated with the machine's operating condition. In this work, high-order CFD models were used to compute these aerodynamic forces.

For any case, at each instant in time, the power associated with these forces will be $F \times v$ and, the integration of this quantity, the aerodynamic power, over one period, will yield the aerodynamic work. This simple example serves to understand how a positive aerodynamic work results in the amplification of vibration amplitudes due to an energy feed from flow to structure, and vice-versa, and how this value will be related to the phase lag between the vibration motion and the unsteady aerodynamic forces generated due to it [11].

In sum, having the data regarding the transient pressures and the surface velocities associated with the vibration cycle, the aerodynamic power can be computed, and so also the aerodynamic work. The aerodynamic damping ratio, which will be used in the forced response analysis, is computed having the aerodynamic work. In turbomachinery, due to a passage effect, the aerodynamic work will significantly change with different IBPAs. To account for this, two CFD methods to compute transient pressures are available. The aerodynamic influence coefficients method, which allows to compute all the aerodynamic damping ratio values for all possible IBPAs with only one simulation, and the direct imposition of the

IBPA on two vibrating blades, applying phase-lagged boundary conditions.

Aerodynamic influence coefficients method

The aerodynamic influence coefficient (AIC) method, described in [11], will be used to compute the entire stability curve for a certain blade mode. This method is based on the assumption that for small vibrations, the influence of a vibrating blade on the adjacent, non-vibrating blades, will superimpose linearly with a phase lag associated with the interblade phase angle in question, as experimentally demonstrated in [22].

First, considering only one vibrating blade, the force acting on its surface can be decomposed in a mean field $\bar{F}(x,y,z)$ and an unsteady field $\tilde{F}(x,y,z,t)$ acting around it,

$$F(x,y,z,t) = \bar{F}(x,y,z) + \tilde{F}(x,y,z,t). \tag{3.13}$$

The unsteady forces $\tilde{F}$ can, through a fast Fourier transform, be decomposed into a sum of harmonics,

$$\tilde{F}(x,y,z,t) = \sum_{n=0}^{N_{\text{harmonics}}} \check{F}_n(x,y,z)e^{-i\omega_n t}, \tag{3.14}$$

where $\check{F}_n$ is the harmonic force (a complex number), ω_n the frequency and where the subscript n represents the harmonic number. From Equation 3.14, the first harmonic, $n = 1$, which will correspond to the component of the unsteady force acting with the same frequency as the imposed vibration, is the one considered for the computation of the aerodynamic damping, and so the subscript n is dropped,

$$\tilde{F}(x,y,z,t) = \check{F}(x,y,z)e^{-i\omega t}. \tag{3.15}$$

The harmonic force $\check{F}(x,y,z)$, being a complex number, is characterized by an amplitude, $\hat{F}(x,y,z)$, and a certain phase. Now considering an entire blade row, in Figure 3.14 (a) a blade row is vibrating at a certain IBPA, which is an illustration of the travelling wave mode in reality, and is represented by a subscript TWM. On the right side, in Figure 3.14 (b), the AIC method setup is depicted, where only one reference blade is vibrating, represented by a subscript AIC. Equation 3.15 is valid for all the blades represented in both cases, which are numbered in relation to a reference blade and with positive values in the direction of the rotational speed.

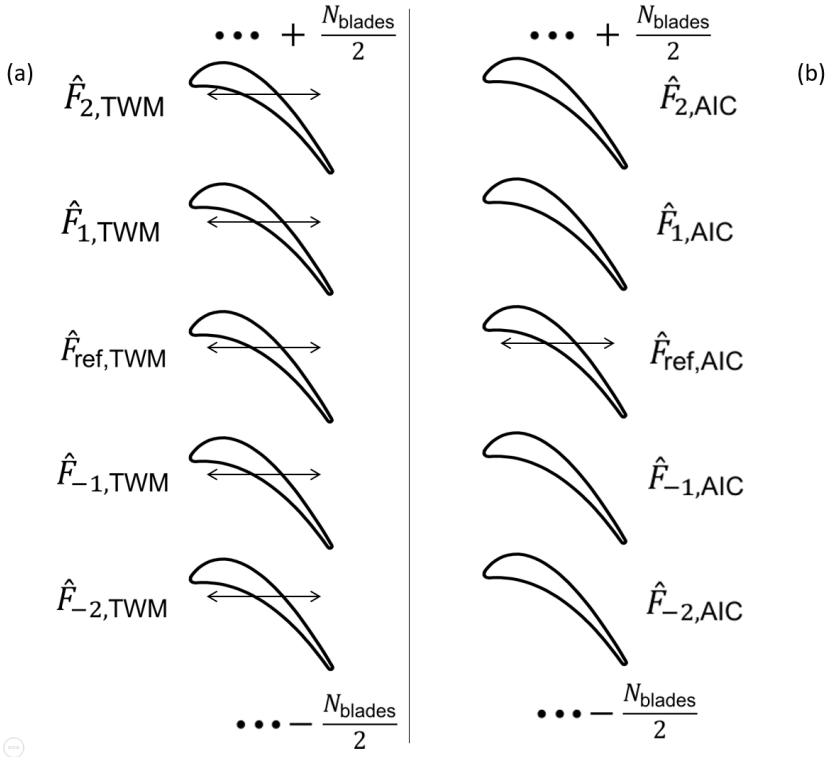

Figure 3.14: Illustration of vibrating blade rows: a) Vibration of a blade row with a travelling wave mode at a certain IBPA; b) Vibration of a blade row with only one vibrating reference blade, illustrating the aerodynamic influence coefficient method setup.

In the real case, Figure 3.14 (a), every blade is subject to the same unsteady pressure field throughout one vibration period, even if these are lagged in time for every blade, and so,

$$\hat{F}_{\mathrm{ref,TWM}} = \hat{F}_{-1,\mathrm{TWM}} = \hat{F}_{1,\mathrm{TWM}} = \ldots = \hat{F}_{-N_{\mathrm{blades}}/2,\mathrm{TWM}} = \hat{F}_{+N_{\mathrm{blades}}/2,\mathrm{TWM}}, \tag{3.16}$$

or in other words, the amplitude of the unsteady forces generated by a blade row motion at a certain travelling wave mode, is equal for each blade.

From the AIC setup, in Figure 3.14 (b), $\hat{F}_{\mathrm{ref,TWM}}$ can be obtained by the superposition of the unsteady forces on all the blades:

$$\hat{F}_{\mathrm{ref,TWM}} = \sum_{b=-N_{\mathrm{blades}}/2}^{b=+N_{\mathrm{blades}}/2} \hat{F}_{b,\mathrm{AIC}} e^{-i\times IBPA\times b}, \tag{3.17}$$

where b represents the blade numbering on the AIC method setup. In short, Equation 3.17 states that, for a certain travelling wave mode, the harmonic forces of a reference blade, $\hat{F}_{\mathrm{ref,TWM}}$, can be obtained by summing the harmonic pressures measured from the setup of the AIC method, $\hat{F}_{b,\mathrm{AIC}}$ with the correspondent phase lag associated with the blade numbering and the IBPA, $e^{-i\times IBPA\times b}$.

Knowing $\hat{F}_{\mathrm{ref,TWM}}$, the aerodynamic work for this IBPA can be computed by multiplying the unsteady forces with the blade velocities and integrating over one period of vibration, as previously mentioned. The potential of this method lays in the fact that only one set of transient data is sufficient to compute

$\hat{F}_{\text{ref,TWM}}$ for all the possible interblade phase angles. The influence of the vibration of the reference blade on the adjacent blades decreases rapidly, and so two or three sets of neighbouring blades are sufficient [34]. In this work, an overall of 7 blades were used in both test cases, just as concluded in [35] as a sufficient number.

In a more practical way, a diagram with the workflow necessary to obtain the aerodynamic damping is here shown in Figure 3.15.

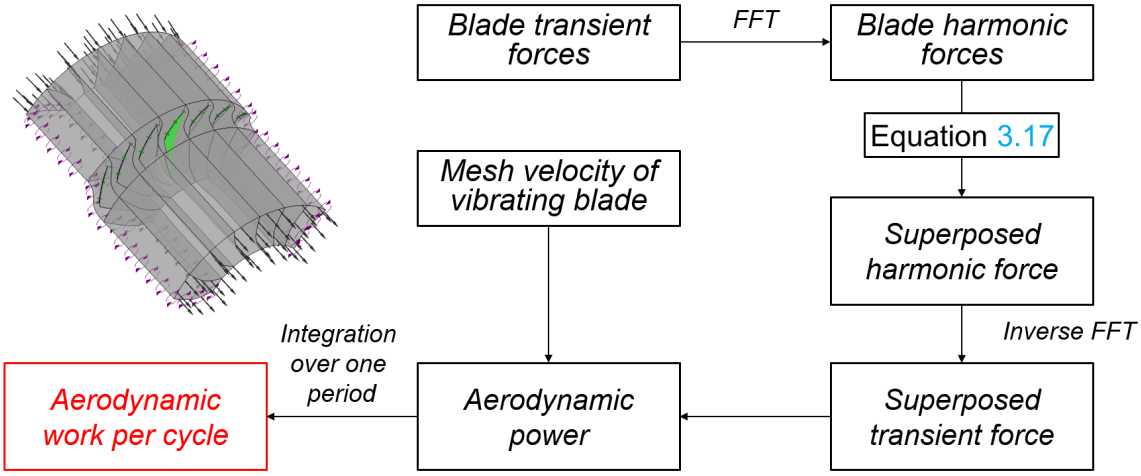

Figure 3.15: Aerodynamic influence coefficient method workflow. Superposition of aerodynamic forces in the frequency domain and multiplication of superposed transient force with mesh velocity to obtain aerodynamic power and work.

First, the transient CFD simulations with the described setup of the AIC method are performed. The transient forces on all the blades and the mesh velocity of the vibrating blade are extracted. The transient forces are decomposed on its harmonics, by a fast Fourier transform (FFT), and superposed taking the interblade phase angle into account using Equation 3.17. The superposed harmonic force is then brought back to the time domain with an inverse FFT. After this, the power can be computed,

$$P_{\text{aero},nodeCFD}(t) = \vec{F}(x,y,z,t) \cdot \vec{v}(x,y,z,t), \tag{3.18}$$

where $P_{\text{aero},nodeCFD}(t)$ is the aerodynamic power at time t and at every node on the CFD blade surface mesh $nodeCFD$. By summing up the power obtained from Equation 3.18, through the entire blade surface, the aerodynamic power for the whole blade $P_{\text{aero,blade}}(t)$ can be obtained,

$$P_{\text{aero,blade}}(t) = \sum_{nodeCFD=0}^{N_{\text{nodesBlade}}} P_{\text{aero},nodeCFD}(t). \tag{3.19}$$

Using the result obtained from Equation 3.19, and integrating this value over one vibration period $\mathcal{T}$, the aerodynamic work done per cycle W_{aero} can be computed,

$$W_{\text{aero}} = \int_{t=0}^{t=\mathcal{T}} P_{\text{aero,blade}}(t)dt. \tag{3.20}$$

Finally, Equations 3.21 and 3.22 can be used to compute the aerodynamic damping ratio, taken from [37], which will be the final value to be used in the modal superposition method to obtain the vibration amplitudes and stresses,

$$\xi_{\text{aero}} = \frac{-W_{\text{aero}}}{8\pi^3 \omega_{\text{Hz}}^2 S^2}, \tag{3.21}$$

where ω_{Hz} is the frequency in Hertz and S is the amplitude ratio of CFD and FEM simulations,

$$S = \frac{x_{\text{CFD}}}{A_{\text{max,FEA}}}, \tag{3.22}$$

where x_{CFD} is the maximum vibration amplitude for the transient CFD simulation, and $A_{\text{max,FEA}}$ is the maximum amplitude of the mode shape obtained from the FEA simulation.

Direct method

A direct method, that applies the mode shape on two adjacent blades with the correct phase lag regarding the IBPA of interest, follows the same steps as the AIC method, since Equations 3.18 to 3.22 are still used. The difference lays in the fact that one transient simulation can only output the values of aerodynamic damping for the applied IBPA. For faster computations this method is preferred since the mesh size is smaller than the AIC method and the post processing is simpler, since the superposition of harmonic forces is not required.

3.6. Forced response solution

Current methods used to obtain the forced response solution, which can then be used for analysis and optimization purposes, include the modal superposition method [36], [37], and the energy method [37], [38], [39]. The energy method is based in the fact that a balance between the destabilizing aerodynamic forcing work and stabilizing aerodynamic damping work leads to a steady-state vibration. In this way, finding an equilibrium between these quantities can output the vibration amplitudes. Assumptions regarding the work dependencies with vibration amplitude must be made [37]. In this work, the modal superposition method was chosen to conduct the analysis and is detailed in this section.

The modal superposition method is used to solve the equation of motion for systems with a higher number of degrees of freedom. This will be the case for the finite element models assembled. Equation 3.1 is generalized and expressed in matrix form,

$$[M]\ddot{\vec{q}}(t) + [D]\dot{\vec{q}}(t) + [K]\vec{q}(t) = \vec{F}_{\text{exc}}(t) \tag{3.23}$$

where $[M]$, $[D]$ and $[K]$ represent the mass, damping and stiffness matrices, which will be square matrices of size equal to the number of degrees of freedom of the system. $\vec{F}_{\text{exc}}(t)$ and $\vec{q}(t)$ are vectors of length equal to the number of degrees of freedom of the system and represent the excitation force

and the structural displacements.

Just as previously presented, the external force will be a harmonic function,

$$\vec{F}_{\text{exc}}(t) = Re\{\hat{\vec{F}}_{\text{exc}} e^{i\omega_{\text{exc}} t}\}, \tag{3.24}$$

where $\hat{\vec{F}}_{\text{exc}}$ represents the amplitude of the excitation force and ω_{exc} its frequency, that, just as for the SDOF case, imposes the frequency of the harmonic response $\vec{q}(t)$ of the system,

$$\vec{q}(t) = Re\{\hat{\vec{q}} e^{i\omega_{\text{exc}} t}\}, \tag{3.25}$$

where $\hat{\vec{q}}$ is the amplitude of the harmonic response.

The basis of the modal superposition method is the projection of $\hat{\vec{q}}$ onto a modal basis,

$$\hat{\vec{q}} = \sum_{k=1}^{N_{\text{modes}}} \vec{\phi}_k \gamma_k = [\Phi]\vec{\Gamma}, \tag{3.26}$$

where $\vec{\phi}_k$ is the mode shape of mode k and γ_k the correspondent modal coordinate. The sum of the product between the modal shapes (which can be normalized in different ways) and the appropriate modal coordinate (also referred to as modal participation factor, which is a scalar for each mode) will yield back to the coordinate $\hat{\vec{q}}$. The sum of Equation 3.26 can be written in a matrix form where $[\Phi]$ is a matrix composed of all the mode shape vectors $\vec{\phi}_k$ and $\vec{\Gamma}$ a vector composed of all the modal coordinates γ_k.

The potential of this method lays in the fact that only one scalar value by mode needs to be determined to compute the vibration amplitudes. Furthermore, at resonance conditions, it is usually accepted that one mode is enough to represent the response of the system, taken that the different modes are sufficiently spaced in frequency. Having this, the problem can be solved just as the SDOF oscillator.

Replacing the excitation force, Equation 3.24, and vibration amplitudes form, Equation 3.25, in the equation of motion for the system of Equation 3.23,

$$(-\omega_{\text{exc}}^2[M] + i\omega_{\text{exc}}[D] + [K])\hat{\vec{q}} e^{i\omega_{\text{exc}} t} = \hat{\vec{F}}_{\text{exc}} e^{i\omega_{\text{exc}} t}, \tag{3.27}$$

and using the modal basis representation presented by Equation 3.26,

$$(-\omega_{\text{exc}}^2[M] + i\omega_{\text{exc}}[D] + [K])[\Phi]\vec{\Gamma} = \hat{\vec{F}}_{\text{exc}}. \tag{3.28}$$

Multiplying Equation 3.28 by $[\Phi]^T$ on the left,

$$(-\omega_{\text{exc}}^2[\Phi]^T[M][\Phi] + i\omega_{\text{exc}}[\Phi]^T[D][\Phi] + [\Phi]^T[K][\Phi])\vec{\Gamma} = [\Phi]^T\hat{\vec{F}}_{\text{exc}}. \tag{3.29}$$

At this stage, the generalized mass, damping and stiffness matrices can be introduced respectively as:

$$[M]_{\text{gen}} = [\Phi]^T[M][\Phi], \qquad [D]_{\text{gen}} = [\Phi]^T[D][\Phi], \qquad [K]_{\text{gen}} = [\Phi]^T[K][\Phi],$$

which leads to,

$$(-\omega_{\text{exc}}^2[M]_{\text{gen}} + i\omega_{\text{exc}}[D]_{\text{gen}} + [K]_{\text{gen}})\vec{\Gamma} = [\Phi]^T\hat{\vec{F}}_{\text{exc}}. \tag{3.30}$$

Normalizing against the mass matrix and due to the orthogonality properties, the matrices introduced will only have non zero values in the main diagonal,

$$M_{\text{gen},ij} = \begin{cases} 1, & \text{for } i = j \\ 0, & \text{for } i \neq j \end{cases}, \qquad D_{\text{gen},ij} = \begin{cases} 2\xi_i\omega_i, & \text{for } i = j \\ 0, & \text{for } i \neq j \end{cases}, \qquad K_{\text{gen},ij} = \begin{cases} \omega_i^2, & \text{for } i = j \\ 0, & \text{for } i \neq j \end{cases},$$

where the damping ratio ξ, and the natural frequency ω, will both be associated with each mode. To simplify now the derivation, for each mode k,

$$(-\omega_{\text{exc}}^2 + i2\omega_{\text{exc}}\xi_k\omega_k + \omega_k^2)\gamma_k = \vec{\phi}_k^T\hat{\vec{F}}_{\text{exc}}, \tag{3.31}$$

and, finally, the modal participation factors can be computed for each mode k:

$$\gamma_k = \frac{\vec{\phi}_k^T\hat{\vec{F}}_{\text{exc}}}{(-\omega_{\text{exc}}^2 + i2\omega_{\text{exc}}\xi_k\omega_k + \omega_k^2)}. \tag{3.32}$$

Now relating back to the vibration amplitudes, using Equation 3.26,

$$\hat{\vec{q}} = \sum_{k=1}^{N_{\text{modes}}} \vec{\phi}_k \frac{\vec{\phi}_k^T\hat{\vec{F}}_{\text{exc}}}{(-\omega_{\text{exc}}^2 + i2\omega_{\text{exc}}\xi_k\omega_k + \omega_k^2)}, \tag{3.33}$$

and, if only one mode is used, the vibration amplitudes will be computed, of course, by the influence of that mode alone,

$$\hat{\vec{q}} = \vec{\phi}_k \frac{\vec{\phi}_k^T\hat{\vec{F}}_{\text{exc}}}{(-\omega_{\text{exc}}^2 + i2\omega_{\text{exc}}\xi_k\omega_k + \omega_k^2)}. \tag{3.34}$$

It must now be mentioned that, since the normalization was made against the mass matrix, also the mode shapes used for this computation must be normalized against the mass matrix, an option that can be easily chosen in the finite element solver.

Equation 3.34 represents one of the most important results to be obtained from the forced response analysis. From the finite element solver, also the modal stresses will be obtained (which are computed from the modal shapes), and will also be multiplied by γ from Equation 3.32 to obtain physical alternating stresses. Furthermore, $\vec{\phi}_k^T\hat{\vec{F}}_{\text{exc}}$ represents the generalized force, and ξ_k the aerodynamic damping ratio for mode k, concepts introduced in previous sections.

3.7. Life estimation

The Haigh diagram will be assembled to obtain a life estimation of the machine. Mean and alternating stresses, observed for a certain resonant crossing, are plotted against defined structural limits regarding HCF. The necessary quantities necessary to construct this diagram are:

- Material properties:

  Yield strength;

  Ultimate strength;

  Endurance strength;

- Structural static stresses - due to centrifugal forces;
- Structural alternating stresses - due to vibration motion.

The structural limits necessary will be the yield, ultimate and endurance strengths, which will be taken from the stress-strain and fatigue curves for a given material. From a static analysis at the resonant crossing speed the mean stresses can be obtained. On the other hand, the modal stresses will be taken from the modal analysis and will have to be multiplied by the correspondent modal participation factor before computing the physical alternating stresses. The Von Mises stresses will be the ones used since, being a scalar value, associated with the whole stress tensor, can be compared against structural limits obtained from simple tension or uniaxial experiments [40]. Having these, all the necessary components to construct the Haigh diagram are assessed. In the following, the necessary steps to build and interpret the Haigh diagram are given.

3.7.1. Material properties

The necessary structural limits to assemble the Haigh diagram will come from stress-strain curves, obtained with tension tests and from stress-number of cycles (SN) curves obtained from fatigue tests [40].

The stress-strain curve is obtained by plotting the applied stresses and the elongation produced during a tension test. The yield point represents the point at which the material's behaviour becomes plastic rather then elastic and is one of the values of interest for the elaboration of the Haigh Diagram. Besides this, the ultimate tensile strength, which is the point at which necking starts to occur, is the other necessary criteria to elaborate the diagram. A representative stress-strain curve, from [40], is shown here in Figure 3.16 to show the points mentioned.

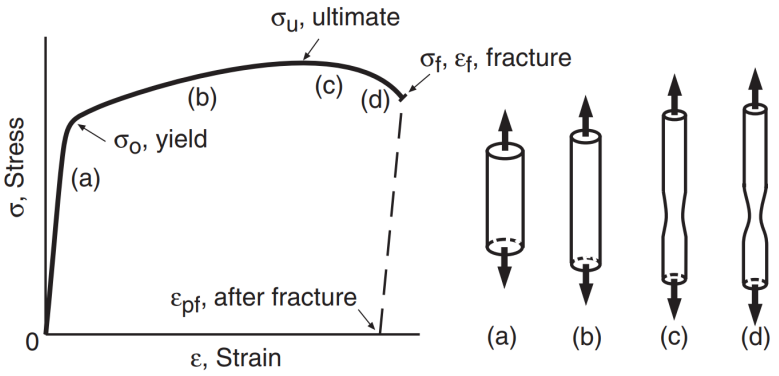

Figure 3.16: Example of a typical stress-strain curve for a ductile metal and representation of important quantities and regions. a) Elastic region; b) Plastic behaviour region; c) Necking region; d) Fracture [40]

Besides the static stresses, also an assessment regarding alternating stresses must be made. For this, the SN curves are used to obtain the endurance limit. Any material subject to a certain amount of alternating stresses can break if the necessary amount of cycles is achieved. When in the low cycle fatigue region, the material is subject to high alternating stresses, above the yield strength, and so a small number of cycles is sufficient to achieve failure. The domain of high cycle fatigue is achieved when the alternating stresses are within the elastic region, and so a higher number of cycles is necessary to achieve failure. The endurance limit represents the value of alternating stresses that, being so low, does not lead to fracture at any number of cycles, referred to as infinite life region. In Figure 3.17 a generic SN diagram is presented where the different regions mentioned are highlighted.

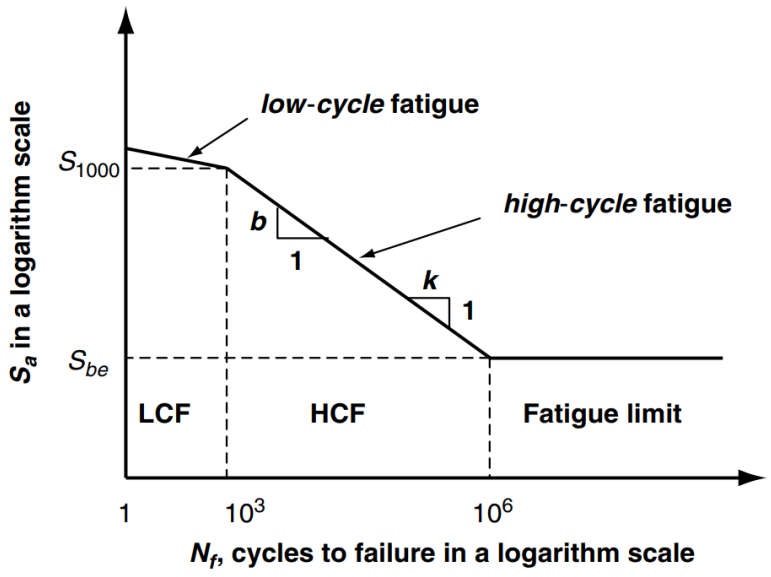

Figure 3.17: Example of a generic SN curve and representation of regions of high cycle fatigue, low cycle fatigue and infinite life region (Fatigue limit) adapted from [41].

3.7.2. Haigh diagram

Having defined the structural limits, the Haigh diagram can now be built. This diagram plots the mean stresses, due to the centrifugal forces, in the abscissa, and the alternating stresses, due to the vibration of a certain mode, in the ordinate axis [42].

The yield line is plotted by connecting the yield strength on the y and x axis. Any value of stresses under this line will mean that the sum of alternating and mean stresses is under the yield strength,

$$\sigma_{\text{mean}} + \sigma_{\text{alt}} = \sigma_{\text{yield}}, \tag{3.35}$$

where σ_{mean}, σ_{alt} and σ_{yield} are, respectively, the static (mean) stresses, the alternating stresses and the yield strength. In a similar way, the Goodman line will be plotted by connecting the endurance limit on the ordinate and the ultimate tensile strength in the abscissa,

$$\sigma_{\text{alt}} = \sigma_{\text{end}}\left(1 - \frac{\sigma_{\text{mean}}}{\sigma_{\text{end}}}\right), \tag{3.36}$$

where σ_{end} is the endurance limit. Being that the Von Mises stresses will be plotted, which are always positive, only the positive abscissa axis needs to be plotted and, the safe region, that will represent an infinite life, is found by taking the area simultaneously under the yield line, from Equation 3.35, and the Goodman line, from Equation 3.36, as depicted in Figure 3.18.

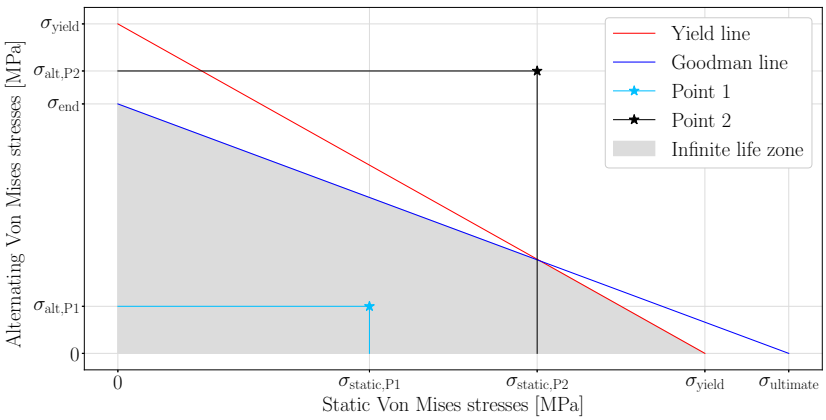

Figure 3.18: Example of a generic Haigh diagram. Plot of yield and Goodman lines and of infinite life region. Illustration of safe mean and alternating stress combination (point 1, inside infinite life region) and of unsafe stress combination (point 2, outside the infinite life region).

The safe region represented in Figure 3.18 is associated with an infinite life because the value used to assemble the diagram was the endurance limit. If the material does not present an infinite life behaviour, or if the value used to assemble the diagram was taken for a certain amount of cycles, the safe region would be associated with that amount of cycles rather than an infinite life. Stresses at nodes in the structural model will be placed on the diagram just as made with points 1 (which is inside the safe region) and 2 (outside the safe region, which will lead to fracture) in Figure 3.18.

4

Case study 1: NASA rotor 67

The NASA rotor 67 (R67) is a high-aspect-ratio, transonic axial flow fan, developed by NASA in 1989 with the purpose of conducting flow experiments using laser anemometers [43] and is shown here in Figure 4.1 along with the inlet guide vanes designed. With this, the comparison of numerical results against experimental data could be made for validation of flow analysis codes. Also in the field of aeroelasticity, the mentioned fan has been widely used to study its forced response behaviour. In this way, data is available in literature regarding this matter and was used as a term of comparison to build the methodology of forced response analysis.

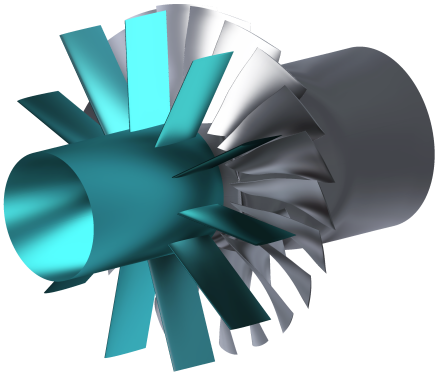

Figure 4.1: 3D rendered view of NASA rotor 67 (in black) with upstream IGV (in blue).

NASA R67	
Number of blades	22
Inlet diameter	0.514 m
Outlet diameter	0.485 m
Tip gap	1.016×10^{-3} m
Tip chord	95.22×10^{-3} m

Table 4.1: NASA R67 main geometric characteristics

In Figure 4.1, a rendered 3D view of the rotor 67, in black, and of the assembled inlet guide vane (IGV), in blue, is shown. The IGV was placed upstream of the NASA R67 and was constructed by taking a symmetric NACA 0006 profile with a constant chord of 0.80 m and extruding it linearly through

the span of the R67 blade. 11 IGV blades were chosen so that that there is a crossing of the 11^{th} engine order with mode number 4, as will be seen in further sections in the Campbell diagram. This was made so that some unsteadiness, that can possibly lead to the excitation of a vibration mode, exists in the simulations. Futhermore, a meridional view is presented in Figure 4.2 and the main geometric characteristics of the R67 are summarized in Table 4.1.

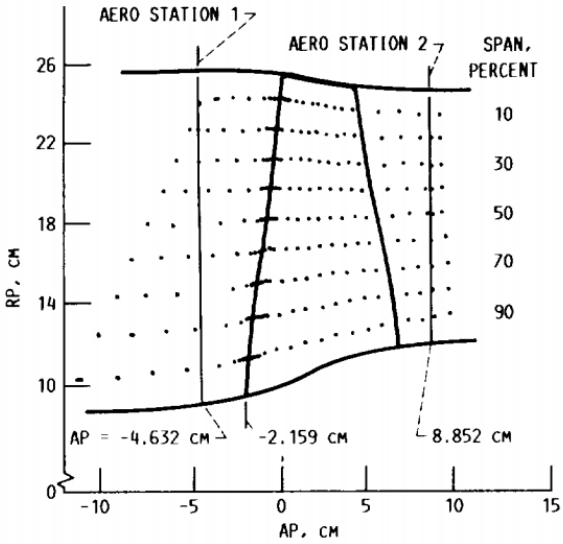

Figure 4.2: Meridional view of NASA R67 [43]

Just as mentioned before, to allow for the interpolation of quantities between FEA and CFD meshes, the construction of coincident structural and fluid models was made. These are presented in the following sections, along with the numerical settings for the simulations. The verification of the structural model was possible against results found in available literature by [36] and the validation of the fluid model against the experimental results obtained by NASA in [43].

4.1. Computational fluid dynamics model

CFD simulations were performed using the commercial software ANSYS 19.2. To obtain accurate results, a standard set of procedures was followed, detailed in the upcoming section.

4.1.1. Mesh convergency study

A mesh convergence study was performed using the steady state operation conditions found in [43]. Table 4.2 summarizes the four meshes studied by presenting the number of nodes per passage of the IGV and of the rotor 67. Mesh number 4, the finer one, was the one eventually chosen for the simulations since it provided the most reliable results at an acceptable computational cost.

Mesh	IGV	R67
1	115×10^3	144×10^3
2	226×10^3	241×10^3
3	252×10^3	271×10^3
4	313×10^3	321×10^3

Table 4.2: Mesh sizes, by number of nodes, of mesh convergence study.

In Table 4.3 the mesh quality criteria used, which comes automatically in TurboGrid are summarized.

Mesh quality criteria	
Maximum face angle	165°
Minimum face angle	15°
Maximum connectivity number	12
Maximum element ratio	20
Minimum volume	0 m^3
Maximum edge length ratio	1000

Table 4.3: Mesh quality criteria.

Grid independence was investigated by comparing the values for pressure ratio, mass flow and efficiency for increasingly fine meshes. Furthermore, the blade loadings, and values at measuring stations were used to confirm this convergence, just as exemplified in Figure 4.3, where it is clearly seen that the blade loading for meshes 3 and 4 is qualitatively similar.

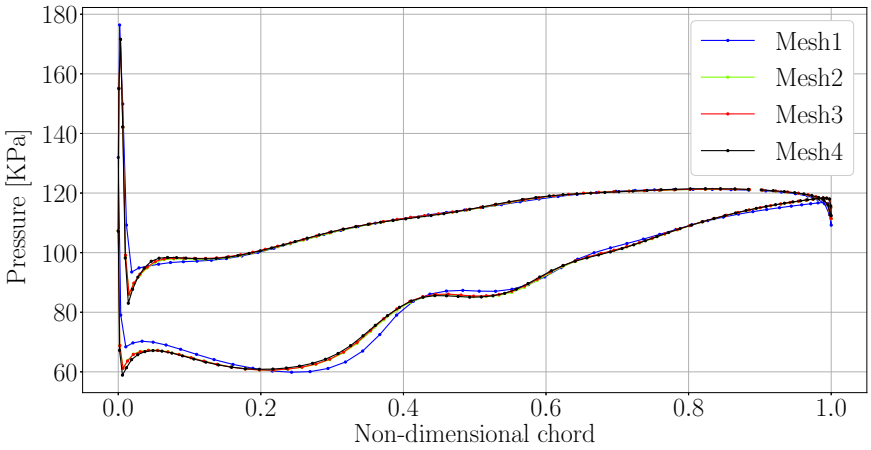

Figure 4.3: Blade loading at 50% span for different meshes of the convergence study.

4.1.2. Boundary conditions

Total conditions were imposed at the inlet of the IGV and, obtained from [43], and have been listed below,

- $p_{\text{total}} = 101325$ Pa
- $T_{\text{total}} = 288.15$ K
- Flow direction - Normal to boundary

A rotational speed of 16043 rpm is imposed on the rotating domain. Regarding the outlet boundary, at the R67 domain outlet face, a radial pressure profile was imposed, also obtained from [43], which was scaled to a value of 98% to account for the extension of the computational domain and the introduction of the IGV. In Figure 4.4 the pressure profiles are presented.

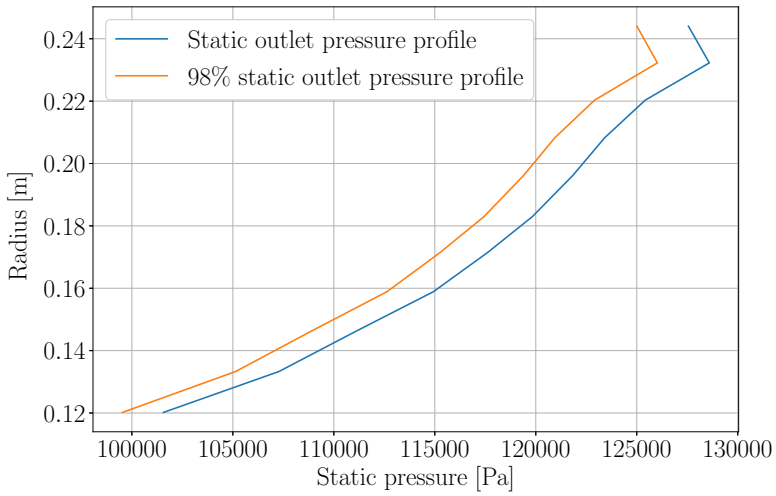

Figure 4.4: Static pressure profile imposed as boundary condition at the outlet face of the NASA R67 domain.

Furthermore, the interface between stator and rotor used a mixing plane for steady state simulations and a transient rotor-stator interface in transient simulations. The mesh connection for these interfaces was set to automatic, which chooses between a direct (one-to-one) interpolation or a general grid interface option depending on the characteristics of the interface. Further details regarding the numerical setting of transient simulations will be summarized along with the presentation of results.

The periodic boundaries were defined as rotationally periodic for the steady state simulations. For the transient simulations the periodic boundary conditions are dependent on the transformation method used. They are rotationally periodic for the case where the pitch ratio is maintained as 1 and for the time inclination method. The remainder method used was based in imposing phase lagged boundary conditions in the mentioned boundaries.

Some of the important characteristics regarding the operation of the R67 are summarized in Table 4.4. These include the experimental results reported in [43] and the results obtained with mesh 4.

NASA R67 operating conditions		
Quantity	**Experimental**	**CFD - Mesh 4**
$P_{\textbf{ratio}}$	1.63	1.599
$\dot{m}$	33.25 $\mathrm{kg\,s^{-1}}$	33.4131 $\mathrm{kg\,s^{-1}}$
$\eta_{\textbf{tt}}$	0.93	0.889

Table 4.4: NASA R67 operating conditions. Comparison of experimental values and of results obtained with mesh 4.

The introduction of the IGV, together with the extension of the outlet domain to avoid numerical reflections were reasons that eventually led to some slight differences in values of efficiency, pressure ratio and mass flow when comparing against experimental results. As will be described further, even though these differences were verified, the main flow features associated with the operation of this fan were still captured.

4.1.3. Numerical setting

The Reynolds-Averaged Navier Stokes (RANS) equations were solved in ANSYS CFX, which is an inherently implicit solver, using air modeled as a polytropic perfect gas. Other important points are here summarized in Table 4.5.

Numerical setting	
Advection scheme	High resolution
Turbulence numerics	First order
Timescale	Automatic timescale
Turbulence mode	Shear stress transport

Table 4.5: Numerical setting of CFD simulations for the NASA R67 case.

The automatic timescale was set to a value of 0.8, and so the timestep for the steady-state simulations is computed automatically. The high resolution option for the advection scheme, in ANSYS CFX, is characterized by an automatic choice of a blending factor (for different locations in the domain) to alternate or combine between first and second order accuracy.

Convergence was tracked by checking residuals, which were mantained at least at an order of magnitude of -4, by the inspection of equation imbalances, which were mantained within a range of 1% and by the inspection of flow quantities, namely by inspection of pressure values in points around the rotor blade. Finally, the post processing of results, and their comparison against experimental values in [43] was also made.

4.2. Finite element analysis model

The procedure of constructing the FEA model to be used in structural simulations was based in three main steps, summarized in Figure 4.5.

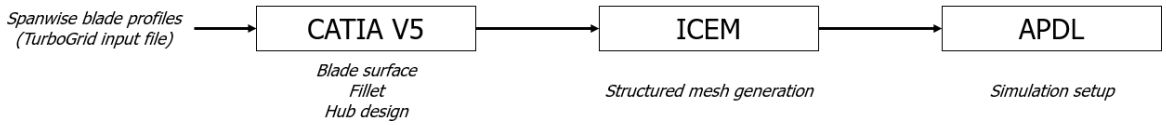

Figure 4.5: Workflow for setup of structural simulations in APDL: Geometry generation, using CATIA, of blade surface (from spanwise blade profiles), fillet and hub; mesh generation in ICEM; and finally, structural simulation in APDL.

The first step is assembling the necessary geometry using the same input file as used for the CFD mesh (which is based on the spanwise blade profiles). The blade surface can be generated with this. Furthermore, designing a hub that allows for cyclic boundary conditions to be applied was also made. Finally, a fillet in the connection between the blade and the hub was included to avoid a high concentration of stresses that would appear in a straight connection. The second step is based in generating the FEA mesh from the geometry, using ANSYS mesh generator ICEM. In this test case, a structured mesh was assembled. From here, an input file for ANSYS structural solver APDL can be generated. Some properties regarding the hub designed are here summarized in Table 4.6.

Hub angle	$16.3636°$
Hub thickness	30×10^{-3} m
Fillet radius	2×10^{-3} m

Table 4.6: Hub design data

Furthermore, in Figure 4.6, the structural mesh is presented

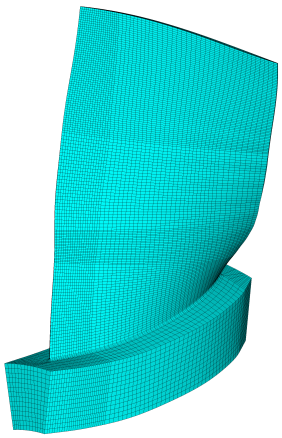

Figure 4.6: Structural mesh, generated in ICEM, of NASA R67 blade and hub cyclic sector.

A simplified hub design was assembled, and the zero displacement boundary condition was imposed in the bottom hub face closest to the rotation centre. This constrains the disk in such a way that only blade modes are being captured, and so the influence of the disk on the structural modes is disregarded. The correct determination of only blade modes was considered sufficient for this test case. Furthermore, the rotational speed is also applied as boundary condition during the structural simulation. The value for the rotational speed will vary, and so an operating range of 10% of the design

speed is defined.

Also material properties need to be defined. This can become a vast field of investigation, where many different alloys can be studied. In this study, general properties for titanium were taken from [36], presented in Table 4.7.

Titanium	
Young modulus - E	1.25×10^{11} Pa
Poisson coefficient - ν	0.27
Density - ρ	4110 kg m^{-3}

Table 4.7: Material properties for titanium taken from [36].

4.3. Campbell and interference diagram

The Campbell diagram is assembled by performing pre-stressed modal analysis at different design speeds, that captured the blade modes. It is usual that the natural frequencies vary slightly and linearly due to the centrifugal effects, and so the analysis is performed at 3 operating speeds, shown in Equations 4.1, 4.2, 4.3.

$$\Omega_{\text{min}} = 0.9 \times \Omega_{\text{design}} = 14438.7 \text{ rpm} \tag{4.1}$$

$$\Omega_{\text{design}} = 16043 \text{ rpm} \tag{4.2}$$

$$\Omega_{\text{max}} = 1.1 \times \Omega_{\text{design}} = 17647.3 \text{ rpm} \tag{4.3}$$

The minimum of the operating range, Ω_{min}, is at 90% of the design speed Ω_{design} and the maximum, Ω_{max}, at 110% of Ω_{design}. With this, the Campbell diagram can be elaborated after exporting the modal frequencies obtained and plotting them against the excitation frequencies. For this test case, the diagram is here shown in Figure 4.7 with 14 engine orders and the first 5 modal frequencies plotted for the range of operating speeds mentioned.

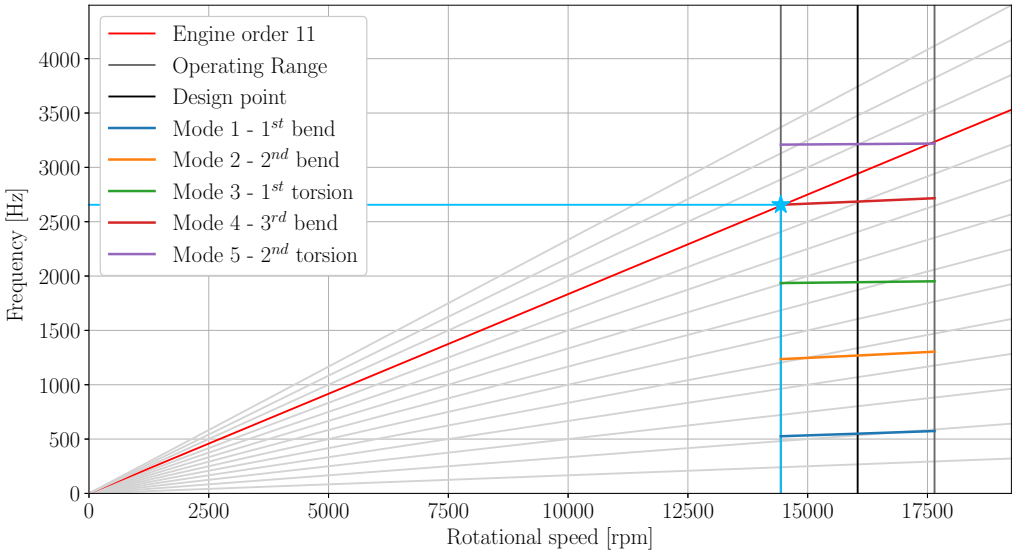

Figure 4.7: NASA R67 - Campbell diagram for blade modes with first 5 modes and 14 engine orders plotted. Blue star indicates resonant crossing to be analysed.

The resonant crossing to be analysed is the one regarding the 11^{th} engine order and mode 4 (which was identified as the 2^n torsion mode), illustrated in Figure 4.7 with the blue star. This crossing was chosen so that a pitch ratio of 1 can be easily obtained by having 1 IGV blade and 2 rotor blades, and because it represented the lowest frequency resonant conditions identified. The important information regarding this resonant crossing is here summarized in Table 4.8.

R67 resonant crossing	
Engine order	11
$\boldsymbol{\Omega}_{\text{RC}}$	14438.7 rpm
$\boldsymbol{\omega}_{\text{RC}}$	2655.7016 Hz
Mode shape	3^{rd} bending with 1^{st} torsion mode

Table 4.8: Resonant crossing details for NASA R67.

It must also be mentioned that, due to the lack of a thorough performance map, the CFD simulations used to compute the aerodynamic forcing and damping were made at the design speed. This is an approximation that considers that the main flow features that occur at the operating speed of the resonant crossing are sufficiently similar to the ones seen at the design operating speed. This does not constitute the most ideal situation to perform the analysis but was considered acceptable to save the efforts of building a performance map for the test case in question. The mode shape is shown here in Figure 4.8, where the interpolation from the FEA to the CFD mesh was already performed. The mode shape is seen to be a combination of the 3^{rd} bending mode with the 1^{st} torsion mode since 2 bending nodal lines are clearly identified at the root of the blade and around midspan, and another combined torsion and bending nodal line is identified, as shown in Figure 4.8.

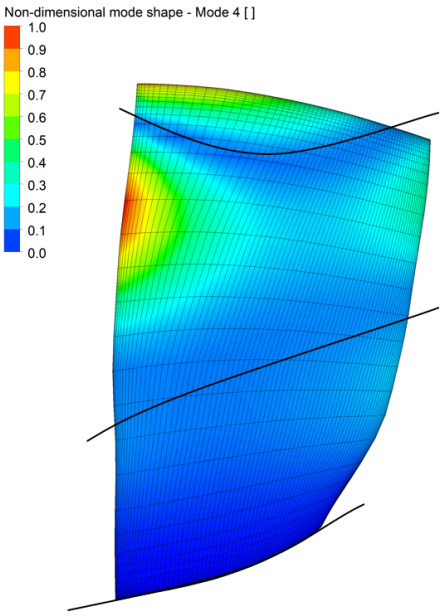

Figure 4.8: Normalized mode shape 4 of NASA R67 interpolated onto CFD mesh. Illustration of nodal lines in black.

The interference diagram was computed at the resonant crossing's speed, by performing a pre-stressed modal analysis at the mentioned speed and with cyclic symmetry boundary conditions. This diagram is shown here in Figure 4.9. The crossing identified previously is here seen clearly occurring at the 11^{th} nodal diameter. This will correspond to an IBPA of $180°$,

$$IBPA = \frac{360 \times ND}{N_{blades}} = 180°. \tag{4.4}$$

In Figure 4.10, the blisk mode shape is presented. It is seen that the deformation on the blades is representative of the blade mode shape and that the phase between every two adjacent blades is of $180°$, characteristic of the disk mode with 11 nodal diameters.

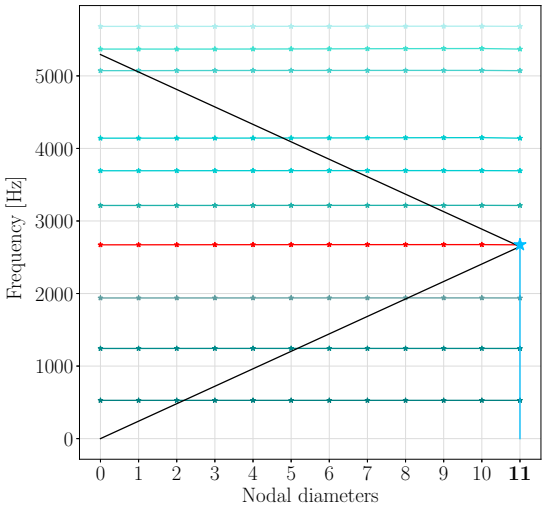

Figure 4.9: Interference diagram for NASA R67 for minimum operating speed. Blue star representing resonant crossing.

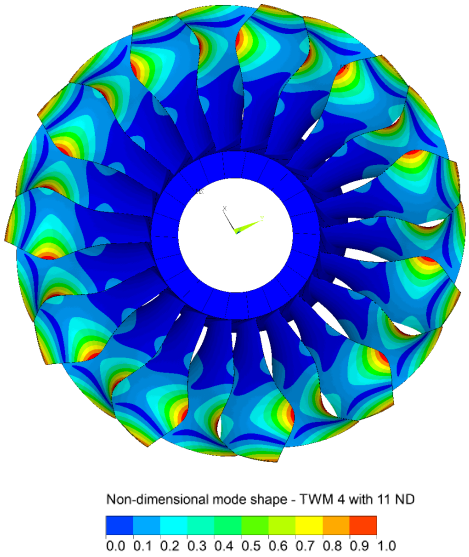

Figure 4.10: Normalized travelling wave mode shape of NASA R67 mode 4 with 11 nodal diameters.

From the interference diagram shown, it is also seen that the disk influence on natural frequencies is not relevant due to the zero displacement boundary conditions applied, since no change is seen between the different nodal diameter modes. A summary regarding the resonant conditions can now be made. The excitation coming from 11 engine orders will cross mode 4, a combined bending mode of 3 nodal lines with a 1 nodal line torsion mode, at a rotational speed of around 90% of the design speed and a frequency of 2655.7016 Hz. This engine order is seen to excite the 11 nodal diameter travelling wave mode characterized by an IBPA of $180°$.

4.4. Aeroforcing

In this section, the harmonic pressures computed will be commented in relation to the mean flow field obtained with the steady state simulations. These comments will be based on surface contours of harmonic and generalized pressures.

The relevant flow features of the rotor 67 are the shock waves and the hub corner stall [44] can be described. The complex system of shock waves is stronger close to the tip of the blade and consists of an oblique shock wave at the leading edge and a passage shock wave that spans from the pressure side of one blade - closer to the leading edge - to the suction side of the adjacent blade - closer to the trailing edge. The pressure contour at 90% span is shown here in Figure 4.11 to illustrate the shock wave system described.

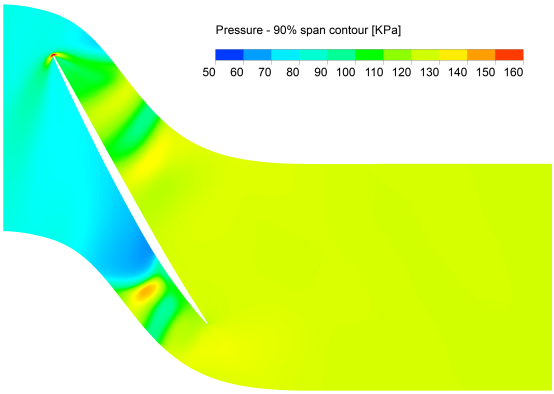

Figure 4.11: Static pressure contour at 90% span from steady state simulation.

Another flow feature of relevance, that is usual in the operation of transonic fans such as the rotor 67, is the hub corner stall [44], characterized by flow separation at the trailing edge, close to the hub, on the suction side of the blade. The velocity contour shown here in Figure 4.12 clearly shows the separation occurring close to the trailing edge at a span of 10%.

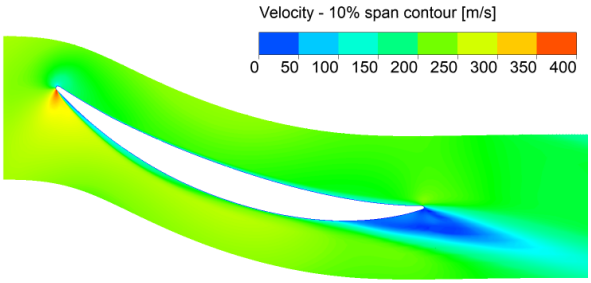

Figure 4.12: Velocity contour at 10% span from steady state simulation.

Understanding what kind of features are present in the flow, and their location on the blade, will be of relevance when looking at unsteady pressures related to the influence of the upstream blade row or the vibration of the blade. It will be expected that higher unsteadiness will be present in these locations.

Different sets of transient simulations were performed with the NASA R67 test case, for which the results are presented in the following section. The set of results used as reference, and presented here, corresponded to the model that maintains a pitch ratio of 1 using the URANS transient method of ANSYS CFX. A transient stator-rotor interface was used along with the profile transformation method of CFX. The number of timesteps per period was set to 80, which corresponded to a timestep of 4.24×10^{-6} and approximately $0.4°$ of rotation per timestep.

The contours of harmonic pressure are shown in Figures 4.13 and 4.14. It is seen that in a general way a higher amount of unsteadiness is seen on the pressure side. Besides this, high values of unsteady pressures are seen close to the leading edge, related to the direct passage through the wake

created by the upstream IGV. Near the hub, the unsteadiness found closer to the trailing edge is associated with the hub corner stall mentioned previously and it is seen that, even if the separation takes place on the suction side, a high influence on the pressure side of the adjacent blade is assessed. Finally, the unsteadiness due to the passage shock wave is spanning from around 50% span until the blade tip on the suction side. Just as mentioned previously this influence is also felt on the pressure side with quite some strength. As an idea, the higher pressure fluctuations have a value of around 3 kPa.

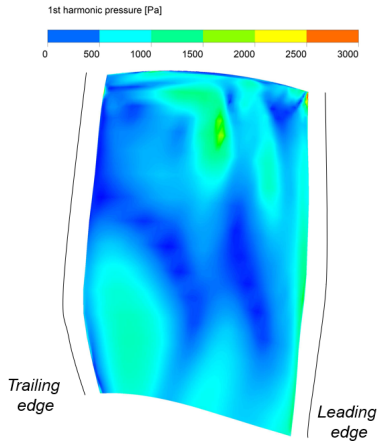

Figure 4.13: Blade surface contour, on the pressure side, of 1^{st} harmonic pressure of NASA R67, obtained from stage transient CFD simulations.

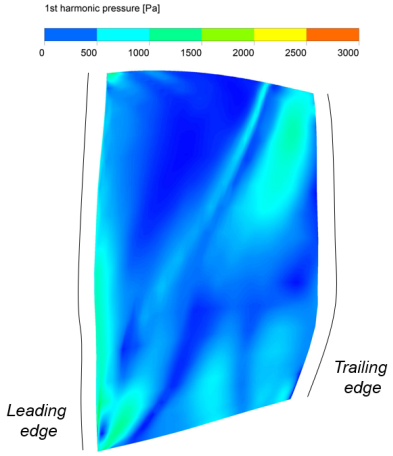

Figure 4.14: Blade surface contour, on the suction side, of 1^{st} harmonic pressure of NASA R67, obtained from stage transient CFD simulations.

The generalized pressure is here presented in Figures 4.15 and 4.16. These values came from the projection of the previously shown unsteady pressures onto the mode shape 4. The mode shape is normalized against the mass matrix and has yet no real physical value, and so also the generalized pressure contours serve only to gain an idea of where in the blade the unsteady pressures are matching more closely with the mode shape. In a general way, the unsteadiness closer to the tip of the blade are of more concern, with a bigger impact on the leading edge and on the pressure side.

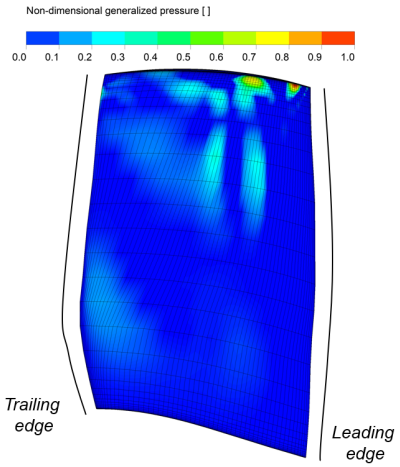

Figure 4.15: Blade surface contour, on the pressure side, of generalized pressures due on the NASA R67.

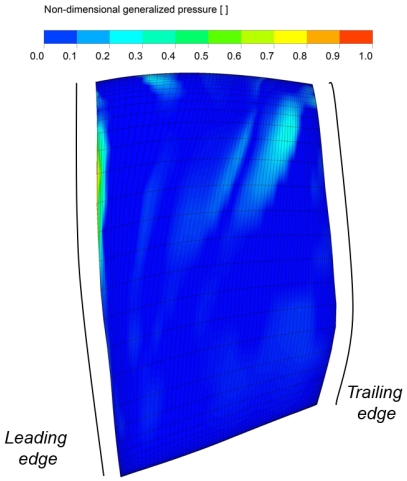

Figure 4.16: Blade surface contour, on the pressure side, of generalized pressures on the NASA R67.

4.4.1. Transient CFD methods for turbomachinery applications - Results

The models assembled to study the different transient methods are summarized in Table 4.9.

Pitch Ratio 1 **Profile transformation**		**Phase lagged BC** **Fourier transformation**		**Time inclination** **Time Transformation**
URANS	*Harmonic balance*	*URANS*	*Harmonic balance*	*URANS*
1 IGV / 2 R67		2 IGV / 2 R67		2 IGV / 3 R67
Pitch ratio = 1		Pitch ratio = 0.5		Pitch ratio = 0.75

Table 4.9: Different models used to handle of unequal pitch ratios in aeroforcing transient simulations.

The comparison of the different results was performed by inspection of harmonic and generalized pressure contours on the blade surface. Also the values of the generalized force, which in the end is the most important one in terms of forced response analysis, were compared.

In Figure 4.17, the values for the generalized force are presented with a normalization against the Pitch ratio 1 (PR1) model using the time integration method. The values obtained with the transformation methods showed very good relations with the reference value. The highest deviation is seen for the PR1 model using the harmonic balance method and that, even so, only shows a slight overestimation of around 5% of the reference value. It is also worth mentioning that the results obtained using the Fourier transformation model using the harmonic balance method are not presented since convergence was not achieved in a reasonable amount of computational time.

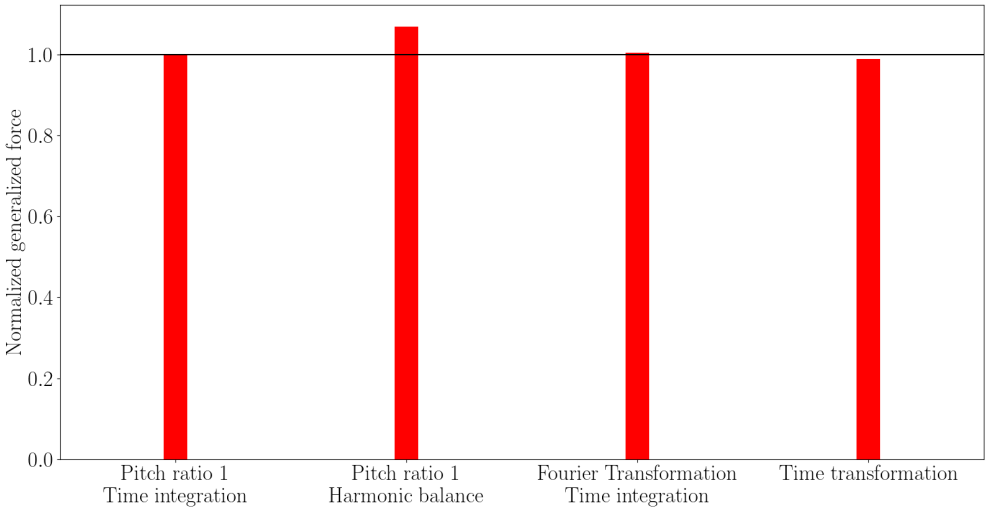

Figure 4.17: Normalized generalized force using different transient methods.

To gain understanding regarding the potential of these methods, the domain size of each model can be compared against a whole annulus simulation. In this case, by using the pitch ratio 1 model the computational domain size is reduced by a factor of 11, for the Fourier transformation model of around 8 and for the Time transformation model of around 7. As is clear by these numbers, the main advantage of the presented methods is to reach smaller domain sizes for cases where the pitch ratio cannot be maintained as 1 when reducing the model size from the full model. In these cases, the methods studied show a big potential to provide reliable results in terms of the generalized force with competitive computation times. Being that all the methods presented show viable results, the most adequate one should be chosen for a certain machine by assessing which model leads to the least amount of blade passages.

4.5. Aerodamping

The unsteady simulations to determine aerodynamic damping were made using 7 passages having the middle blade vibrating with the mode shape and frequency from the resonant crossing defined. 80 timesteps per period were defined, yielding to a timestep of 4.656×10^{-6} seconds. Having 7 blades, the computational domain is wide, and so the unsteady effects from the middle vibrating blade are small in the last blade passage, allowing for periodic boundary conditions to be applied.

The main output from the transient analysis with the blade vibration is to determine the aerodynamic damping ratio to the whole range of IBPA values possible to occur by using the aerodynamic influence coefficient method [11]. This result is here presented in Figure 4.18.

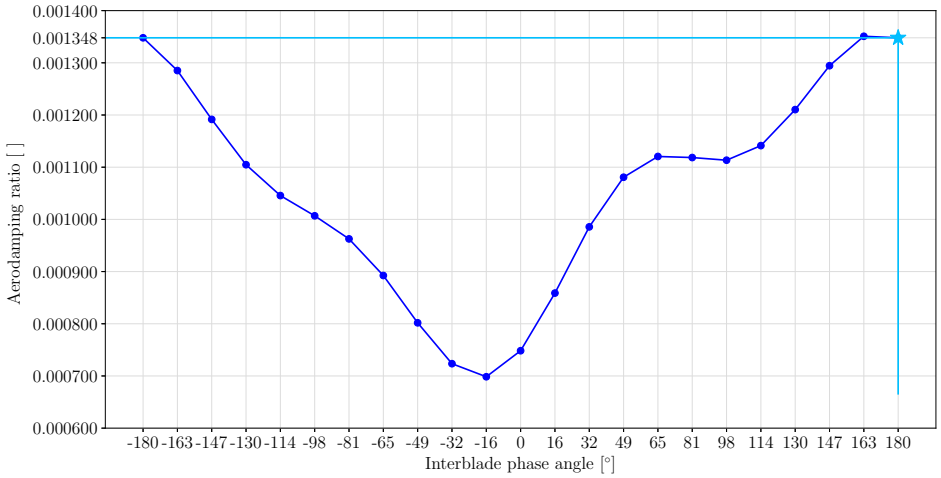

Figure 4.18: NASA R67 stability curve for mode 4. Aerodynamic damping ratio for all possible IBPA values.

The first conclusion to be taken from the stability curve is that all the damping values computed are stable, having a positive value. Furthermore, the least stable mode is associated with the IBPA of $-16°$ at a value of around 0.0007.

The IBPA associated with the resonant crossing under investigation is actually seen to be one of the most stable modes. The aerodynamic damping value associated with it is of $\xi_{\text{aero},180} = 0.00134793$

In Figure 4.19, the blade loadings for a span of 50% of stage and rotor only simulations are shown. Correctly representing the stage uniform flow without the presence of the stator is an important step to obtain feasible results in terms of aerodynamic damping. It is seen that the overall trend is well captured between the two simulations and at similar pressure levels. The discrepancies seen were considered to be acceptable for the test case presented. Moreover, some uncertainty related to the aerodynamic damping value, due to this fact, will be introduced in following computations as will be discussed.

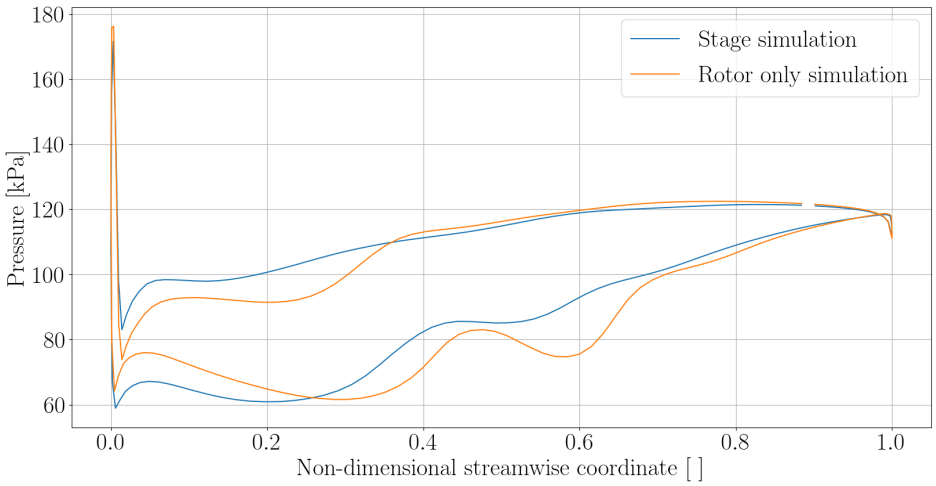

Figure 4.19: Comparison of blade loadings at 50% span for the NASA R67 stage and rotor only steady state simulations.

4.6. Forced response and life estimation

As mentioned previously, to perform the forced response analysis, the modal participation factors must be computed using Equation 3.32, in order to obtain the physical alternating stresses. The generalized force and aerodynamic damping ratio are two of the necessary parameters and are here presented in Equations 4.5 and 4.6. The generalized force is the summation, for the entire rotor blade, of the harmonic pressures (translated into forces) and projected onto the mode shape of interest. Also the aerodynamic damping value is associated with the vibration mode shape of interest.

$$\check{F}_{\text{gen}} = 3.462 - 7.108i \tag{4.5}$$

$$\xi_{\text{aero},180} = 0.00134793 \tag{4.6}$$

The modal frequency $\omega_{\text{mode 4}}$, which is equal to the excitation frequency ω_{exc}, was used for the forced response analysis,

$$\omega_{\text{mode 4}} = \omega_{\text{exc}} = 2655.70 \text{ Hz}. \tag{4.7}$$

As it was previously mentioned, being that the CFD simulations to compute the aerodynamic forcing and damping were taken as the design speed, in order to avoid the necessity of elaborating a compressor map for the resonant crossing speed, the assumption that the flow features at these two speeds are sufficiently similar is taken. Taking this into account, an uncertainty of 10% on the generalized force and aerodamping values was investigated. This was done by increasing the value of the generalized force by 10% and reducing the aerodynamic damping ratio by 10%. The Haigh diagram for these conditions is then showed here in Figure 4.20.

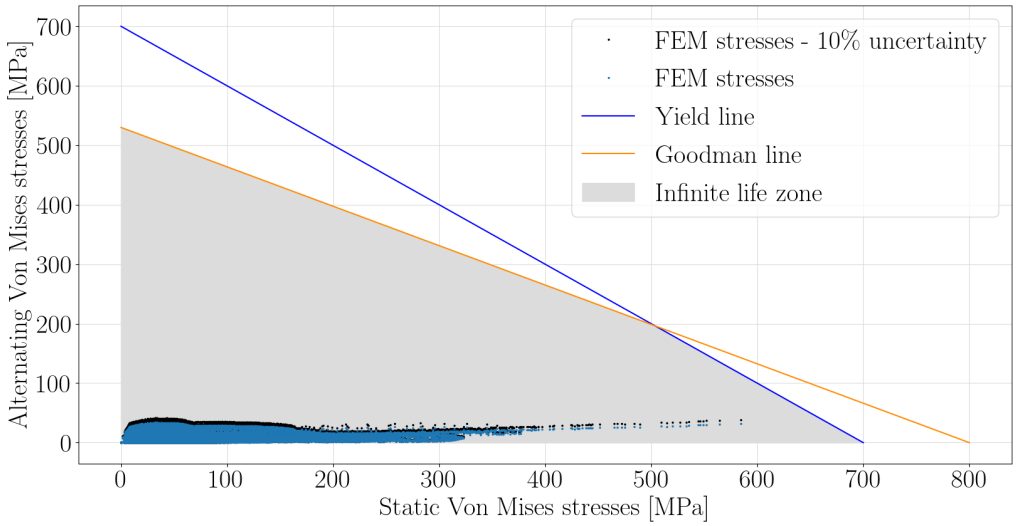

Figure 4.20: Haigh diagram for NASA R67. Excitation of blade mode 4 with 11 nodal diameters and 11 engine orders.

It is seen here that the stresses computed are all within the structural limits defined for an infinite life of the machine. Furthermore, the uncertainty influence is well identified but still not sufficient to overcome the mentioned limits. The high centrifugal stresses, associated with the alternating stresses are the ones that present itself to be closer to the limits. These points correspond to the connection of the blade with the hub, in the fillet created, where a high concentration of stresses was expected, as seen in Figure 4.21 and 4.22, which display the static and modal stresses, respectively.

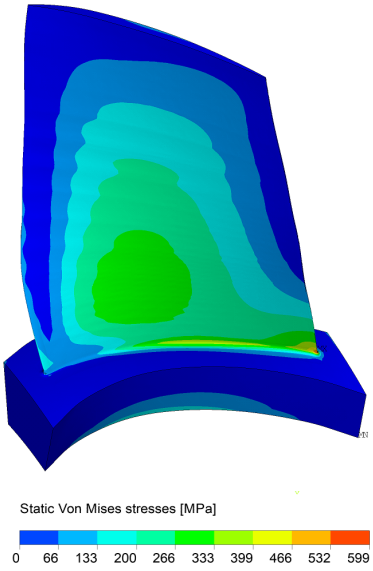

Figure 4.21: Static stresses on the NASA R67 model due to centrifugal forces.

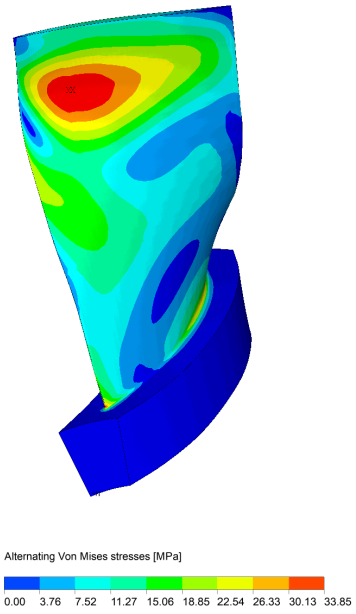

Figure 4.22: Alternating stresses on the NASA R67 model due to the vibration with mode shape of resonant crossing.

The static stresses presented in Figure 4.21 show stress concentrations at the fillet which fade away while moving towards the blade tip. This is an expected contour for stresses due to centrifugal effects. In terms of modal stresses, the contour shown in Figure 4.22 shows higher values for regions of bigger blade curvature, such as the region close to the blade tip. It is a positive fact in terms of structural integrity that the regions of high modal and static stresses mismatch.

In conclusion, the results presented for the case of the NASA R67, show that the excitation of the 4^{th} natural mode by means of the inlet guide vanes, does not pose a problem to the structural integrity of the rotor in terms of high cycle fatigue.

4.7. Conclusions

Three main objectives achieved with this test case are:

- Synthesis and validation of the forced response analysis chain;
- Assessment of transformation methods in ANSYS CFX;
- Assessment of the structural integrity of the NASA R67 for the resonant conditions identified.

As the methodology was assembled, also the acquaintance with the different necessary software was essential. For the FEA, the CAD software CATIA was used to assemble the geometry, the structural mesh was built with ICEM and the simulations themselves were performed using ANSYS APDL. For the CFD analysis, ANSYS CFX was used and the mesh was made using TurboGrid. Moreover, most of the post processing presented throughout was made using Python scripts, developed during the course of this work. The process of assembling the methodology was then dependent on many different software, and so the use of this test case in order to gain confidence with all of them was vital.

As mentioned, for the aerodynamic forcing simulations, a study of different transformation methods available in ANSYS CFX was performed and consistency between the different methods was assessed. The different simulations gave very similar results in terms of the generalized force for all the cases and showed agreeing contours of harmonic and generalized pressures, showing that these options provide a viable alternative for cases where a reduction of the computational domain cannot be obtained while maintaining a unity pitch ratio. Furthermore, the use of harmonic balance instead of a time-marching method was also made using the possible models. The combination of the Fourier transformation model and the harmonic balance method yielded convergence problems and ended up being abandoned. The use of a model maintaining a pitch ratio of 1 and the harmonic balance method provided viable results in a shorter computation time, also showing the potential of this method as a faster alternative to time-marching methods.

In terms of structural integrity, it is concluded that the excitation of the 4^{th} mode, the 3^{rd} bending combined with the 1^{st} torsion mode, by means of the elaborated inlet guide vanes, does not pose a problem to the structural integrity of the rotor regarding high cycle fatigue. This conclusion is taken by direct inspection of the Haigh diagram and it has certain underlying causes:

- The damping values, from an aerodynamic origin, are positive, and so are associated with a stable mode that is able to contain the vibrations encountered;
- The aerodynamic forcing coming from flow defects generated by the inlet guide vanes is not sufficient to excite vibrations that can overcome the structural limits;
- A mismatch in location of high modal stresses and static stresses is seen:

  The mode shape encountered shows the highest modal stresses at the top of the blade, where the static stresses are smaller and the structural limits are higher;

  The modal stresses encountered close to the connection between the blade and the hub (high static stresses), are not enough to overcome the structural limits imposed.

5

Case study 2: Organic Rankine cycle turbine

The ORCHID turbine studied in this chapter, referred throughout as mini-ORC turbine, has been designed at TU Delft and it has a power output of about 10kW. Its main application is the waste heat recovery for long-haul truck engines. The challenges associated with its design lay in the lack of guidelines for small scale turbines operating with organic fluids. Furthermore, the small mass flow rate and the non-ideal compressible fluid dynamics increase the complexity of such a design.

The designed turbine has 12 stators and 19 rotor blades which were an outcome of the optimization performed in [3]. In Figure 5.1, a rendered 3D view of this machine is given.

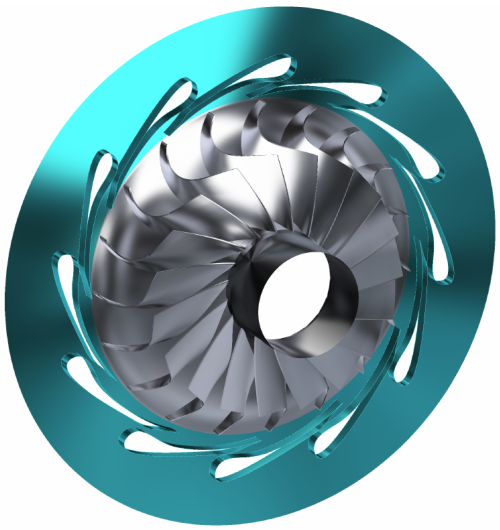

Figure 5.1: 3D rendered view of the mini-ORC turbine.

Table 5.1 summarizes some of the important values regarding the geometric configuration of this machine, with emphasis given to the small dimensions of the turbine, that has an inlet diameter of only $3.48cm$.

Mini-ORC characteristics	
Stator number of blades	12
Rotor number of blades	19
Inlet diameter	34.8×10^{-3} m
Outlet diameter	8.20×10^{-3} m
Tip gap	0.1×10^{-3} m

Table 5.1: Mini-ORC main geometric characteristics.

A meridional view is shown in Figure 5.2. The radial inflow configuration was chosen since it is, arguably, the most suitable configuration for this type of machine due to the reduced tip leakage losses and the possibility of handling a high volumetric flow ratio with only one stage [3].

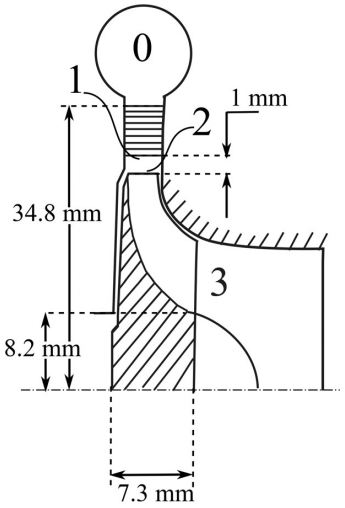

Figure 5.2: Mini-ORC meridional channel [3].

5.1. Computational fluid dynamics model

Similarly to the previous test case, the procedures followed to obtain quality CFD results are here detailed.

5.1.1. Mesh convergency study

In [3] the fluid dynamic design for the ORC turbine was made by means of a meanline design and an optimization based in CFD simulations. A mesh convergence study was performed, and so the necessity to conduct one in the current study was avoided.

A very fine mesh resulted from this mesh convergency study, with around 2 million nodes for the stator passage and 1.5 million nodes for the rotor passage.

5.1.2. Boundary conditions

The rotational speed of the turbine is of 98119 rpm and the inlet boundary conditions, applied at the inlet of the stator domain, are:

- $p_{\text{total}} = 1809.3$ kPa
- $T_{\text{total}} = 573.16$ K
- Flow direction - Normal to boundary

The static pressure was defined as the outlet boundary condition, at the outlet of the rotor domain, and was set to a value of 44.3 kPa.

Furthermore, just as for the previous test case, a mixing plane was applied to the stator-rotor interface for the steady state simulations. For the transient aeroforcing simulations, a transient stator-rotor interface was applied. Besides this, the mesh connection for these interfaces was also maintained as automatic. Rotationally periodic boundary conditions were applied for the steady state and transient aeroforcing simulations, since the time inclination method was used.

Having this, in Table 5.2 the important characteristics of the mini-ORC turbine operation are presented. Emphasis is given to the small mass flow of the turbine that is able to output the mentioned power of 10.6 kW and with an optimized efficiency of 84%.

Mini-ORC characteristics	
$\dot{m}$	$0.132\ \text{kg s}^{-1}$
P	10.6 kW
η_{ts}	0.84

Table 5.2: Mini-ORC operating parameters.

5.1.3. Numerical setting

One major difference, in comparison with the numerical setting of the previous test case, lays in the working fluid. The organic fluid to be used is Siloxane (MM), also known as hexamethyldisiloxane. Since the thermodynamic behaviour of this gas does not follow the ideal gas equation, for the CFD simulations, the necessary properties were obtained by the use of look up tables included in ANSYS CFX.

The high molecular weight of Siloxane MM, of $162.37752\text{g mol}^{-1}$ [45], which is around 5 times higher than for air, is of relevance since it will result in a low speed of sound. With this, a supersonic flow occurs, reaching, in this case, values of Mach number of more than 2 in the stator, resulting in a complex system of shock waves.

The remainder relevant numerical setting parameters were the same as the previous test case, which were summarized already in Table 4.5. In this case, the automatic timescale was set to 0.4 and the turbulence numerics was switched to the high resolution option (which blends 1^{st} and 2^{nd} order

accuracy in different regions of the computational domain). Convergence was assessed by inspection of residuals, which were set to an order of magnitude of -7, the imbalances were kept in a range of 1% and the inspection of flow quantities such as mass flow, efficiency and pressure at certain points was made.

5.2. Finite element analysis model

The construction of the FEA model followed the steps presented for the previous test case. These were based in the construction of the blade and hub geometry, mesh generation and structural simulation setup. For this test case, to simplify the construction of this model, an unstructured mesh was generated, shown in Figure 5.3. Also, in Figure 5.4, a close up of the leading edge is presented to show the level of detail of the leading edge and the fillet made.

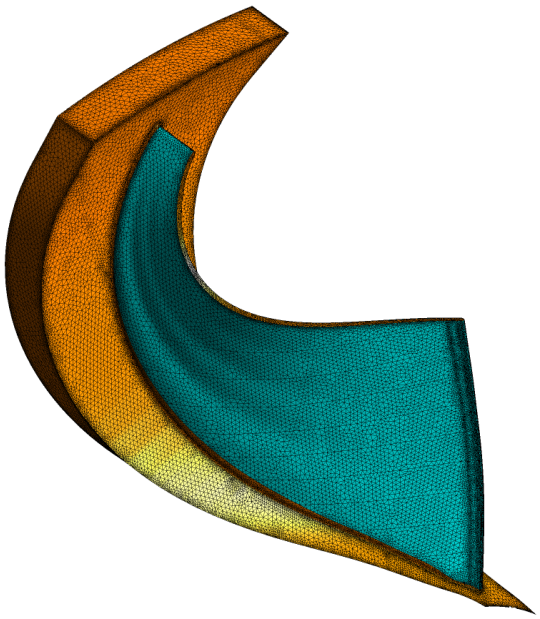

Figure 5.3: Unstructured mesh, generated in ICEM, of the mini-ORC rotor blade and hub cyclic sector.

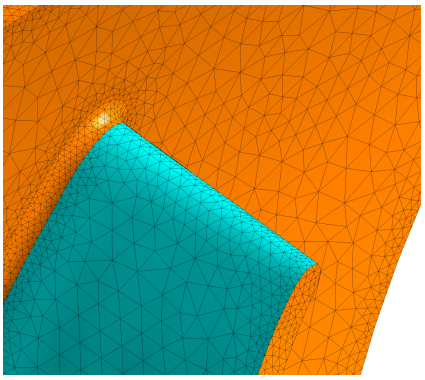

Figure 5.4: Leading edge close up of the mini-ORC mesh.

Table 5.3 presents the properties for the hub design parameters used. Titanium was once more used, for which material properties were presented in Table 4.7.

Hub angle	$18.947°$
Hub thickness	2×10^{-3} m
Hub fillet radius	0.4×10^{-3} m

Table 5.3: Hub design data for mini-ORC turbine.

The boundary conditions were applied as the rotational speed and the zero displacement constraint

imposed on the hub's bottom face. The simplified hub geometry is not ideal in terms of manufacturing since, just as before, the disk is being constrained in a way that only blade modes are captured. The conclusions regarding the transient unsteady pressures in terms of forcing and damping are not influenced by this, and so the results presented with this structural model are of relevance. An improved structural model was assembled and is presented at the end of this chapter to investigate the structural implications of a different model.

5.3. Campbell and interference diagram

Having the FEA model constructed, the Campbell diagram is assembled by conducting a pre-stressed modal analysis at three different rotational speeds, shown in Equations 5.1, 5.2 and 5.3. Just as before, Ω_{min} and Ω_{max} correspond, respectively, to 90% and 110% of the design speed Ω_{design},

$$\Omega_{\text{min}} = 0.9 \times \Omega_{\text{design}} = 88307.1 \text{ rpm} \tag{5.1}$$

$$\Omega_{\text{design}} = 98119 \text{ rpm} \tag{5.2}$$

$$\Omega_{\text{max}} = 1.1 \times \Omega_{\text{design}} = 107930.9 \text{ rpm} \tag{5.3}$$

With 40 engine orders and the first 5 modes plotted, the Campbell diagram is presented in Figure 5.5. The engine orders of 12, 24 and 36 are highlighted since they correspond to the excitations coming from the 1^{st}, 2^{nd} and 3^{rd} harmonics of the 12 upstream stators

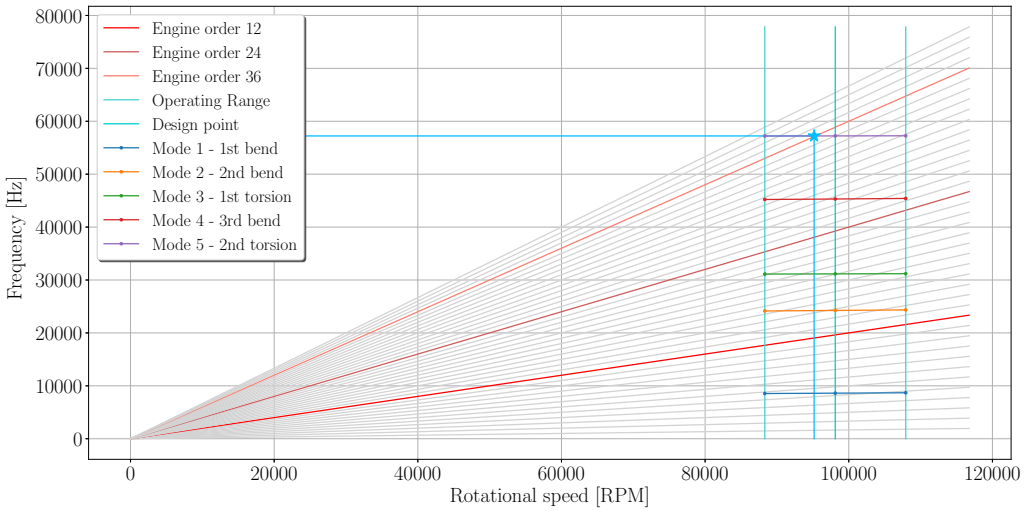

Figure 5.5: Mini-ORC turbine - Campbell diagram for blade modes with first 5 modes and 40 engine orders. Blue star indicates resonant crossing.

It is seen that, for the structural model elaborated, the first 2 harmonics of the unsteady pressures produced by the stators, corresponding to the engine orders 12 and 24, do not cross any modal fre-

quencies inside the operating range defined for the turbine. In this way, the resonant crossing studied will be related to the 36^{th} engine order and the 5^{th} vibration mode, occurring very close to the turbine's design speed. The mode shape associated with the mode in question is here shown in Figure 5.6 and is characterized by 2 torsion nodal lines. In Table 5.4 the resonant crossing data is summarized.

ORC resonant crossing	
Engine order	36
Ω_{RC}	95325 rpm
ω_{RC}	57233.23 Hz
Mode shape	2^{nd} torsion
Nodal diameter	2
IBPA	37.895°

Table 5.4: Resonant crossing details for mini-ORC turbine.

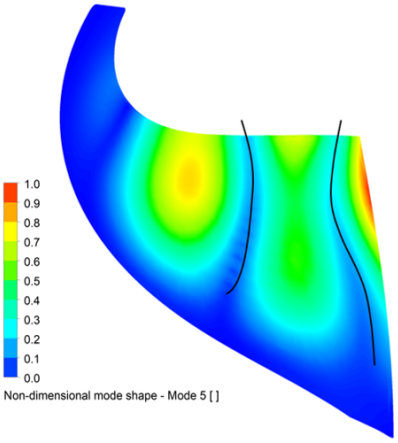

Figure 5.6: Mini-ORC normalized mode shape 5, interpolated onto CFD mesh. Nodal lines illustrated in black.

The interference diagram is computed at the resonant crossing speed. With this, the travelling wave mode can be captured and the IBPA determined. This diagram is shown in Figure 5.7.

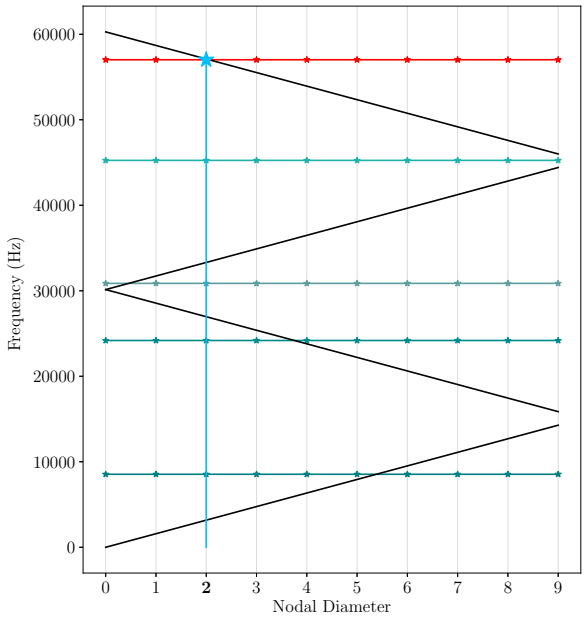

Figure 5.7: Mini-ORC turbine interference diagram at 97% of the design speed. Blue star representing resonant crossing. Natural frequencies of mode 5 represent in red.

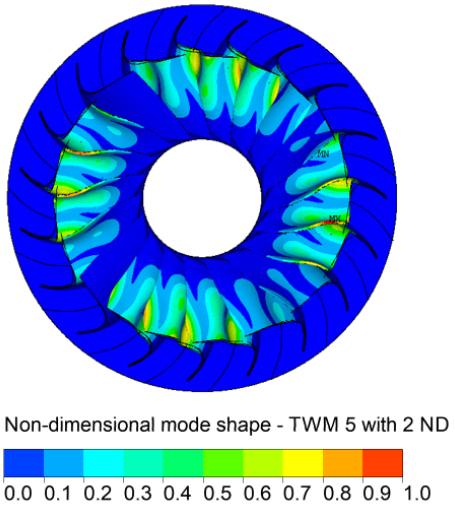

Figure 5.8: Mini-ORC turbine normalized travelling wave mode shape of blade mode 5 with 2 ND.

From the inspection of the diagram in Figure 5.7, indicated by a blue star, the resonant crossing of mode 5 (red line) happens at a nodal diameter of 2, corresponding to an interblade phase angle of $37.895°$, computed by,

$$IBPA_{\text{forward}} = \frac{360 \times ND}{N_{\text{blades}}} = 37.895°. \tag{5.4}$$

The diagram is assembled for 97% of the design speed and the positive interblade phase angle indicates that a forward travelling wave mode is seen.

In sum, mode 5, occurring at a frequency of 57233.23 Hz, will be excited by the 36^{th} engine orders which corresponds to the 3^{rd} harmonic of the transient excitation. The mode is characterized by a torsion shape with two nodal lines close to the trailing edge and is being excited at around 97% of the design speed. This crossing will excite the 2 nodal diameter travelling wave mode, which has an IBPA of $37.895°$.

5.4. Aeroforcing

The unsteady simulations to obtain the aerodynamic forcing were made by using the URANS solver of ANSYS CFX with a time inclination method to handle the non-equal pitch ratio. For this, a model containing 1 stator passage along with 2 rotor passages was assembled, yielding a pitch ratio of 0.8 which is inside the advised limits of CFX for the use of the time inclination method. Furthermore, 80 timesteps per period were defined, which resulted on a timestep of roughly 6.369×10^{-7} seconds and around $0.38°$ of rotation per timestep. Also, of course, the mixing plane interface was replaced by a transient stator-rotor interface.

To have an idea regarding important flow features of the flow in this turbine, Figures 5.9 and 5.10 show pressure contours on the rotor blade surface obtained with the steady state simulations for the pressure and suction side.

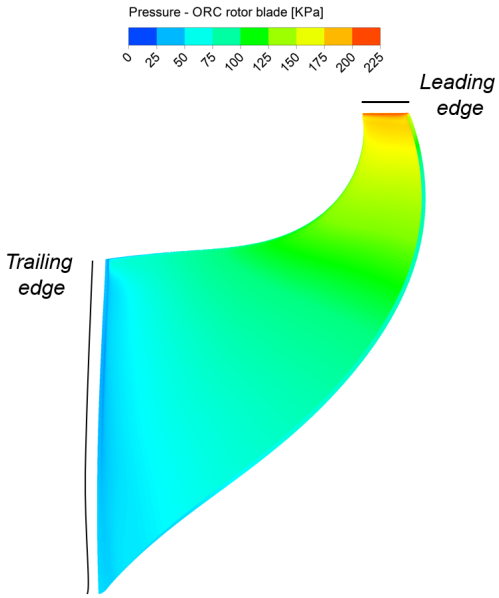

Figure 5.9: Mini-ORC turbine static pressure contour on the rotor blade surface on the pressure side

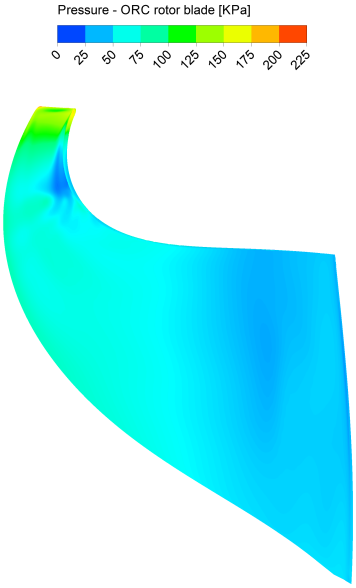

Figure 5.10: Mini-ORC turbine static pressure contour on the rotor blade surface on the suction side

An overall very uniform flow all over the blade surface is seen, with special emphasis on the pressure side. On the suction side, close to the leading edge, and spanning from approximately the midspan to the blade tip, a pressure drop area is verified. The reason for this area is the strong tip leakage that is occurring on this area of the blade. Indeed, this zone relates to the highest pressure area on the pressure side of the blade, where the flow from the upstream stator is impinging and thus generating the mentioned tip leakage.

The contours of harmonic pressures are shown here in Figures 5.11 and 5.12 for the pressure and suction side, respectively, of the rotor blade.

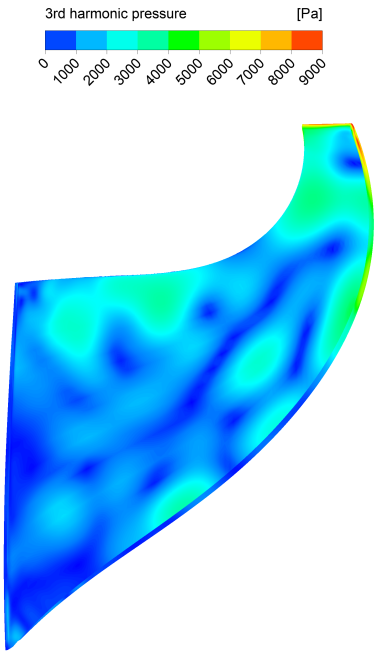

Figure 5.11: Mini-ORC turbine 3^{rd} harmonic pressure contour on the rotor blade surface on the suction side.

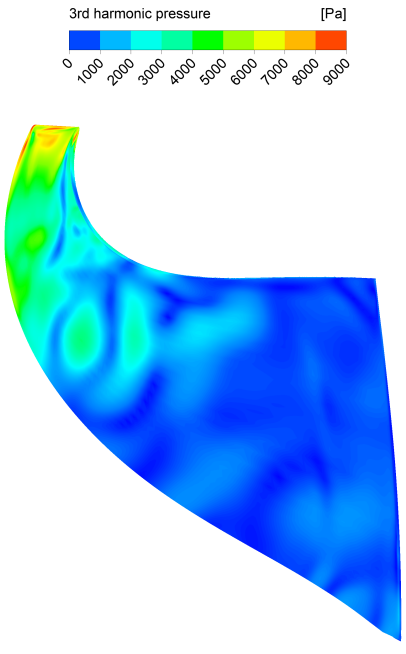

Figure 5.12: Mini-ORC turbine 3^{rd} harmonic pressure contour on the rotor blade surface on the suction side.

Unsteady pressures span all along the pressure side of the blade in different regions. The uniformity of the mean flow in this region leads to believe that this unsteadiness is coming from the impingement of the upstream wake and shock waves coming from the stator on the blade surface. Furthermore, high unsteady pressures are seen on the suction side, close to the leading edge, due to a combined effect between the upstream disturbances and the tip leakage in this region, reaching a maximum of around 9 kPa.

The following step is to project the harmonic pressures onto the mode shape direction using Equation 3.11. Figures 5.13 and 5.14 show the contours of the non-dimensional generalized pressure in relation to mode 5. The greatest match between modal displacements and unsteady pressures is occurring on the pressure side of the blade surface, around mid chord and close to the tip. Moreover, a mismatch between the locations of high unsteady pressures and high modal displacements is seen. Indeed, the high unsteady pressures coming from the upstream disturbances are located close to the leading edge, where small modal displacements are seen due to the small blade span when comparing to the trailing edge span.

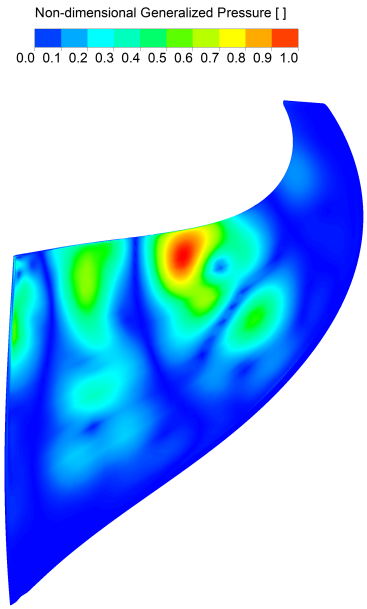

Figure 5.13: Mini-ORC turbine generalized pressure contour on the rotor blade surface on the suction side.

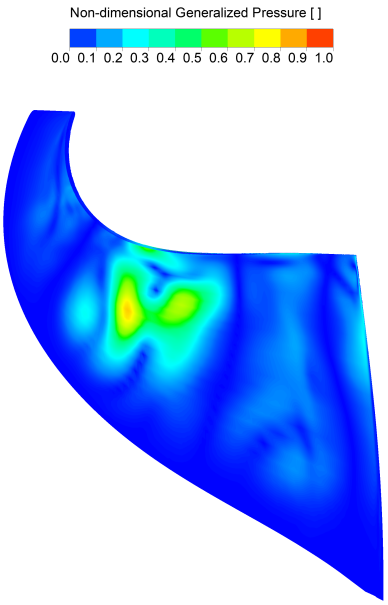

Figure 5.14: Mini-ORC turbine generalized pressure contour on the rotor blade surface on the suction side.

5.5. Aerodamping

The unsteady simulations to determine aerodynamic damping were made using 7 passages having the middle blade vibrating with the mode shape and frequency from the identified resonant crossing. 80 timesteps per period were defined, yielding to a timestep of 2.184×10^{-7} seconds. 7 blades in the computational domain are sufficient to obtain little unsteady effects from the middle vibrating blade, and so periodic boundary conditions were applied.

Applying the aerodynamic influence method to determine the aerodamping values for the ORC machine results in the stability curve presented in Figure 5.15. The damping values computed show a stable system for all the possible IBPA values.

The least stable mode is verified to be the one associated with an IBPA of $-113°$. Furthermore, the mode of concern, related to the IBPA of $37.895°$, is one of the most stables modes and has an aerodynamic damping ratio of $\xi_{\text{aero}} = 0.0008193$.

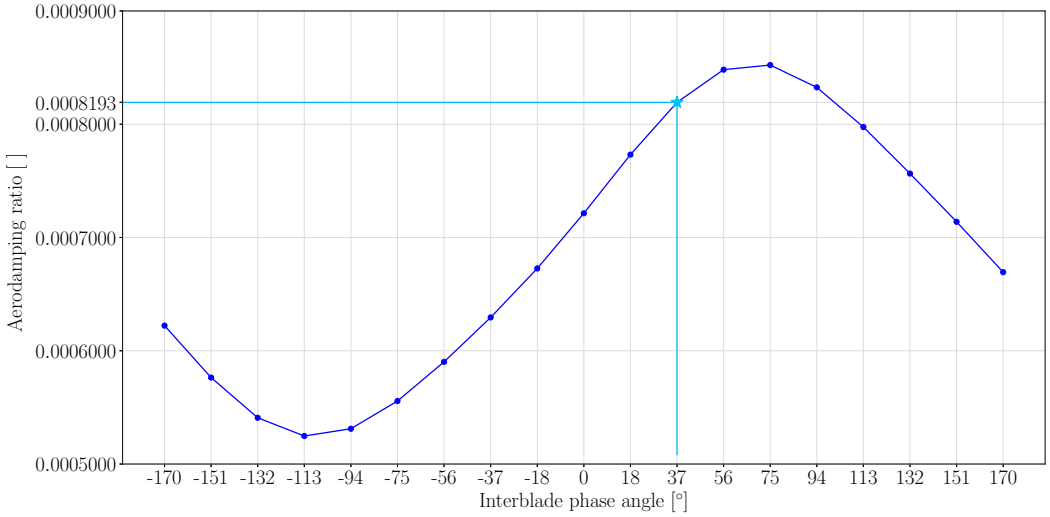

Figure 5.15: Mini-ORC turbine stability curve for mode 5. Aerodynamic damping ratio for all IBPA values.

One of the important steps when assembling the transient simulations for aerodamping determination is to correctly represent the uniform stage flow even when taking the stator presence off of the computational model. This is done so that the transient pressures obtained are only occurring due to the vibration of the blade and not due to the stator presence. To perform this, the boundary conditions are taken from the stage simulation, from the interface between the stator and the rotor. The flow direction, total pressure and total temperature, which are steady values, are imposed as boundary conditions for the rotor. Due to the extension of the domain, these values must be slightly changed so that the flow is well represented, which can sometimes become a difficult process. For the test case presented this match was difficult to obtain, and so an uncertainty of 30% was introduced on the values of aerodynamic damping obtained.

The comparison between the stage and the rotor only simulations was made by looking at the blade loadings at different spans through the rotor blade. In Figure 5.16 the blade loading for a span of 50% is shown.

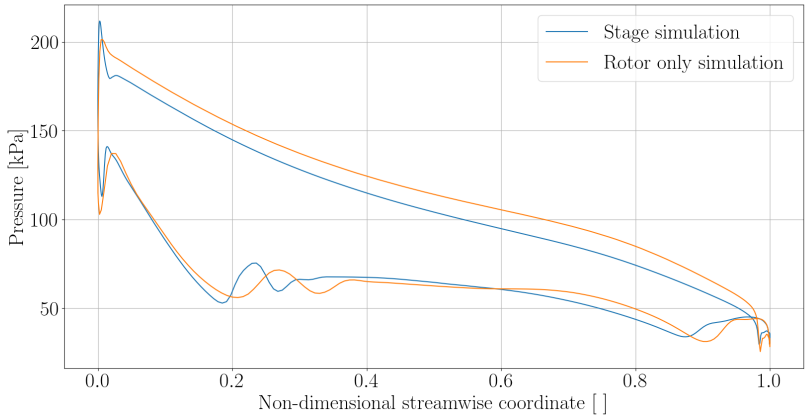

Figure 5.16: Comparison of blade loadings at 50% span for mini-ORC turbine stage and rotor only simulations.

It is seen that the overall pressure distribution follows similar patterns but at slightly different levels and positions throughout the rotor blade. The results presented show the best correlation obtained between both cases, and so the aerodynamic damping was computed based on the blade loading obtained from this isolated impeller simulation.

5.6. Forced response and life estimation

The generalized force and the aerodamping ratio values computed for the mini-ORC test case are presented in Equations 5.5 and 5.6. The generalized force is the summation, for the entire rotor blade, of the harmonic pressures (translated into forces) and projected onto the mode shape of interested. Also the aerodynamic damping value is associated with the vibration mode shape of interest.

$$\check{F}_{\text{gen}} = -0.0937 + 5.6158i \tag{5.5}$$

$$\xi_{\text{aero,37}} = 0.0008193 \tag{5.6}$$

The modal frequency, ω_{mode5}, which is equal to the excitation frequency, ω_{exc}, was used for the forced response analysis,

$$\omega_{\text{mode5}} = \omega_{\text{exc}} = 57233.23 \text{ Hz}. \tag{5.7}$$

Having this, the necessary components to construct the Haigh diagram by using the modal superpostion method are met.

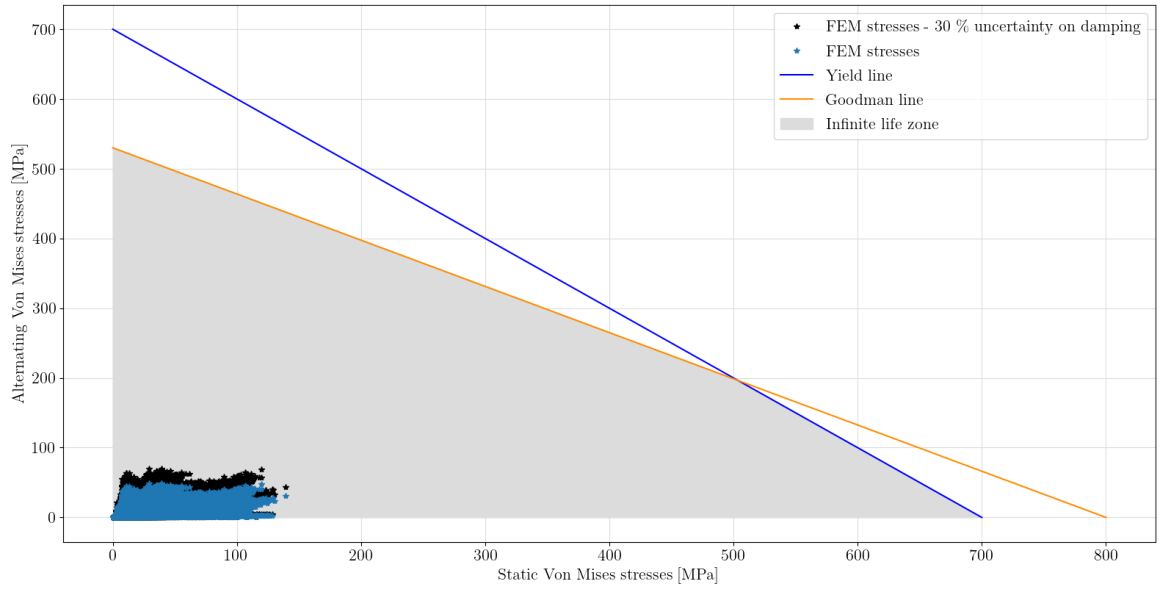

Figure 5.17: Haigh diagram for mini-ORC turbine. Excitation of blade mode 5 with 2 nodal diameters with 36 engine orders.

The Haigh diagram is presented in Figure 5.17, which shows that the stresses computed are within the structural limits imposed for an infinite life. Moreover, it is also important to mention that the static stresses for this case are smaller than the ones obtained for the previous test case, having a maximum of around 150 MPa. The small dimensions of the turbine, and its small mass, lead to small centrifugal stresses. This is an important observation since the margin for allowed alternating stresses will be high, and so results in high safety margins. In Figures 5.18 and 5.19 the static and modal stresses are presented. As expected, a static stress concentration on the fillet is seen, with higher intensity closer to the trailing edge. Regarding modal stresses, the areas of high blade twist present the higher stress values, reaching maximum values of around 75 MPa. Also a zone of high modal stresses close at the fillet is seen, fortunately, around midchord, and so mismatching with the higher static stresses locations.

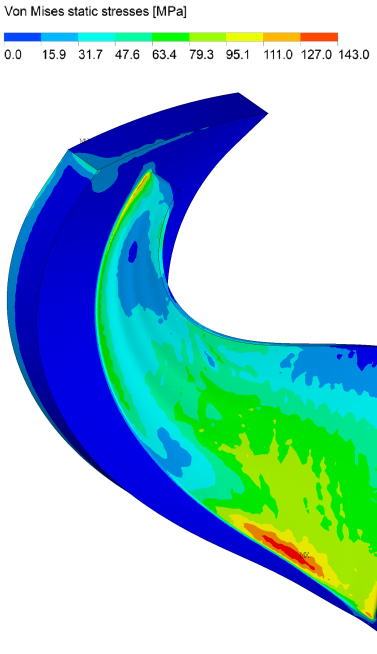

Figure 5.18: Static stresses on the mini-ORC turbine rotor model due to centrifugal forces.

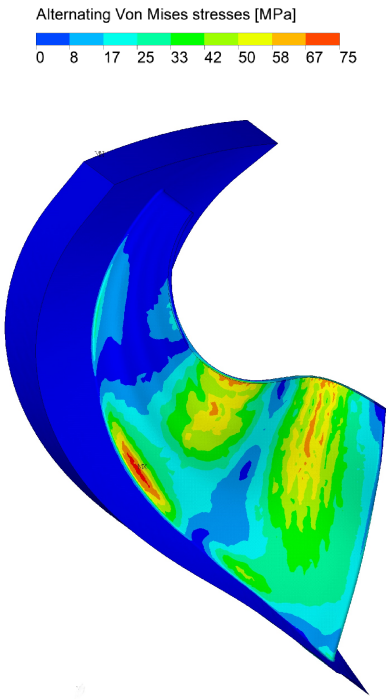

Figure 5.19: Alternating stresses on the mini-ORC turbine rotor model due to the vibration with mode shape of resonant crossing.

After this, the rotational speed and the generalized force values that would exceed the structural limits are computed to provide a safety factor regarding allowable static and alternating stresses. To do this, static structural simulations with increasing rotational speed were performed. Moreover, alternating stresses are computed with increasing values of the generalized force. It must be mentioned that the variations in the parameters mentioned does not constitute a forced response analysis but serves only to give an idea of how safe the operation of the machine is regarding the structural limits. Indeed, the increase in rotational speed would result in completely different vibration modes and flow features.

Having this, the Haigh diagrams of these computations are presented in Figures 5.20 and 5.21. It is seen that regarding static stresses, the rotational speed would have to be increased by a factor of around 2.5 to surpass any structural limits.

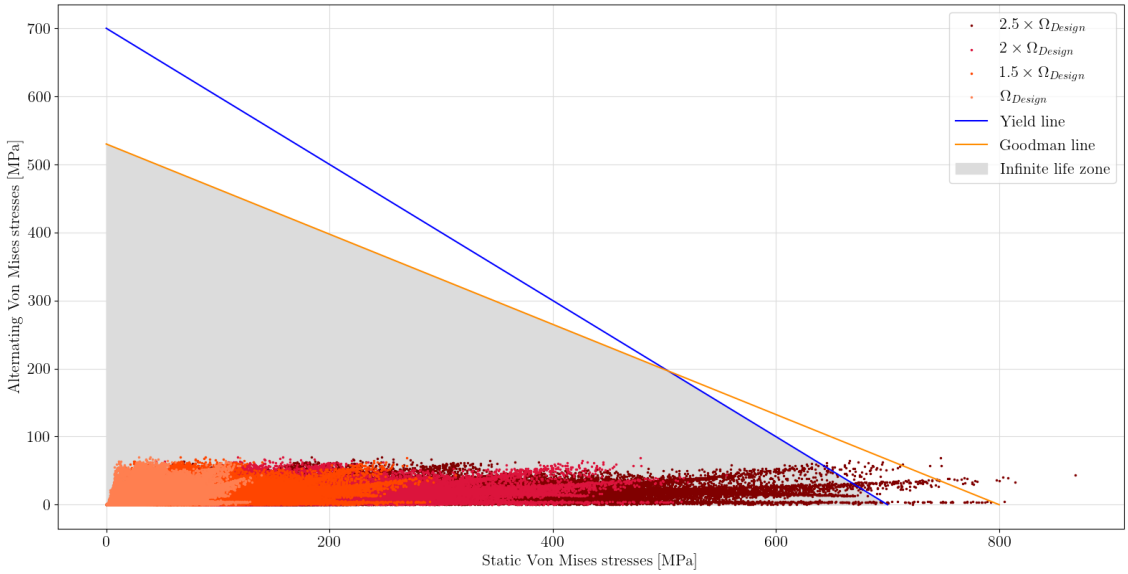

Figure 5.20: Haigh diagram for mini-ORC turbine. Excitation of blade mode 5 with 2 nodal diameters with 36 engine orders - Increasing rotational speed.

Furthermore, regarding the alternating stresses, the generalized force would have to be increased by a factor of around 10 before any limits are surpassed. This means that the overall unsteady pressures would also have to be 10 times higher than the current computed value. As an idea, comparing the maximum value of the first and third harmonic of the unsteady pressures computed, the first harmonic is around 2 times higher than the third harmonic.

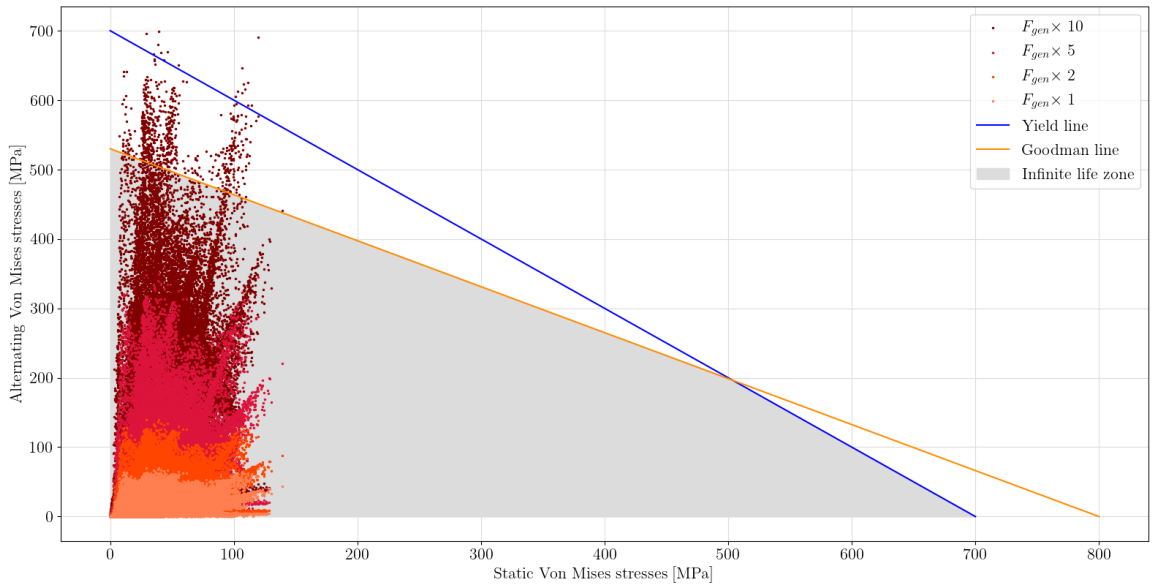

Figure 5.21: Haigh diagram for mini-ORC turbine. Excitation of blade mode 5 with 2 nodal diameters with 36 engine orders. - Increasing generalized pressures.

5.7. Structural model improvements

The previously presented structural model allowed for the FEA simulations to be performed with cyclic symmetry conditions but the simple hub design did not represent the closest model to be manufactured and was constrained in such a way that only blade modes were being captured. In this sense, the forced response analysis was repeated using a second structural model of the mini-ORC turbine which represents more closely a realistic blisk. A different hub geometry was constructed to study its influence on the modal frequencies and on the possible appearance of lower frequency resonant crossings. This geometry is presented in Figure 5.22 where the cyclic sector is reproduced to represent the entire turbine. The cyclic sector itself, already meshed, is shown in Figure 5.23.

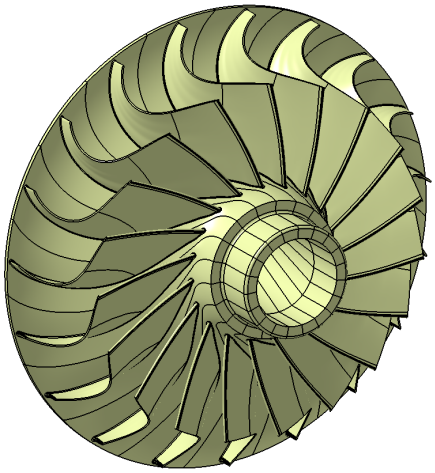

Figure 5.22: Mini-ORC bladed disk assembly geometry in CATIA. Reproduction of cyclic sector geometry over entire wheel.

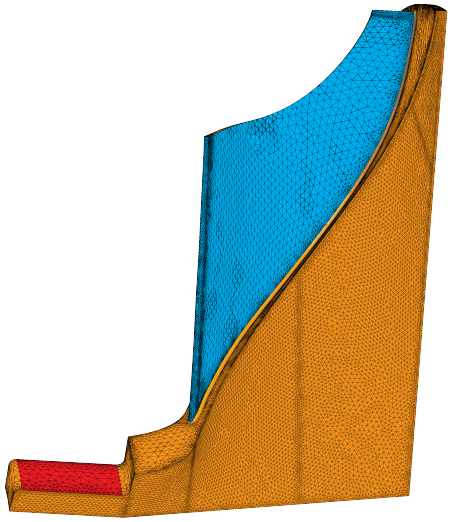

Figure 5.23: Mini-ORC turbine cyclic sector model. Unstructured mesh generated in ICEM.

A different material was also used for this model, INCONEL 625, a nickel-based alloy, for which structural properties are defined in Table 5.5. This material is chosen since it is usually used in industry in the manufacturing process of turbines. Having a more accurate structural model will also allow to impose the zero displacement boundary condition directly on the turbine shaft, represented in red in Figure 5.23, which is a situation that will be closer to the real case.

INCONEL 625	
Young modulus - E	207.5×10^9 Pa
Poisson coefficient - ν	0.278
Density - ρ	8440 kg m^{-3}

Table 5.5: Material properties for INCONEL 625 [46].

A study regarding the influence of the material in the modal frequencies was made to know if the changes in the resonance diagrams should be attributed to the geometry change or to the new material. It was concluded that the material does not have a major influence on the mode frequencies. The ratio between stiffness and density is roughly maintained between titanium and INCONEL 625, and so it can be expected that vibration mode frequencies remain similar. The interference diagrams for the design speed and for the minimum operating range speed are presented in Figure 5.24. It is seen that the frequency change between different nodal diameters indicates that these are mainly disk dominated modes. This comes due to the application of the zero displacement boundary condition on the shaft region mentioned previously, which does not constrain the disk.

The Campbell diagram is not presented since, being disk dominated modes, the blade modal frequencies do not correctly represent the real case. In this way, the assembly of the interference diagram was made at minimum and maximum speed of the operating range, and at the design speed.

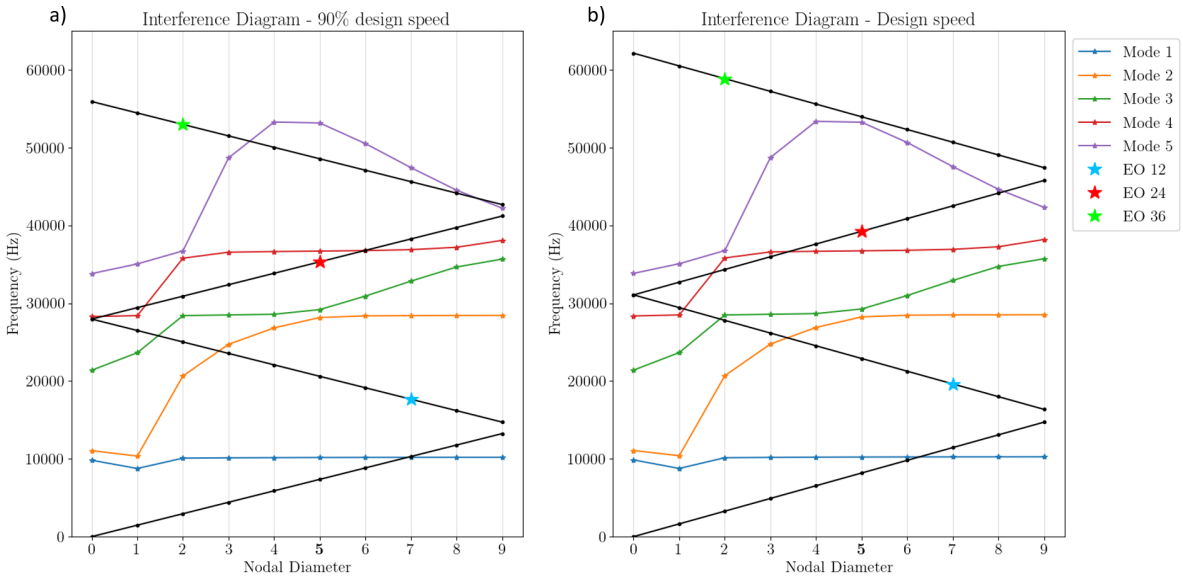

Figure 5.24: Mini-ORC turbine interference diagrams for a) minimum operating range speed and b) design speed. Resonant crossing concerning engine order 24 and mode 4 with 5 nodal diameters is below natural frequency for case a) and above natural frequency for case b). Hence, resonant conditions for this case will be found between minimum and design speeds.

To identify resonant conditions, the engine orders 12, 24 and 36 are inspected since they will be associated with the 12 stators placed upstream of the impeller. The 12^{th} engine order (represented in Figure 5.24 by the blue star) could possibly lead to the lowest frequency crossings but, fortunately, the excitation frequency is located between modal frequencies of modes 1 and 2, both at 90% and at 100% of the design speed (as seen in Figure 5.24). The excitation frequency associated with the 24^{th} engine order (represented in Figure 5.24 by the red star) is located right below the frequency of mode 4 at 90% of the design speed, and just above it at 100% of the design speed. Having this, it is concluded that the lowest frequency resonant crossing possible corresponds to engine order 24 with mode 4 between minimum speed and the design speed. By constructing interference diagrams at different rotational speeds it was found that the resonant crossing mentioned occurs at around 93%

of the operating speed. Furthermore, nodal diameter 5, which corresponds to an IBPA of $94.737°$ will be excited. In Figure 5.25 the vibration mode is illustrated, and the torsion nodal line is depicted. The information regarding the resonant crossing is summarized in Table 5.6.

ORC resonant crossing	
Engine order	24
$\boldsymbol{\Omega}_{\text{RC}}$	91250.67 rpm
$\boldsymbol{\omega}_{\text{RC}}$	36500.268 Hz
Mode shape	1^{st} torsion
Nodal diameter	5
IBPA	$94.737°$

Table 5.6: Mini-ORC turbine resonant crossing for improved structural model.

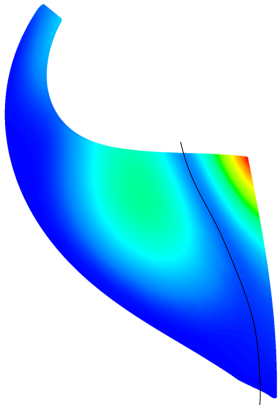

Figure 5.25: Mini-ORC mode 4 shape on CFD mesh for improved structural model. Nodal line illustrated in black.

After having the resonant crossing defined, determining the aerodynamic forcing and damping was necessary. Transient simulations for aerodynamic forcing were not necessary to conduct again since the previous simulations provided all the necessary information. In terms of aerodynamic damping, the transient simulations were performed by using a Fourier transformation method, with only two passages. The mode shape was imposed to each blade and the nodal diameter was defined in CFX to account for the resonant crossing's IBPA. This method is an alternative to the aerodynamic influence coefficient method where a smaller number of passages is simulated, but where the aerodynamic damping value is only computed for one IBPA rather then for its entire range. Furthermore, 76 timesteps per period were used, resulting in a timestep of 3.604×10^{-7} seconds.

The Haigh diagram can then be computed and is presented in Figure 5.26.

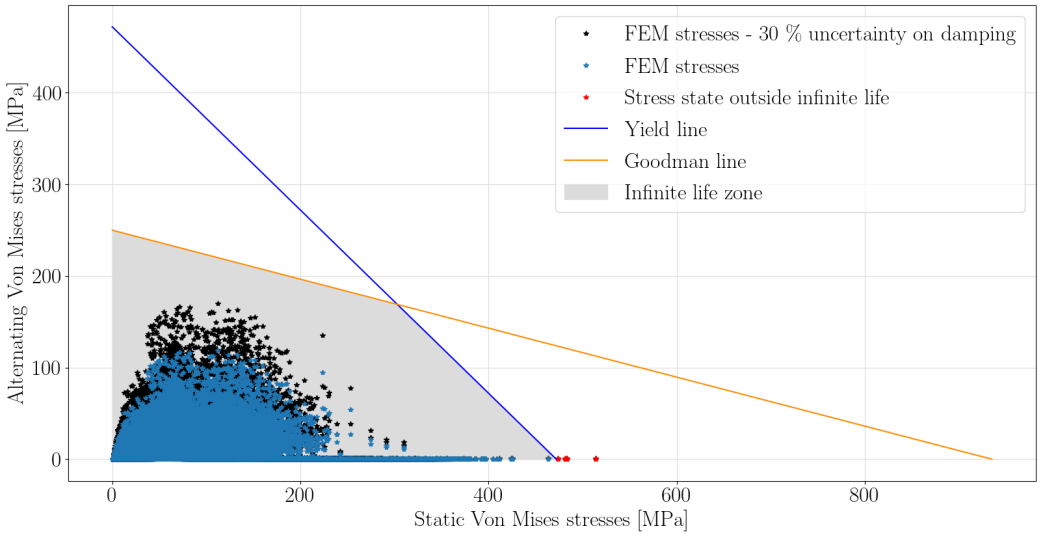

Figure 5.26: Haigh diagram for mini-ORC turbine with improved structural model. Excitation of blade mode 4 with 5 nodal diameters and 24 engine orders.

The stress values that do not fall inside the infinite life region are illustrated in red in Figure 5.26. These points correspond to a concentration of static stresses on a cusp in the hub. The remaining static and alternating stresses, which are located in the blade and fillet, are still within the structural limits for infinite life of INCONEL 625 summarized here in Table 5.7. Even when introducing a 30% uncertainty on the aerodynamic damping values, the mentioned stresses are within limits.

INCONEL 625	
Yield strength	472 MPa
Ultimate strength	935 MPa
Endurance limit	250 MPa

Table 5.7: INCONEL 625 structural limits [47].

Comparing with the Haigh diagram for the previous structural model (for the stresses on the blade and fillet), the safety margins are greatly reduced. This comes firstly due to higher alternating stresses, which are related to the fact that a lower frequency mode is being excited by a lower engine order. Besides this, high static stresses are assessed, which come at a location in the hub where no alternating stresses are verified, seen in Figure 5.27 delineated by the black lines, and where a concentration of static stresses would be expected. Furthermore, the structural limits regarding fatigue, for INCONEL 625, are much lower than Titanium and contribute also for the smaller safety margins. The mentioned stress concentration will disappear when further improving the structural model by including the turbine shaft and designing an appropriate fillet in the mentioned location.

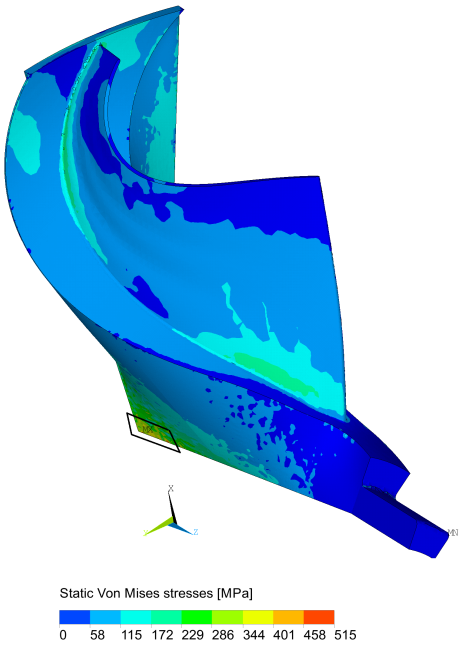

Figure 5.27: Static stresses on the mini-ORC turbine rotor with improved structural model due to the centrifugal forces.

5.8. Conclusions

Having presented all the relevant results for the ORC turbine test case, some conclusions can now be made.

Regarding the first structural model assembled, using a simple hub design and titanium as the material, no structural limits regarding high cycle fatigue were surpassed. The causes for the safe design seen are:

- The static stresses obtained due to the centrifugal effects are small due to the small dimensions of the turbine, and so result in higher allowable margins for alternating stresses.

  A linear study of the rotational speed influence on the static stresses showed that for the structural limits to be exceeded this parameter would have to increase by a factor of 2.5.

- The Campbell diagram does not show any resonant crossings for the first 4 modes inside the operating range defined. The studied resonant conditions, regarding the excitation of the 5^{th} natural mode with the 36^{th} engine order (corresponding to the 3^{rd} harmonic from the 12 upstream stators) are characterized by a high frequency mode and high harmonic, fact that usually does not result in large forced response vibration issues, and that was verified by the analysis made.

- A natural mismatch between the location of higher unsteady pressures due to the stator presence and the vibration mode shape was verified. This will result in low generalized forces, and so in low stresses and vibration amplitudes.

  Just as before, a linear study of the generalized force magnitude was made, which showed

that for the structural limits to be surpassed, this parameter would have to be increased by a factor of 10.

- It was verified that a stable system is encountered for all the values of interblade phase angles possible, leading to positive damping values from an aerodynamic origin.

  The uniform flow at which these values were determined was not exactly equal to the stage flow and an uncertainty of 30% was introduced in the damping values.

After this analysis, an improved structural model was developed by designing a new hub, which represents more closely the actual turbine to be manufactured, and by using INCONEL 625 as the material, which is a material usually used in industry in the manufacturing process of turbines. From this analysis, the conclusions taken are:

- The influence of the disk on the natural modes is not negligible and resulted in varying modal frequencies with respect to the nodal diameters on the interference diagram. The use of this diagram, at different rotational speeds, is advised to inspect resonance conditions;
- The resonant conditions identified, which concerned the excitation of the 4^{th} natural mode with the 24^{th} engine order (corresponding to the 2^{nd} harmonic from the 12 upstream stators), are characterized by lower frequency and engine order regarding the previous structural model;
- The mismatch between the location of higher unsteady pressures due to the stator presence and the vibration mode shape was still verified but the lower harmonic leads to higher unsteadiness, and so to a high value of the generalized force;
- The vibration mode studied was stable regarding self-excited oscillations;
- No structural limits were surpassed for stresses in the blade region:

  A cusp on the model led to high static stresses at the hub (where no alternating stresses were seen). This stress concentration will disappear when including a fillet and the shaft in the structural model;

  The safety margins were reduced due to the higher alternating stresses (due to the higher generalized force), and to the smaller structural limits of the new material used.

Although the conclusions presented lead to no structural issues regarding high cycle fatigue for the mini-ORC turbine, further studies should be conducted. In this way, as a recommendation for the manufacturer of this machine, a detailed investigation with precise material properties and hub geometry should be made to investigate if any resonant crossings might occur at lower frequency modes and harmonics. Moreover, also an investigation regarding the upstream inlet geometry of the stators, such as a scroll volute, is recommended since an asymmetric inlet will result in low engine order excitations that will surely affect lower frequency modes such as the 1^{st} bending mode.

6

Conclusions and recommendations

In this chapter, the conclusions taken throughout this study are given in Section 6.1. Besides this, the research questions initially stated are answered based on the results obtained. In Section 6.2 recommendations for future work are given regarding the study of forced response behaviour of small scale organic Rankine cycle (ORC) turbines and the implementation of the knowledge gathered in optimization procedures.

The objective of this work was to develop a forced response analysis chain and apply it to an ORC turbine test case. The motivation for this was based in the fact that the unsteadiness observed in these machines would raise concerns regarding the structural integrity in terms of high cycle fatigue. Furthermore, an analysis of the influence of organic fluids on the aeroelastic behaviour of this class of machines has not been performed in the past, and so a study of these effects would enhance the life and economic viability of organic Rankine cycle machines.

6.1. Conclusions

In summary, this work regarded the assessment of dynamic aeroelastic effects on small scale, highly supersonic turbines operating with the organic Rankine cycle. To assemble the necessary forced response analysis methodology, a preliminary framework was developed and validated using a well documented test case commonly known as NASA rotor 67 [43]. Subsequently, a small-scale organic Rankine cycle machine, known as ORCHID (developed at TU Delft) [3] was analysed in the developed framework. Furthermore, a study regarding different transformation methods for transient computational fluid dynamics simulations in turbomachinery was made during the research exchange undergone at the Institute of Thermal Turbomachinery and Machinery Laboratory (ITSM) in the University of

Stuttgart.

Two of the most commonly occurring dynamic aeroelastic effects are flutter and forced response. Flutter is a case of self-excited oscillations determined by the energy transfer between fluid and structure due to unsteady aerodynamic forces created by blade vibrations. On the other hand, forced response deals with the structural response to a harmonic aerodynamic forcing induced by periodic flow non-uniformities generated by upstream and downstream components. The influence of these effects is studied regarding high cycle fatigue, which indicates failure due to a high number of cycles occurring at small, elastic strains. Taking these effects into consideration, the developed methodology can be summarized in three steps. First, the assessment of resonant conditions. Second, determining aerodynamic damping (to account for the flutter phenomenon) and forcing (to account for the forced response phenomenon) by performing transient computational fluid dynamics simulations. And finally, the post process of results to obtain structural stresses that can be compared against material limits.

6.1.1. Case study 1: NASA rotor 67

A study of different transient methods that handle stator-rotor interactions (in ANSYS CFX) was made using the present test case. The different methods gave very similar results in terms of the generalized force for all the cases and showed agreeing contours of harmonic and generalized pressures, showing that these options provide a viable alternative for cases where a reduction of the computational domain cannot be obtained while maintaining a unity pitch ratio. As an example, for the ORCHID case, a reduction of computational size of around 10 times was obtained by the use of the time inclination method in CFX. Furthermore, the use of harmonic balance instead of a time-marching method was also made using the possible models. The combination of the Fourier transformation model and the harmonic balance method yielded convergency problems and ended up being abandoned. The use of a model mantaining a pitch ratio of 1 and the harmonic balance method provided viable results in a shorter computation time, also showing the potential of this method as a faster alternative to time-marching methods. **Since all the methods described (with the exception of the Fourier transformation using harmonic balance) provided coherent results, it can be concluded that the choice of transient method to use when computing aerodynamic forcing can be made solely by assessing the case that allows for the biggest reduction in computational size.**

The excitation of mode 4, at a frequency of 2656 Hz, by engine order 11 due to the upstream inlet guide vanes was identified as the resonant condition to study. The interblade phase angle for these conditions was identified to be of $180°$. Titanium was used for the structural model, in order to verify natural frequency values against available results in literature [36]. The highest unsteady pressures were seen to be in the order of 3 kPa which, with the positive aerodynamic damping values obtained, resulted in alternating stresses in the order of 33 MPa. Maximum static stresses due to centrifugal forces were computed to be around 600 MPa. The mentioned structural stresses for the resonant conditions described were inside the safety limits regarding high cycle fatigue.

In sum, the small values of unsteady pressures and the stable system for the interblade phase angle identified led to a structurally safe design. A mismatch between locations of high alternating and static stresses also contributed to this. Most importantly, the forced response analysis chain was successfully assembled with this test case and can now be applied to the ORCHID turbine.

6.1.2. Case study 2: Organic Rankine cycle turbine

For the ORCHID case, also referred to as mini-ORC turbine, two structural models were assembled. First, a simplified hub was designed to allow for cyclic symmetry analysis to be performed. Also, titanium was the material used, such as in the previous case. After this, an improved model of the mini-ORC turbine was assembled. The motivation for this was to study how a significantly different hub geometry, and material, could influence the resonance diagrams. In this way, a hub design closer to the one to be manufactured was made and INCONEL 625, a nickel based alloy usually used in turbine manufacture, was used instead of titanium.

Structural model 1

For this model, the resonant conditions identified are:

- Vibration mode: Blade mode 5 - Frequency of 57233.23 Hz;
- 2^{nd} nodal diameter blisk mode: Interblade phase angle of $37.895°$;
- Excitation force associated with the 3^{rd} harmonic of the 12 upstream stators, corresponding to engine order 36.

From the transient fluid simulations, the unsteady pressures of the 3^{rd} harmonic reach a maximum of 9 kPa, much higher than the previous test case and confirming the initial concerns regarding forced response issues due to high unsteadiness. With the positive aerodynamic damping values identified, maximum alternating stresses were around 75 MPa. The maximum static stresses obtained due to the centrifugal effects are around 150 MPa. These values are small due to the small dimensions of the turbine, and so result in higher allowable margins for alternating stresses. **The static and alternating stresses computed are inside structural limits regarding high cycle fatigue.**

Safety margins regarding the structural stresses were defined, and it was concluded that:

- In terms of static stresses, a linear study of the rotational speed showed that for the structural limits to be exceeded this parameter would have to increase by a factor of 2.5;
- In terms of alternating stresses, a linear study regarding the generalized force magnitude was made, that showed that, for structural limits to be surpassed, this parameter would have to be increased by a factor of 10.

These safety margins for this structural model are high and can be justified by different arguments:

- The Campbell diagram does not show any resonant crossing for the first 4 modes inside the operating range defined, and so the resonant conditions studied are characterized by a high frequency mode and high harmonic, fact that usually does not result in great structural issues;
- Regarding the excitation, a natural mismatch between the location of higher unsteady pressures due to the stator presence and the vibration mode shape was identified, which results in lower values of the generalized force, and so in lower stresses and vibration amplitudes;
- In terms of self-excited vibrations, it was seen that a stable system is encountered for all the values of interblade phase angles possible;

  As mentioned, the uniform flow at which these values were determined was not exactly equal to the stage flow and an uncertainty of 30% was introduced in the damping values which still resulted in high safety margins;
- The previously mentioned small static stresses contribute to structural safety since allowable margin for alternating stresses is higher.

Structural model 2

As could be expected, with this model, different resonance diagrams were obtained and a lower frequency resonant crossing was identified and studied. The influence of the disk on structural modes was found to be relevant, and so the interference diagram showed varying frequencies with respect to the nodal diameter. Furthermore, the influence of the material on the vibration modes was found to be minimal since the ratio of stiffness and density between both materials studied was roughly maintained.

The resonant conditions identified for this structural model are:

- Vibration mode: Blade mode 4 - Frequency of 36500.268 Hz;
- 5^{th} nodal diameter mode: Interblade phase angle of $94.737°$;
- Excitation force associated with the 2^{nd} harmonic of the 12 upstream stators, corresponding to engine order 24.

Regarding the structural response, the maximum static stresses were identified on a cusp of the structural model assembled which will not be present when the turbine shaft is included, and so these stresses are not considered physically meaningful. Regarding the blade region, the maximum static stresses are of around 300 MPa. In terms of alternating stresses, these are identified to have a maximum of around 150 MPa. **In this way, from inspection of the Haigh diagram, no structural limits for the blade region were surpassed, result that can be associated with a set of observations from the unsteady fluid simulations:**

- The harmonic pressures reached a maximum of 11.5 kPa, which is, as expected, higher than the 3^{rd} harmonic previously studied, but still not sufficient to excite vibrations to levels of concern;
- A mismatch between regions of high unsteadiness and modal displacements was still observed, just as in the previous model;

- In terms of self-excited oscillations, the transient simulations with vibrating mesh showed positive aerodynamic damping values.

Even though the structural integrity can still be confirmed regarding high cycle fatigue, when comparing the safety margins against the previous structural model, these are greatly reduced, to around 1.5. This reduction in terms of safety margins is explained due to:

- Higher alternating stresses, which were expected for lower frequency resonant conditions;
- An excitation force associated with a lower engine order, that is characteristic of higher unsteadiness;
- The smaller structural limits of INCONEL 625 in comparison with titanium.

6.1.3. Research questions

Stemming from the conclusions presented above, the research questions presented before can now be answered:

1. Which are the dominant aeroelastic issues in small-scale, highly supersonic machines operating with organic fluids?

   a) Regarding aerodynamic damping, a stable system for all interblade phase angles is observed.

   b) A high harmonic content in terms of pressure, due to the presence of the disturbances coming from the upstream stator, is verified. The shock wave system seen in the stator, the tip leakage verified in the rotor blade and the potential interaction between the two rows summarize the flow features identified that lead to excitation.

   c) The region of unsteadiness on the suction side of the rotor blade shows highest values on a region close to the leading edge, from the leading edge until around 30% of the chord, due to the interaction with the shock wave from the stator. The region of unsteadiness on the pressure side shows lower values than the suction side but more distributed around the blade. Due to the blade vibration, the unsteady region was, as expected, in the region of higher displacements, acting in such a way that energy is dissipated to the flow.

   The dominant aeroelastic issues in the machine studied lay in forced response phenomena, due to a positive aerodynamic damping and high excitation pressure values. The flow features summarized create the unsteadiness at the regions of the rotor blade mentioned and result in some extent of excitation that leads to alternating stresses that can be compared against material limits.

2. What can be concluded regarding the influence of the aeroelastic issues identified on the life of the machine being analysed?

a) A mismatch between regions of higher unsteadiness and of high modal displacements is observed. Although the unsteadiness is high in the machines studied, the mentioned mismatch results in small values of the generalized force, not exciting the vibration modes to levels of concern;

b) None of the structural limits are surpassed for the blade region. The study was performed with two different structural models with titanium and INCONEL 625. The model with INCONEL 625 resulted in smaller safety margins but still inside the allowable region (for the blade region). The safety factors for the titanium model due to static loads were determined to be around 2.5 and regarding alternating stresses around 10. The INCONEL 625 model had safety factors of around 1.5 for both static and alternating stresses on the blade region. Besides the answers to research questions 1.a) and 2.a), further reasons that resulted in stresses inside safety regions were the small dimensions of the machine, that even having high rotational speeds, resulted in small centrifugal stresses that raise the allowable margins for alternating stresses and the fact that excitations due to lower harmonics for the machine studied did not result in any resonant crossings inside the operating range.

c) Regarding the assumptions of the methodology assembled and the resonant crossings identified, the infinite life of the machine is predicted.

d) To increase safety margins regarding high cycle fatigue, the use of a material with a high endurance limit is advised. The incorporation of a structural analysis in the early stages of the design phase is advised to avoid low frequency resonant crossings inside the operating range.

Although a high amount of unsteadiness is seen, the excitation force verified does not lead to any stresses that surpass the structural limits, mainly due to the mentioned mismatch between unsteadiness and mode shape location. From the Haigh diagram, for the resonant conditions studied, an infinite life behaviour of the machine is predicted, also due to the small static stresses that raise the allowable margins for alternating stresses.

The dominant aeroelastic issues identified in the mini-ORC turbine are more related to aerodynamic forcing than to flutter, which, at the resonant conditions found, didn't raise concerns regarding the life of the machine in terms of high cycle fatigue. In the best case scenario it was seen that the turbine can withstand an harmonic forcing with similar shape around 10 times higher. Although this is a satisfying result, it is only valid for the machine configuration elaborated and with the assumptions established, and so recommendations for future work, related to these points, are presented in the following section.

In conclusion, a forced response analysis chain based on one-way fluid-structure interaction simulations was successfully assembled and applied to two majorly different test cases. The use of the commercial software ANSYS CFX and ANSYS APDL allowed for all the computations to be performed and the post processing was made in Python. Moreover, the methodology can be generalized to different software with the correct adaptation of the post processing scripts, and so can also be included

in optimization procedures. For the mini-ORC turbine it was concluded that the inherent unsteadiness of this machine that leads to the excitation of natural modes does not raise concerns regarding the structural integrity of the machine.

6.2. Recommendations for future work

The first recommendations presented are related to the manufacture of the mini-ORC turbine, since further investigation regarding the possible appearance of lower frequency resonant crossings is of relevance. The occurrence of these resonant crossings can raise higher concerns regarding forced response issues. Furthermore, recommendations from a more academic point of view are also presented, related to the improvement of computational fluid dynamics simulations and to the incorporation of the work presented on multi-disciplinary optimization procedures.

- **Further analysis with precise material properties and hub geometry.** This was already performed in the thesis presented but it can be iteratively improved having further information from the manufacturing process. Namely, the hub thickness can be varied, the turbine shaft included in the structural model and a cost against safety analysis made with materials as titanium, INCONEL 625 and aluminium;

- **Analysis using upstream inlet geometry, such as a scroll volute.** It is likely that the inlet before the stator will not be perfectly symmetric. In this case, low engine order excitations will be unavoidable and will result in resonant crossings with lower frequencies modes, such as the 1^{st} bending mode;

- **Investigate the influence of static centrifugal and gas loads on hot and cold geometries.** If significant differences are found, either in natural frequencies or stress levels, an analysis using a cold geometry instead of hot should be performed;

- **Automation of Campbell and interference diagram computation.** The possibility of assembling a Python script that runs ANSYS APDL in batch and generates Campbell and interference diagrams is very feasible. A more challenging goal would lie in an automatic mesh generation script that could account for geometry modifications in a simple way. Such a tool would allow for quick structural analysis to be performed in the early stages of the design process in order to avoid the appearance of low frequency resonant crossings.

- **Investigate the match between stage and rotor only simulations for aerodynamic damping.** Either for the NASA R67 or for the mini-ORC test case, a closer match between stage and rotor only simulations could be obtained. Optimizing this procedure and studying the influence of the correct uniform flow representation on the aerodynamic damping value can result in a much easier setup of transient fluid simulations for this case.

- **Investigate the influence of the blade vibrations determined on the efficiency of the machine.** The major step forward after this thesis lies in its incorporation in multi-disciplinary optimizations. Optimizations using only aerodynamic improvements as objective functions can result in higher blade vibrations which can lead to structural issues. Quantities such as the generalized force and aerodynamic damping can be used as objective functions and its sensitivity in relation to different design parameters can be studied. Such tools can be deemed as very relevant to increase the safety of a wide range of turbomachinery components used in industry and to shorten the necessary design and testing chain before its market incorporation.

Bibliography

[1] AV Srinivasan. Flutter and resonant vibration characteristics of engine blades: An igti scholar paper. In *ASME 1997 International Gas Turbine and Aeroengine Congress and Exhibition*. American Society of Mechanical Engineers Digital Collection, 1997.

[2] AR Collar. The expanding domain of aeroelasticity. *The Aeronautical Journal*, 50(428):613–636, 1946.

[3] Carlo Maria De Servi, Matteo Burigana, Matteo Pini, and Piero Colonna. Design method and performance prediction for radial-inflow turbines of high-temperature mini-organic rankine cycle power systems. *Journal of Engineering for Gas Turbines and Power*, 2019.

[4] Fredy Vélez, José J Segovia, M Carmen Martín, Gregorio Antolín, Farid Chejne, and Ana Quijano. A technical, economical and market review of organic rankine cycles for the conversion of low-grade heat for power generation. *Renewable and Sustainable Energy Reviews*, 16(6):4175–4189, 2012.

[5] Piero Colonna, Emiliano Casati, Carsten Trapp, Tiemo Mathijssen, Jaakko Larjola, Teemu Turunen-Saaresti, and Antti Uusitalo. Organic rankine cycle power systems: from the concept to current technology, applications, and an outlook to the future. *Journal of Engineering for Gas Turbines and Power*, 137(10):100801, 2015.

[6] Sylvain Quoilin, Martijn Van Den Broek, Sébastien Declaye, Pierre Dewallef, and Vincent Lemort. Techno-economic survey of organic rankine cycle (orc) systems. *Renewable and Sustainable Energy Reviews*, 22:168–186, 2013.

[7] Damian M Vogt. Experimental research on aeroelasticity. *Structural Design of Aircraft Engines: Key Objectives and Techniques*, 2008.

[8] Mayuresh J Patil, Dewey H Hodges, and Carlos ES Cesnik. Limit-cycle oscillations in high-aspect-ratio wings. *Journal of fluids and structures*, 15(1):107–132, 2001.

[9] Jean Thomassin, Huu Duc Vo, and Njuki W Mureithi. Blade tip clearance flow and compressor nsv: The jet core feedback theory as the coupling mechanism. In *ASME Turbo Expo 2007: Power for Land, Sea, and Air*, pages 619–628. American Society of Mechanical Engineers, 2007.

[10] JG Marshall and M Imregun. A review of aeroelasticity methods with emphasis on turbomachinery applications. *Journal of fluids and structures*, 10(3):237–267, 1996.

[11] Damian Vogt. *Experimental investigation of three-dimensional mechanisms in low-pressure turbine flutter*. PhD thesis, 2005.

[12] Max F Platzer and Franklin O Carta. Agard manual on aeroelasticity in axial-flow turbomachines. volume 2. structural dynamics and aeroelasticity. Technical report, ADVISORY GROUP FOR AEROSPACE RESEARCH AND DEVELOPMENT NEUILLY-SUR-SEINE (FRANCE), 1988.

[13] Paul Lowden, Joseph Liburdi, et al. Failure of turbomachinery components. In *Proceedings of the 14th turbomachinery symposium*. Texas A&M University. Turbomachinery Laboratories, 1985.

[14] Zdzislaw Mazur et al. L-0 blades failure investigation of a 110 mw geothermal turbine. In *ASME 2006 Power Conference*, pages 281–289. American Society of Mechanical Engineers Digital Collection, 2006.

[15] E Seinturier. Forced response computation for bladed disks industrial practices and advanced methods. *Lecture Series-Von Karman Institute For Fluid Dynamics*, 2:5, 2007.

[16] T Nicholas and JR Zuiker. On the use of the goodman diagram for high cycle fatigue design. *International Journal of Fracture*, 80(2-3):219–235, 1996.

[17] Daniel J Inman and Ramesh Chandra Singh. *Engineering vibration*, volume 3. Prentice Hall Englewood Cliffs, NJ, 1994.

[18] Earl Logan Jr. *Handbook of turbomachinery*. CRC Press, 2003.

[19] Chen-an Zhang, Zhengyin Ye, and Feng Liu. Numerical researches on aeroelastic problem of a rotor due to igv/fan interaction. In *47th AIAA Aerospace Sciences Meeting including The New Horizons Forum and Aerospace Exposition*, page 865, 2009.

[20] XQ Huang, L He, and DL Bell. Influence of upstream stator on rotor flutter stability in a low pressure steam turbine stage. *Proceedings of the Institution of Mechanical Engineers, Part A: Journal of Power and Energy*, 220(1):25–35, 2006.

[21] Maria Angelica Mayorca. *Numerical methods for turbomachinery aeromechanical predictions*. PhD thesis, Royal Institute of Technology, 2011.

[22] Yoji Hanamura, Hideo Tanaka, and Kazuo Yamaguchi. A simplified method to measure unsteady forces acting on the vibrating blades in cascade. *Bulletin of JSME*, 23(180):880–887, 1980.

[23] Matthew P Castanier and Christophe Pierre. Modeling and analysis of mistuned bladed disk vibration: current status and emerging directions. *Journal of Propulsion and Power*, 22(2):384–396, 2006.

[24] C Bré, ard, JS Green, and M Imregun. Low-engine-order excitation mechanisms in axial-flow turbomachinery. *Journal of Propulsion and Power*, 19(4):704–712, 2003.

[25] Stephan Netzhammer, Damian M Vogt, Stephan Kraetschmer, Johannes Leweux, and Andreas Koengeter. Aerodynamic excitation analysis of radial turbine blades due to unsteady flow from vaneless turbine housings. In *ASME Turbo Expo 2017: Turbomachinery Technical Conference and Exposition*. American Society of Mechanical Engineers Digital Collection, 2017.

[26] Stephan Netzhammer, Damian M Vogt, Stephan Kraetschmer, Johannes Leweux, and Jennifer Blackburne. Reducing blade force response in a radial turbine by means of jet injection. In *ASME Turbo Expo 2019: Turbomachinery Technical Conference and Exposition*. American Society of Mechanical Engineers Digital Collection.

[27] Stuart Connell, Mark Braaten, Laith Zori, Robin Steed, Brad Hutchinson, and Graham Cox. A comparison of advanced numerical techniques to model transient flow in turbomachinery blade rows. In *ASME 2011 Turbo Expo: Turbine Technical Conference and Exposition*, pages 1241–1250. American Society of Mechanical Engineers, 2011.

[28] Aravin Dass Naidu, Klemens Vogel, and Magnus Fischer. A comparative study of transient blade row and blade count scaling approaches for numerical forced response analysis in a transonic turbine. *ETC12*, 2017.

[29] JI Erdos, Em Alzner, and W McNally. Numerical solution of periodic transonic flow through a fan stage. *AIAA journal*, 15(11):1559–1568, 1977.

[30] L He. An euler solution for unsteady flows around oscillating blades. In *ASME 1989 International Gas Turbine and Aeroengine Congress and Exposition*, pages V001T01A098–V001T01A098. American Society of Mechanical Engineers, 1989.

[31] Michael B Giles. Calculation of unsteady wake/rotor interaction. *Journal of Propulsion and Power*, 4(4):356–362, 1988.

[32] Kenneth C Hall, Jeffrey P Thomas, and William S Clark. Computation of unsteady nonlinear flows in cascades using a harmonic balance technique. *AIAA journal*, 40(5):879–886, 2002.

[33] Arathi Gopinath and Antony Jameson. Time spectral method for periodic unsteady computations over two-and three-dimensional bodies. In *43rd AIAA aerospace sciences meeting and exhibit*, page 1220, 2005.

[34] Enrique Camara. Validation of time domain flutter predictiontool with experimental results, 2015.

[35] Christopher Fuhrer and Damian M Vogt. On the impact of simulation approaches on the predicted aerodynamic damping of a low pressure steam turbine rotor. In *ASME Turbo Expo 2017: Turbomachinery Technical Conference and Exposition*. American Society of Mechanical Engineers Digital Collection, 2017.

[36] Stuart Moffatt. *Forced response prediction for industrial gas turbine blades*. PhD thesis, Durham University, 2006.

[37] Stuart Moffatt and Li He. Blade forced response prediction for industrial gas turbines: Part 1—methodologies. In *ASME Turbo Expo 2003, collocated with the 2003 International Joint Power Generation Conference*, pages 407–414. American Society of

[38] Wei Ning, Stuart Moffatt, Yansheng Li, and Roger G Wells. Blade forced response prediction for industrial gas turbines: Part 2—verification and application. In *ASME Turbo Expo 2003, collocated with the 2003 International Joint Power Generation Conference*, pages 415–422. American Society of Mechanical Engineers Digital Collection, 2003. Mechanical Engineers Digital Collection, 2003.

[39] L He and DX Wang. Concurrent blade aerodynamic-aero-elastic design optimization using adjoint method. *Journal of Turbomachinery*, 133(1):011021, 2011.

[40] Norman E Dowling. *Mechanical behavior of materials: engineering methods for deformation, fracture, and fatigue*. Pearson, 2012.

[41] Yung-Li Lee, Jwo Pan, Richard Hathaway, and Mark Barkey. *Fatigue testing and analysis: theory and practice*, volume 13. Butterworth-Heinemann, 2005.

[42] BA Cowles. High cycle fatigue in aircraft gas turbines—an industry perspective. *International Journal of Fracture*, 80(2-3):147–163, 1996.

[43] Anthony J Strazisar, Jerry R Wood, Michael D Hathaway, and Kenneth L Suder. Laser anemometer measurements in a transonic axial-flow fan rotor. 1989.

[44] Ahad Mehdi. Effect of swirl distortion on gas turbine operability. 2014.

[45] P Colonna, NR Nannan, ALBERTO Guardone, and Eric W Lemmon. Multiparameter equations of state for selected siloxanes. *Fluid Phase Equilibria*, 244(2):193–211, 2006.

[46] Maher. https://www.maher.com/alloys. Accessed: 28/12/2019.

[47] Fábio Gustavo Lima Pereira, Jorge Magner Lourenço, Rubens Maribondo do Nascimento, and Nicolau Apoena Castro. Fracture behavior and fatigue performance of inconel 625. *Materials Research*, 21(4), 2018.